UNIVERSIDADE FEDERAL DO RIO GRANDE DO SUL

CHARLES AIRTON BOLZAN

Compositional, structural and thermoelectric characterization of $In_xGa_{1-x}Sb$ films deposited by magnetron sputtering and modified by ion irradiation

Caracterização da composição, estrutura e propriedades termoelétricas dos filmes de $In_xGa_{1-x}Sb$ depositados por *magnetron sputtering* e modificados por irradiação iônica

Brasil

2023

CHARLES AIRTON BOLZAN

Compositional, structural and thermoelectric characterization of $In_xGa_{1-x}Sb$ films deposited by magnetron sputtering and modified by ion irradiation

Caracterização da composição, estrutura e propriedades termoelétricas dos filmes de $In_xGa_{1-x}Sb$ depositados por *magnetron sputtering* e modificados por irradiação iônica

Thesis prepared under the supervision of professor Dr. Raquel Giulian, presented to the Physics Graduation Program of Instituto de Física at UFRGS, in partial fulfillment of the requirements for obtaining the title of Doctor in Sciences.

Brasil

2023

* This work was parcially supported by Conselho Nacional de Desenvolvimento Científico e Tecnológico (CNPq)

“In der Mitte von Schwierigkeiten liegen die Möglichkeiten.”

(Albert Einstein)

Abstract

$In_xGa_{1-x}Sb$ (x = 0.5, 0.6, 0.8 and 1) films were deposited by radio frequency magnetron sputtering onto SiO_2/Si substrates at 420 °C and the compositional, structural and thermoelectric characterizations of the films were performed for different In/Ga ratio concentrations before and after ion irradiation at different fluences. Rutherford backscattering spectrometry (RBS) and particle-induced x-ray emission (PIXE) were employed in the analysis of the relative atomic concentration of the films. The structure of the films was characterized by grazing incidence x-ray diffraction (GIXRD) and extended x-ray absorption fine structure (EXAFS) analyses, whereas scanning electron microscopy (SEM) provided information about the morphology of the films. The thermoelectric properties of the films were measured with the aid of an equipment specially developed for this purpose. GIXRD showed the formation of polycrystalline zincblende structure in as-deposited films with the lattice parameter changing linearly with composition x as predicted by Vegard`s law. EXAFS evidenced that the lattice mismatch in ternary compounds is accommodated favorably through bond bending over bond stretching. Regarding the thermoelectric properties, it was observed that $In_{0.8}Ga_{0.2}Sb$ films exhibited the highest ZT value (0.53 at 450 K) among the films investigated here. Upon ion irradiation with 16 MeV Au^{+7} ions with ion fluences ranging from 1×10^{13} cm^{-2} to 5×10^{14} cm^{-2}, $In_xGa_{1-x}Sb$ films presented a pronounced continuous-to-porous transformation and a bond length conservation with no loss of material or sputtering induced by the ion irradiation process. $In_xGa_{1-x}Sb$ compounds, however, exhibited a nonlinear stoichiometry-dependent porosity. Through GIXRD analysis, it was verified that it is easier to amorphize the ternary compound than its binary counterpart InSb. $In_xGa_{1-x}Sb$ nanofoams also showed to be remarkably stable under annealing in vacuum at 200 °C, with very small changes in atomic concentration induced by thermal annealing. Concerning the thermoelectric properties (ZT parameter), its value substantially decreased after ion irradiation. These results show that $In_xGa_{1-x}Sb$ films deposited by magnetron sputtering have potential application in gas sensor devices.

Keywords: $In_xGa_{1-x}Sb$ films; magnetron sputtering; extended x-ray absorption fine structure; grazing incidence x-ray diffraction; scanning electron microscopy; thermoelectric properties.

Resumo

Filmes de $In_xGa_{1-x}Sb$ (x = 0,5, 0,6, 0,8 e 1) foram depositados por magnetron sputtering em regime de radiofrequência sobre substratos de SiO_2/Si, a 420 °C, e as caracterizações composicional, estrutural e termoelétrica dos filmes foram realizadas para diferentes taxas de In/Ga concentrações antes e depois da irradiação com íons em diferentes fluências. Espectrometria de retroespalhamento Rutherford (RBS) e emissão de raios-x induzida por partículas (PIXE) foram empregadas na análise da concentração atômica relativa dos filmes. A estrutura dos filmes foi caracterizada por difração de raios-x de incidência rasante (GIXRD) e estrutura fina de absorção de raios-x estendida (EXAFS), enquanto a microscopia eletrônica de varredura (MEV) forneceu informações sobre a morfologia dos filmes. As propriedades termoelétricas dos filmes foram medidas com o auxílio de um equipamento especialmente desenvolvido para este fim. GIXRD mostrou a formação de estrutura de zincoblenda policristalina nos filmes depositados com o parâmetro de rede mudando linearmente com a composição x, conforme previsto pela lei de Vegard. EXAFS evidenciou que o descasamento de rede em compostos ternários é acomodado favoravelmente através da flexão da ligação sobre o alongamento da ligação. Com relação às propriedades termoelétricas, observou-se que os filmes de $In_{0.8}Ga_{0.2}Sb$ apresentaram o maior valor de ZT (0.53 a 450 K) entre os filmes aqui investigados. Após irradiação de íons com íons Au^{+7} de 16 MeV com fluências de íons variando de 1×10^{13} cm^{-2} a 5×10^{14} cm^{-2}, os filmes de $In_xGa_{1-x}Sb$ apresentaram uma pronunciada transformação da forma contínua à porosa e a conservação do comprimento de ligação sem perda de material ou pulverização induzida pelo processo de irradiação de íons. Os compostos $In_xGa_{1-x}Sb$, no entanto, exibem uma porosidade dependente da estequiometria não linear. Através da análise GIXRD, verificou-se que é mais fácil amorfizar o composto ternário do que o seu homólogo binário InSb. As nanoespumas $In_xGa_{1-x}Sb$ também mostraram ser notavelmente estáveis sob recozimento a vácuo em temperatura de 200 °C, com mudanças muito pequenas na concentração atômica induzidas pelo recozimento térmico. Com relação às propriedades termoelétricas (parâmetro ZT), seu valor diminuiu substancialmente após a irradiação iônica. Esses resultados mostram que os filmes de $In_xGa_{1-x}Sb$ depositados por magnetron sputtering têm potencial aplicação em dispositivos sensores de gás.

Palavras-chave: filmes de $In_xGa_{1-x}Sb$; magnetron sputtering; estrutura fina de absorção de raios X estendida; difração de raios X com ângulo rasante; microscopia eletrônica de varredura; propriedades termoelétricas.

Resumo para leigos

Esta tese fala sobre materiais que tem uma propriedade muito especial, a de se transformar em espumas nanométricas (incrivelmente pequenas, mas com área superficial gigantesca), e ao mesmo tempo podem ser utilizados para converter calor em energia elétrica. Quando misturamos In, Ga e Sb em diferentes proporções, o material que se forma tem propriedades que variam conforme a concentração de In e Ga, e isso pode ser muito útil pois permite manipular as propriedades do material simplesmente mudando a concentração. As distâncias entre os átomos mudam quanto mais In ou Ga colocamos, e isso induz outras mudanças na estrutura e no comportamento do material. Quando esses materiais são bombardeados com íons pesados velozes, o equivalente a atirar com uma arma contra uma parede só que em nível atômico, esses compostos se transformam em espumas sólidas nanométricas, cheios de buracos e com uma gigantesca área superficial como mostrado na figura A abaixo. As espumas são ótimas para fabricação de detectores de gás, por exemplo, porque são cheias de buracos e há muito espaço vazio e muita superfície para que moléculas de gás grudem ali (e assim possam ser detectadas). Esses materiais estudados também podem servir como termoelétricos porque eles conseguem converter calor em eletricidade de forma direta. Isso pode ser muito útil para aproveitar o calor que geralmente seria desperdiçado (em motores, por exemplo).

Figura_A – A figura (a) ilustra o material formado quando misturamos In, Ga e Sb em diferentes proporções, enquanto a figura (b) representa o mesmo material transformado em espumas sólidas nanométricas, após ser bombardeados com íons pesados velozes.

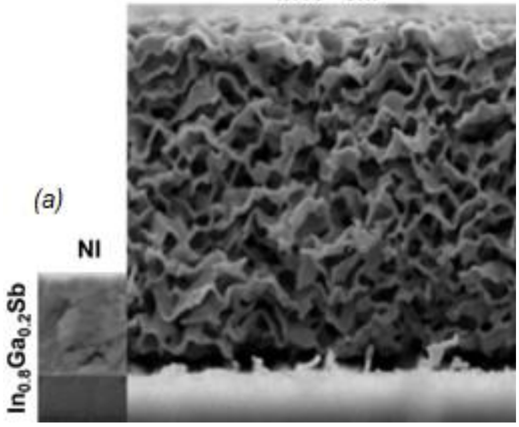

Summary

1 WHY TERNARY POROUS SEMICONDUCTORS ARE INTERESTING?

Porous semiconductors are not a new type of material, although it was not until the 1990s that studies on these materials were intensified. The first semiconductor to be rendered porous was Si discovered by Uhlir in 1956 (KOROTCENKOV e CHO3, 2010), however, a massive investigation in pore formation onto silicon was not performed until the independent work of Lehmann and Canham (CANHAM, 1990) (LEHMANN e GÖSELE, 1990). To obtain porous Si, both researchers used electrochemical dissolution (electrochemical reaction), which is the result of a current flowing through the solid/liquid interface, through a positive potential over the Si electrode (Figure 1.1).

Figure 1.1-Pore formation process in Si. The Si sample is immersed in an HF solution. A closed circuit is made between the Si sample and a Pt electrode. By applying a positive voltage to the sample, an electric current arises. A possible result of current flow is the formation of small holes in the substrate, which are called pores.

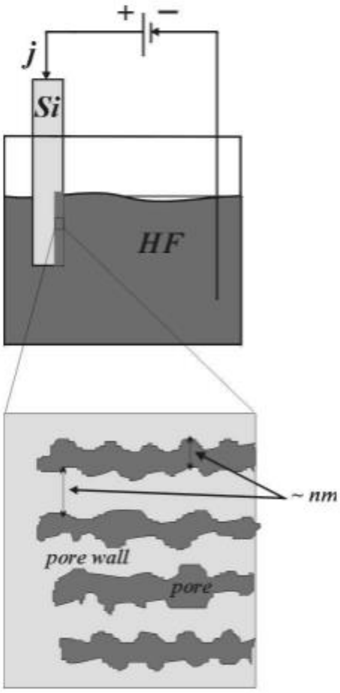

Reference: (TIGINYANU, LANGA, *et al.*, 2009)

A disadvantage of bulk Si, an indirect bandgap semiconductor, is that it does not present an efficient electron-hole recombination, that is, it is not luminescent. Porous Si, on the other hand, showed strong luminescence from red-orange to blue depending on its structure(KOROTCENKOV; CHO, 2010). The “explosion” in the investigation began after this unexpected discovery was published, allowing a possibility to integrate the properties of porous materials with the electronic and photonic characteristics of semiconductors.

Although porous Si was discovered in 1956 by Uhlir (KOROTCENKOV e CHO3, 2010), it was only in 2000`s that conditions were found for the production of pores in Ge (CHOI e BURIAK, 2000), (LANGA, CHRISTOPHERSEN, *et al.*, 2003), (FANG, FOLL e CARSTENSEN, 2006).

Comparing with porous Si, the first impression is that there would be no relevant arguments to investigate III-V semiconductors, due to the fact that approximately all representatives of this group show efficient luminescence in bulk form, without the need to become porous. The good emission properties of these compounds are mainly due to the fact that they are mostly semiconductors with direct bandgap and, therefore, electron-hole recombination is much more efficient compared to bulk Si. Despite all these counter-arguments, soon after the discovery of porous Si, investigations into III-V compounds began. Against all expectations, pores in III-V compounds began to be investigated in order to discover new optical properties beyond those already known in the bulk of these compounds.

III-V ternary semiconductors offer much more possibilities in this regard when compared to Si, due to the fact that the switch from the elementary semiconductor to the compound semiconductor involves a greater crystallographic modification and offers the possibility of changing its chemical composition. For example, combining GaSb, which has ~0.73 eV (at 300 k) bandgap and has been a potential material for infrared detectors and thermophotovoltaic solar cells(DUTTA; BHAT; KUMAR, 1997), with InSb, which has the smallest bandgap (~0.17 eV) (mid-infrared region), among the III-V binary compounds, with applications in infrared imaging systems and gas detection systems (VOLIN, GARCIA, *et al.*, 2002), (KIRBY e HANSON, 2002) a different semiconductor is obtained, in this case $In_xGa_{1-x}Sb$. In the ternary alloy $In_xGa_{1-x}Sb$, the optical bandgap can be tuned across the near infrared (NIR) and mid-infrared (mid-IR) regions of the electromagnetic spectrum from 1.7 µm to 7.3 µm (WOLENSKI et al., 2016). This broad tunability accommodates further applications in infrared sensing and detection, environmental monitoring, data communications, bioimaging, and thermovoltaics (REFAAT et al., 2004)(GREIN et al., 1995)(LI et al., 2020)(WANG et al., 1999). Other examples of ternaries are $In_xGa_{1-x}N$ and $Ga_xAl_{1-x}N$, which made it possible to manufacture more efficient light-emitting diodes, a project that received the Nobel Prize in Physics in 2014.

Consequently, the properties of each of these ternary compounds can be extended by making them porous. This large amount of materials, in their bulk and porous form, opens a new path for new physical properties not yet investigated extensively.

The presence of pores in a semiconductor generally breaks the symmetry of its crystal lattice and this will have consequences for all properties involving part of the crystal larger than the typical pore size (given by the average pore diameter and the average distance between pores). Phonons and photons can, therefore, be affected by the size of the pores, which, according to the classification used by some authors, would be mesopores (size 2-50 nm) and macropores (size above 50 nm) (OLL, CARSTENSEN e FREY, 2006), (H.FOLL, S.LANGA, *et al.*, 2003). For nanopores (<2 nm), the quantum confinement effect can be observed, as well as in the case of nanoparticles, however, for pores, being interpreted as the inverse image (anti-dots) of a set of regularly spaced nanoparticles (HEINRICH, CURTIS, *et al.*, 1992), (SHIMIZU-IWAYAMAI, NAKAOT, *et al.*, 1994), (ROY, JAYARAM e SOOD, 1994). As a result, porous materials can present an increase in bandgap with the reduction of the thickness of the walls that separate the pores, in a similar way to what was verified with the reduction of the size of nanoparticles (Figure 1.2). Examples which exploit the special properties created after the semiconductor becomes porous include their usefulness for photonic waveguides (LANGA et al., 2005), superhydrophobic and large antireflective properties(DATTA; SOM, 2016), chemical sensing based on the pore surface sensitivity to certain substances, and filters for proteins and other particles using the dispersion in pore size for high-size selectivity (FOELL; CARSTENSEN; FREY, 2006).

Therefore, III-V porous compound semiconductors exhibit new properties due to the exclusive combination of their crystalline structures and large internal surface areas, which allows higher adsorbate effects and lower thermal conductivity coefficient, making them very attractive for gas sensor(FOELL; CARSTENSEN; FREY, 2006) and thermoelectric materials(HE; WU, 2021).

Figure 1.2- Schematic representation of the relationship between nanoparticles and porous materials, where E_g is the bandgap.

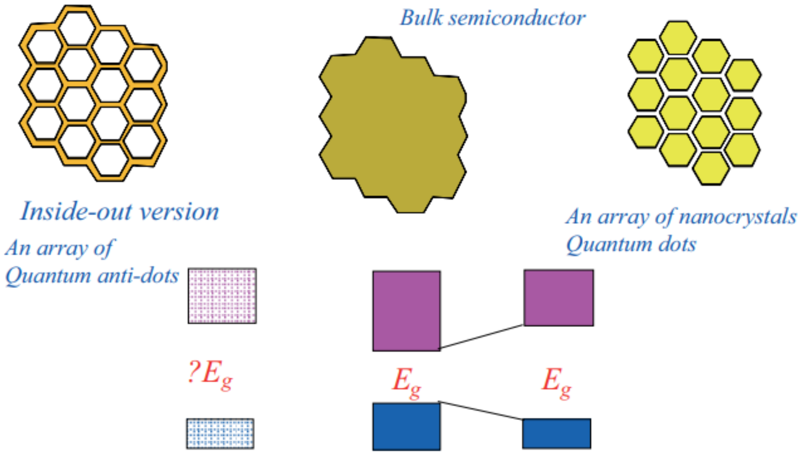

Reference: (KANATZIDIS, 2007).

Nevertheless, to make use of these interesting properties, the manufacturing quality of these materials is of fundamental importance so that their characteristics are effectively used (KOROTCENKOV e CHO3, 2010).

The process of pore formation in semiconductors can occur in several ways, the most used being the electrochemical reaction, which results in regularly spaced columnar structures, usually in the form of tubes (Figure 1.3), whose dimensions vary in size according to the conditions used in the manufacturing process.

Figure 1.3- Comparison between the pores formed by electrochemical reaction (a) and ion irradiation (b).

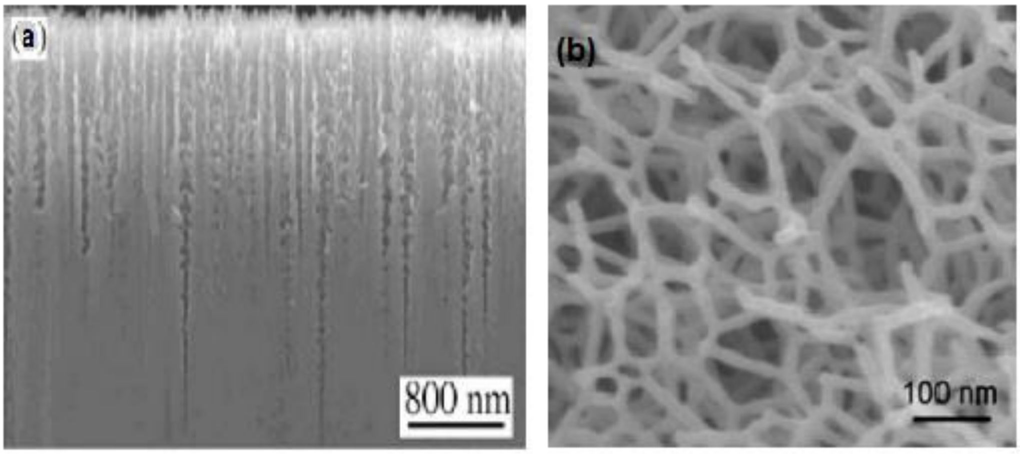

Reference: (KOROTCENKOV e CHO3, 2010) e (KLUTH, GERALD e RIDGWAY, 2005).

Another way of manufacturing porous semiconductors is ion irradiation, which, despite not being the most economically viable choice for industrial production (compared to the use of electrochemical reactions), represents an important tool in the study of these materials. The reproducibility and versatility of the technique (with regard to the choice of incident ions, their energies, fluences, sample temperature, among other parameters) allows the detailed study of the pore formation mechanisms, contributing to the identification and characterization of the properties of each material when implanted (irradiated) with ion beams.

Therefore, III-V porous ternary semiconductors allow new materials to be obtained, exhibiting an extensive diversity of optical, thermoelectric and morphological properties, which opens a great field for basic research and possible future applications.

In summary, the present thesis was organized in 9 chapters as follow:

Chapter 1 shows why porous ternary semiconductors are interesting to be investigated; chapter 2 describes the deposition technique to fabricate $In_xGa_{1-x}Sb$ films; chapter 3 shows the techniques used to characterize the samples; chapter 4 shows the structural and thermoelectric characterization of $In_xGa_{1-x}Sb$ prior and after ion irradiation: results and discussions; chapters 5 and 6 presents, respectively, the conclusions and references; chapters 7 and 8 show additional information via appendixes; finally, the chapter 9 presents the scientific publications made during my PhD program.

1.1 OBJECTIVE AND JUSTIFICATION

The present project aims to study the ternary compound $In_xGa_{1-x}Sb$ films deposited by magnetron sputtering technique, the subsequent modification of the films by irradiation with ion beams and the characterization of the structural and thermoelectric properties of these materials. Due to the fact that the size, shape and distribution of pores possibly have a strong influence on the behavior of a porous semiconductor, a systematic study of the formation, evolution and stability of pores can be used for a better understanding of the mechanisms responsible for such phenomenon, allowing, with this, greater control of the morphology and thermoelectric characteristics desired and, consequently, of the detector and selector properties of porous antimonides.

In this way, a study of the possible mechanisms of formation, evolution and stability of pores will allow a better manipulation of the parameters necessary for the manufacture of porous materials with the desired characteristics that, in turn, present technological potential, such as filters and nanometric membranes, sensors, steam and gas, among others. Therefore, this project is not only of scientific interest, but has a potential technological contribution with regard to the development of new materials.

In summary, the following main questions will be answered :

1- How does structurally $In_xGa_{1-x}Sb$ films behave before and after the effects of ion irradiation?

2- If the films become porous, do they have potential to be applied in gas sensors and as thermoelectric materials?

2 FILM MANUFACTURING AND MODIFICATION TECHNIQUE

In this chapter, it is shown the deposition and modification technique, respectively, used to fabricate and modify the $In_xGa_{1-x}Sb$ films.

2.1 MAGNETRON SPUTTERING

Magnetron sputtering technique has been used as a coating method since 1970s. It allows the deposition of high-purity films, with good control of film thickness and structure on a variety of substrates(SWANN, 1988). The characteristics of sputter-deposited films strongly depend on the substrate, pressure, growing rate, deposition temperature, and other parameters (KELLY; ARNELL, 2000a). Compared to Molecular Beam Epitaxy-grown films, the sputter-deposited ones can be produced more quickly and cheaply; although they seldom exhibit single crystal structure. However, relatively little work has been reported on the fabrication and characterization of antimonide films by magnetron sputtering (GIULIAN et al., 2017a), in particular regarding $In_xGa_{1-x}Sb$ thin films(GIULIAN et al., 2020b)

Sputtering is defined as the ejection of particles (atoms, ions) from a surface (called target) which is bombarded by energetic ions. The ions released from the target, in this process, through a vacuum environment, are deposited on a substrate to form the thin film.

The main principles of the magnetron sputtering process are shown in Figure 2.1.The idea is to enhance the ionization of the atoms to hit the target so that the number of sputtered material is increased compared to conventional sputtering. This is achieved by introducing magnetic fields close to the target surface with the help of horseshoe magnets arranged at the back side of the magnetron (Figure 2.1). The magnetron sputtering can be summarized as follow: To start the magnetron discharge, a DC voltage (1000-2000V) is applied to the target. It is also possible to connect alternating potential via RF (radio-frequency) supply onto the target. After, a gas, usually argon, is inserted in the vacuum chamber with the help of a gas regulating system. Owing to the high voltage, glow discharge (ionization of the argon gas) happens creating a plasma where the ions and electrons are separated. At this point, the free electrons will be affected by the Lorentz force. As a consequence, they are trapped in the magnetic field above the target, ionizing a large amount of argon atoms, restarting the process.

Once the ionization process has started, the positively charged argon ions are accelerated toward the target (negatively charged), thus beginning the sputtering process of the target material. The sputtered material will thereafter be transported and deposited onto the substrate(KELLY; ARNELL, 2000b)(MAURYA; SARDARINEJAD; ALAMEH, 2014)(NEE, 2015).

Figure 2.1- Simplified scheme of the magnetron sputtering process.

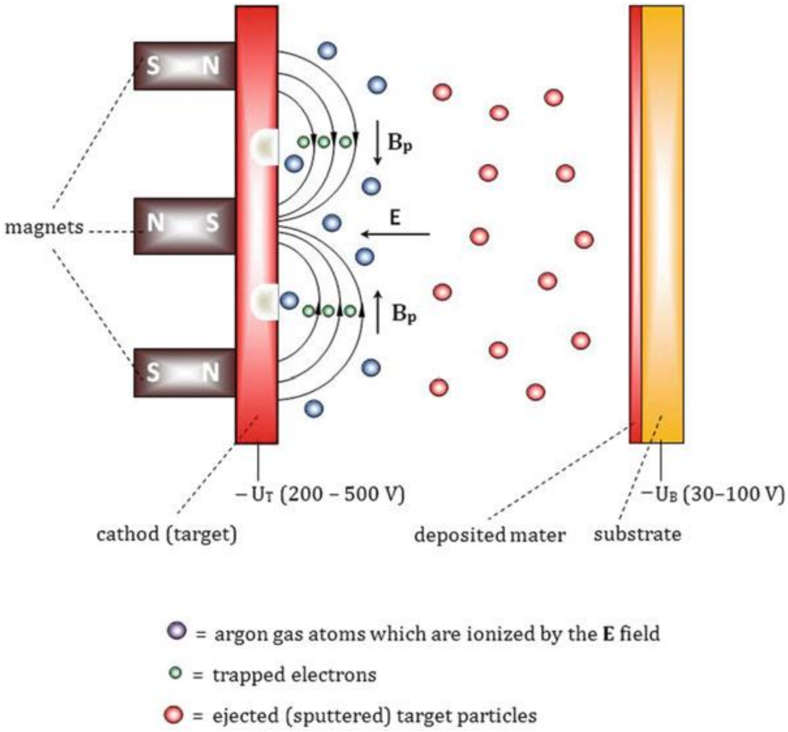

Reference: (NEE, 2015).

2.1.1 Experimental details

$In_xGa_{1-x}Sb$ (x = 0.5, 0.6, 0.8 and 1) films were deposited by RF magnetron sputtering onto SiO_2/Si substrates at 420 °C, using an AJA ATC Orion-8 Magnetron Sputtering System. The thickness of the SiO_2 insulating layer was 200 nm, while the thickness of each deposited $In_xGa_{1-x}Sb$ film was aimed at 300 nm. The base pressure was 2.5×10^{-5} Pa or lower and during deposition it was maintained at 0.27 Pa using a 20 sccm Ar constant flow and an adaptive pressure controller. The target diameter was 2 inches; the target-substrate distance was 5.8 inches (confocal configuration) with the substrate rotating at 40 rpm. The nominal thicknesses of the films were estimated from the deposition rates of InSb and GaSb films obtained through x-ray reflectivity analyses. $In_xGa_{1-x}Sb$ films were deposited by co-sputtering from InSb and GaSb targets. InSb target was set to 100, 50, 30, and 20 W (RF); GaSb target was set to 50 W (RF) in all depositions (except in the case of InSb with no Ga). The respective film deposition rates, in nm/s, were 0.18 (InSb), 0.16 ($In_{0.8}Ga_{0.2}Sb$), 0.086 ($In_{0.6}Ga_{0.4}Sb$), 0.057 ($In_{0.5}Ga_{0.5}Sb$) and 0.036 (GaSb). The purity of the targets was greater than 99.95%.

2.2 ION IRRADIATION

Ion irradiation is a technique generally used to modify the properties of a solid through the incidence of specific ions (Au^{+7}, in this work) towards a substrate that completely crosses the region of interest and only the effects of the deposited energy are considered (radiation damage). Therefore, this technique is different from ion implantation, as in this technique the ions are incorporated into the material.

Therefore, the radiation damage refers to the transfer of kinetic energy from the incident particle (Au^{+7}) to the solid and the result of the rearrangement of atoms in the solid. If the kinetic energy transferred to an atom is above a certain critical value (threshold) (E_d), the atom can be displaced from its initial position in the atomic structure, which can produce an additional displacement of atoms. An event in which only radiation damage occurs results in the creation of singly displaced atoms, such as point defects, or clusters of displaced atoms, whose accumulation of these events is known as material radiation damage (WESCH; WENDLER, 2016). Another effect that can be caused by ion radiation is localized electronic excitation, resulting in atomic motion creating so-called ion tracks, which will be described later.

2.2.1 Experimental details

After the fabrication of $In_xGa_{1-x}Sb$, described in details in section 2.1.1, for four different relative concentrations, $In_xGa_{1-x}Sb$ films were irradiated with 16 MeV Au^{+7} ions with ion fluences ranging from 1×10^{13} cm^{-2} to 5×10^{14} cm^{-2}. All measurements were performed in the Tandentron accelerator (model TN-4130-HC), with terminal voltage 3 MV, from the Ion Implantation Laboratory (LII) at UFRGS. The Tandetron accelerator provides several application lines, such as Rutherford backscattering spectrometry (RBS), Particle-Induced x-ray Emission (PIXE), among other techniques. Figure 2.2 is an illustration of this accelerator, which consists of two ion sources, which are used according to the chosen technique, one of the duoplasmatron type and the other of the sputtering type (SNICS); ion selection and injection system; stripper system, of gaseous nitrogen, in which the charge exchange of the ions and application lines occurs.

For the case of ion implantation, in this accelerator, the Au ion beam is obtained through an ion source, in which the Au target undergoes sputtering when irradiated by Cs atoms, thus, Au^{-1} ions are produced and extracted by a potential in the order of 30 kV. Afterwards, the ions are injected into the accelerator (whose terminal operates at approximately 2.12 MV), which, due to the impurities inside the chamber, need to be selected according to the desired ion. The selection takes place by means of an electromagnet that deflects the beam and together with the mass separator, the charge/mass ratio is obtained. Next, the ions are accelerated towards the terminal, where they become Au^{+7} ions through the loss of electrons in the N_2 gas stripper region, being repelled by the positive terminal (accelerated) and reaching a final energy of 16 MeV, given by $E=(1+q)V_t$, where q is the state of charge (q=+7 in this case) and V_t is the terminal voltage. Finally, the beam is directed to the implant chamber, where it scans the entire sample (x and y axes), in an implanted area of 2x2 cm^2 with approximately uniform fluence.

Figure 2.2-Schematic of the main parts of the tandetron accelerator.

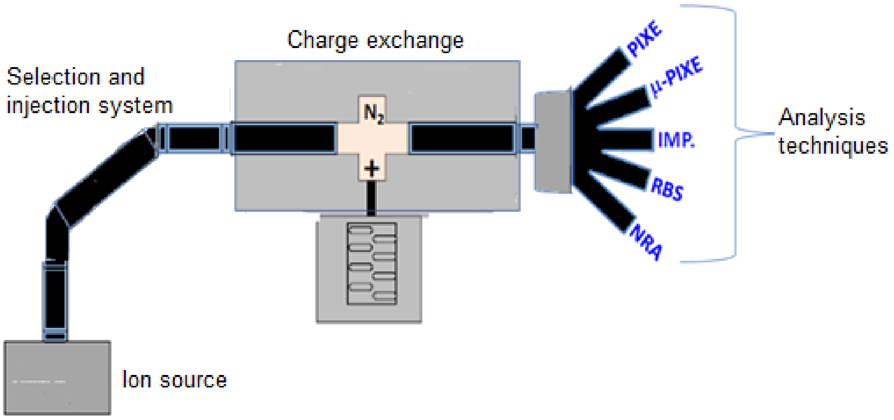

3 ANALYSIS TECHNIQUES

In this chapter, it is shown that the techniques employed in this work for the compositional, structural and thermoelectric characterization of $In_xGa_{1-x}Sb$ films for different concentrations when irradiated by different fluences. Rutherford backscattering spectrometry (RBS) and Particle-Induced x-ray Emission (PIXE) were used to identify the relative composition of the samples. In order to characterize the films structurally, it was used grazing incidence x-ray diffraction (GIXRD), extended x-ray absorption fine structure (EXAFS) and scanning electron microscopy (SEM). These techniques are available at the Nanometric Conformation Laboratory (for GIXRD) and Microscopy and Microanalysis Center (for SEM) at UFRGS. The thermoelectric characteristics of the materials were measured with the aid of an equipment specially developed for this purpose, which will be described briefly on section 3.7.1.

3.1 RUTHERFORD BACKSCATTERING SPECTROMETRY

Rutherford backscattering spectrometry (RBS) is a widely used technique for quantitative analysis of composition, depth and thickness profiles in various branches of materials science (FRIEDBACHER e BUBERT, 2011), (CHU, MAYER e NICOLET, 1978), (WANG e NASTASI, 2009), (VERMA, 2007), (W.A.GRANT, 1989).

In RBS, a monoenergetic beam of ions, H^+ or He^+, with energy in the range of 0.5 to 2.5 MeV, is directed to a target under study. Ions move through the target, losing energy along the way, and those that are backscattered (see Figure 3.1) by elastically colliding with atoms within the sample, are collected by a detector that counts the number of backscattered particles and their energies. The interaction between the projectile and the target's atoms can be described as an elastic collision between two isolated particles (FRIEDBACHER e BUBERT, 2011), (W.A.GRANT, 1989).

The energy of the projectile after the collision (E_1) can be related to its energy before the collision (E_0) through a *k* factor (kinematic factor). As a consequence of the principles of energy conservation and linear momentum, we obtain that the *k* factor is given by (CHU, MAYER e NICOLET, 1978):

$$k = \frac{E_1}{E_0} = \frac{\left(Mcos\theta + \sqrt{M_1^2 - M^2 \sin^2\theta}\right)^2}{(M+M_1)^2}\ , \qquad (1)$$

where *M* is the projectile mass, M_1 the target mass and θ the backscatter angle.

Figure 3.1- Schematic of the backscattering process of a projectile of mass *M* with energy E_0, due to the elastic collision with a target particle of mass M_1, initially at rest. In addition, the corresponding RBS spectrum resulting from the analysis of the highlighted InSb/SiO2/Si system is presented.

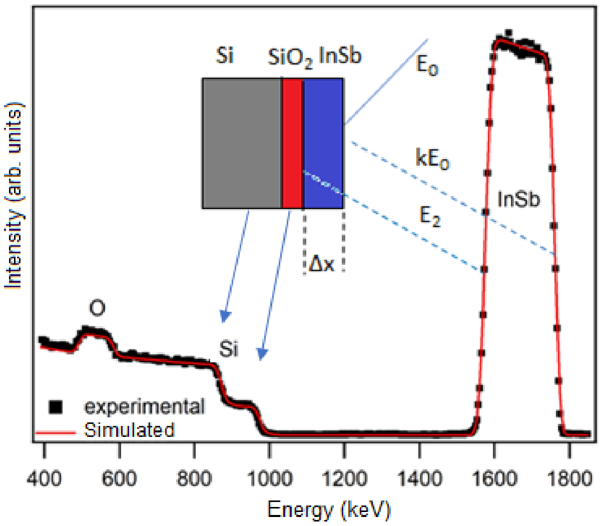

For a particular combination of *M*, M_1 and θ, equation (1) relates the energy of the incident particle with the corresponding energy with which it leaves the material:

$$E_1 = k_i E_0, \tag{2}$$

where k_i represents the kinematic factor for an element i, presented above, which varies according to the target under study. The energy after backscattering is determined solely from the incident particle masses, target mass and scattering angle θ. These expressions allow us to determine the mass of the scattering nucleus, once the energy of the particles backscattered in a given direction is known, and consequently to identify it (W.A.GRANT, 1989), (CHU, MAYER e NICOLET, 1978).

The energy of the scattered ions, given by equation (2), is valid for the scattering by atoms of the target surface. However, in RBS, the ion beam penetrates the target and its scattering depends on the scattering cross section. When the projectile passes through the scattering medium, it suffers an average loss of energy per unit of length $\frac{dE}{dx}$ known as stopping power or stopping cross section, attaining an energy E_2, which therefore depends on the depth Δx (Figure 3.1) Finally, due to the statistical fluctuation in the energy loss of the projectile penetrating the target, particles with a given energy will not have the same energy when traveling equal distances, a phenomenon called energy straggling (FRIEDBACHER e BUBERT, 2011), (W.A.GRANT, 1989).

Therefore, we present the four basic concepts that make up RBS. The kinematic factor k, which allows us to perform a mass analysis; the scattering cross section that provides the quantitative character of RBS; the stopping power, which provides a depth analysis; and the energy dispersion, which shows the limits of resolution of mass and depth.

3.1.1 Experimental details

RBS was performed in a Tandetron accelerator at the Ion Implantation Laboratory at UFRGS, using 1.5 MeV He^+ ions with currents not exceeding 20 nA. The backscattered ions were detected by a Si surface barrier device located at 15° with respect to the beam direction. Experimental data were simulated using the SIMNRA software (MAYER, 1999).

3.2 PIXE

Particle-Induced x-ray Emission (PIXE) is a technique whose physical principle is an x-ray emission by atoms when a beam of ions (in the case of this work, protons) interacts with them with supplied energy (in the range of 1-5 MeV). When the beam hits the sample, it can cause the ionization of its constituent atoms, promoting the ejection of an electron, which is replaced by another electron from an outermost shell of the same atom. In electron transition, the release of an x-ray, with energy related to the energy difference between the layers, occurs. Therefore, the x-rays emitted are characteristic of each atom and each electronic transition (JOHANSSON e JOHANSSON, 1976), (VERMA, 2007).

In this work, only thin samples were used. In short, thin samples are those in which the proton energy loss and x-ray attenuation are negligible (WANG e NASTASI, 2009). An example of a PIXE spectrum is shown in Figure 3.2.

Figure 3.2- Particle induced x-ray emission spectrum from $In_{0.2}Ga_{0.8}Sb$ sample after irradiation with $1x10^{14}$ cm^{-2} Au^{+7} ions, 16 MeV. C, N and O peaks steam from K_α radiation.

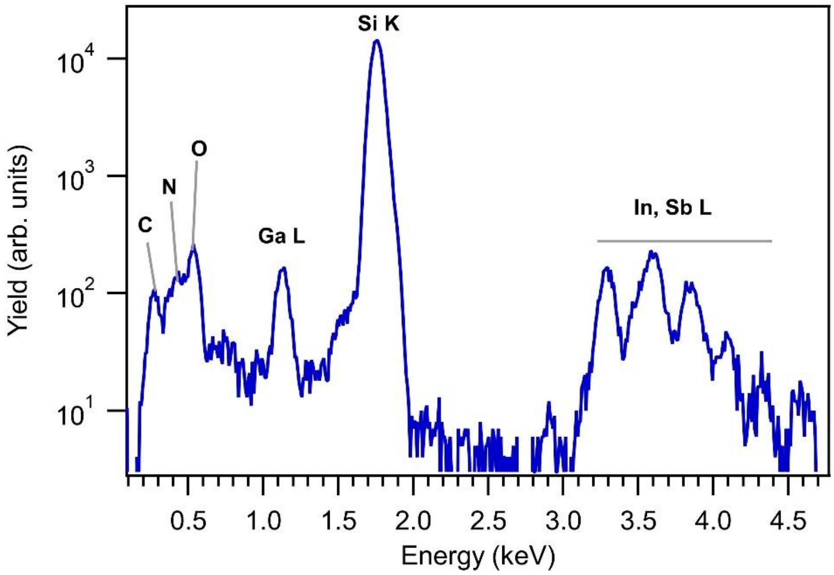

Converting the number of x-rays, resulting from an element in a sample, with its respective concentration can be complex, because it requires the knowledge of several aspects relative to the sample and the ion beam, such as (WANG e NASTASI, 2009): (a) energy of the ray lines X, to identify each peak in the spectrum; (b) information about the stopping power and x-ray attenuation factors, as well as the cross section of the photoelectric effect, which are essential in obtaining the x-ray counts and secondary contribution, respectively.

From numerical procedures it is possible to model the PIXE spectrum and convert the peak area into elementary concentrations. The following equation was used for this purpose (WANG e NASTASI, 2009):

$$Y(Z) = \frac{N_{av}}{A_z}\omega_{KZ}b_{KZ}t_{KZ}\varepsilon_z^t\left(\frac{\Omega}{4\pi}\right)N_pC_z\int_{E_0}^{Ef}\frac{\sigma_Z(E)T_Z(E)}{S_M(E)}dE, \quad (3)$$

where N_{av} is Avogadro's number; ω_{KZ}, the fluorescence of the elements; b_{KZ}, the fraction of x-ray intensity; t_{KZ}, the transmission between any absorbers interposed between the sample and the detector; ε_z^t, the intrinsic efficiency of the detector; N_p, the number of protons that reached the sample; C_z, the concentration of an element; E_0 and E_f are the input and output energies of the protons; $\sigma_z(E)$ is the K-layer ionization cross section for protons with energy E corresponding to a depth x inside the sample;

$T_z(E)$, the x-ray transmission factor in the matrix; $S_M(E)$, the stopping power of the matrix; $\frac{\Omega}{4\pi}$, the solid angle fraction of the detector. The equation (3) is valid for electron transitions to the K shell, however, similar equations can be obtained for L and M transitions.

The equation (3) can be summarized by defining $Y(Z)$ as the number of x-rays per unit of solid angle, proton charge and concentration, where the C_z concentration of an element is obtained by the following equation (WANG e NASTASI, 2009) :

$$Y(Z) = H\varepsilon^{i} z t_z C_z Y_I(Z), \tag{4}$$

where the constant *H* gathers the experimental and geometric factors specific to each PIXE system. However, H is not always constant and can vary with energy, being determined with thin film standards of previously known concentrations (WANG e NASTASI, 2009).

3.2.1 Experimental details

The PIXE technique was employed with 2 MeV protons and average current of 0.2 nA. A silicon drift detector placed at 135° with respect to the beam direction was used for the detection of the x-rays induced by the proton beam with an energy resolution of 150 eV at 5.9 keV. The PIXE calibration was performed via the H method (YONGQIANG; MICHAEL, 2009) and the corresponding spectrum was analyzed with the GUPIXWIN software package (MAXWELL; CAMPBELL; TEESDALE, 1989).

3.3 GRAZING INCIDENCE X-RAY DIFFRACTION

Grazing incidence x-ray diffraction refers to a measurement of x-ray diffraction, but with a small incidence angle (α <1 °, generally). In this configuration, the samples show diffraction peaks resulting from diffraction planes not parallel to the sample surface as shown in Figure 3.3. This measurement geometry is useful since it increases the irradiated volume, especially in the case of thin films. Moreover, there is the added benefit of avoiding the diffraction peaks from the substrate, in our case of Si

(BRACCO; HOLST, 2013; CHANG, 2001; HINRICHS, 2014; SEGMULLER, 1987; WIDJONARKO, 2016).

This additional advantage can be explained by pure geometry. Considering a sample that is thicker than the x-ray absorption length (~ $10\mu m$) and the incidence radius is at a large angle (Figure 3.4-a). In this case, a large part of the incident x-rays is absorbed by the substrate instead of the film, resulting in a loss of signal. Reducing the incidence angle, allows x-rays to be absorbed more by the film than by the substrate, increasing the signal (Figure 3.4-b) (BRACCO; HOLST, 2013)(BIRKHOLZ, 2006).

From Figure 3.4-a, it can be seen that the geometry is the same as that used in conventional XRD, that is, the incidence angle and diffraction are the same. For this to be true, for Bragg's condition in GIXRD, the reference for the diffraction angle is no longer the sample surface (as it is for conventional XRD), but the set of planes that give rise to the peak (HINRICHS, 2014).

Figure 3.3- Incidence angle (α) and detection of diffraction peaks when the detector is in positions 1,2 and 3. The detector is moved at β = $2\theta - \alpha$.

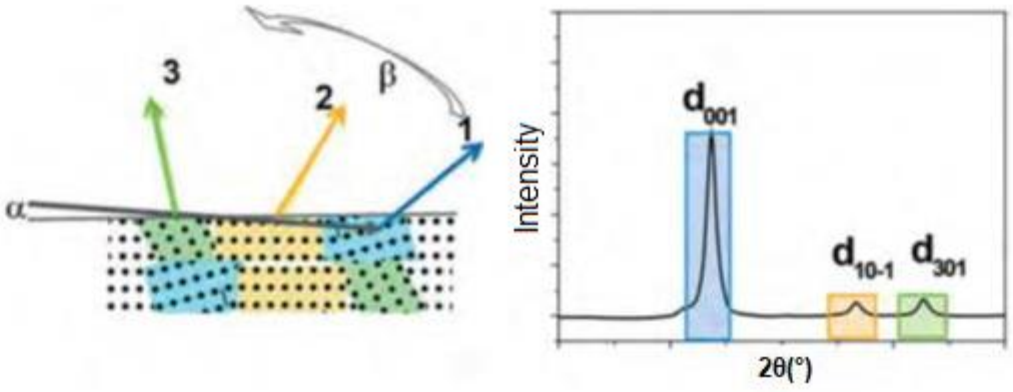

Reference: adapted from (HINRICHS, 2014).

Figure 3.4-(a) Illustration of XRD done at a high incident angle on a thin film. Note that the beam spot is small and that the XRD may penetrate through the thin sample. (b) The same measurement, however, done at low incident angle, causing the beam spot to widen, hence reducing x-ray flux on the sample and reducing x-ray damage.

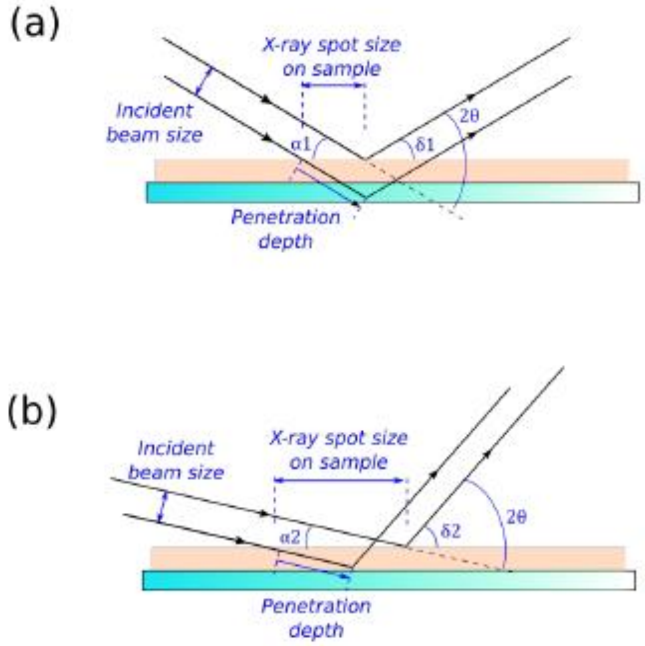

Reference: (WIDJONARKO, 2016).

3.3.1 Experimental details

For both films, GIXRD analyses were performed in a Bruker D8 Advance diffractometer using Seemann–Bohlin geometry. The incidence angle of x-rays was 0.5° with respect to the sample surface using Cu Kα radiation (1.5418 Å).

3.4 EXTENDED X-RAY ABSORPTION FINE STRUCTURE

$B_{(x)}A_{(1-x)}C$ ternary alloys play an important role in optoelectronic devices and heterojunction (CHEN; SUN; LV, 2017; VURGAFTMAN; MEYER; RAMMOHAN, 1997) due to the capability to attaining physical properties F(x) that are a simple interpolation of the properties of the two end-point binary compounds (F_{AC} and F_{BC}). This relation is described by a quadratic form:

$$F(B_{(x)}A_{(1-x)}C) = (1-x)F_{AC} + xF_{BC} + bx(1-x), \quad (5)$$

where b is the bowing parameter, which shows a strong dependence on the atomic structure of the alloy (SCHNOHR, 2012; ZUNGER; JAFFE, 1983). This equation applies for many properties such as bandgap(ADACHI, 2009) and elastic constant (BERGGREN; HANKE; TRAMPERT, 2016). As a consequence, structural information is crucial to understand and correctly tailor the optical, thermodynamic, mechanical, and electronic properties of ternary alloys. Extended x-ray absorption fine structure (EXAFS) is a powerful technique to access atomic structure in elemental (GLOVER; FORAN; RIDGWAY, 2003)(RIDGWAY et al., 2000) and compound materials (SCHNOHR et al., 2012). Over the past years it has been applied in a large number of systems from, chemistry, biology, geology, material science and environmental science (KONINGSBERGER; PRINS, 1988)(REHR; ALBERS, 2000). Since EXAFS is a short-range probe, this technique is sensitive, besides other parameters, to the interatomic distances, which allow this technique to correlate atomic-scale structure with other properties such as refractive index and bulk modulus as reported by Reddy et al. (REDDY et al., 2003) and Cohen(COHEN, 1985). As a consequence, an understanding of the atomic-scale structure is required to explain the optical and mechanical properties of binary compounds and ternary alloys.

3.4.1 Basic principle

Extended x-ray absorption fine structure (EXAFS) refers to the oscillatory structure in the x-ray absorption coefficient just above an x-ray absorption edge. In other words, EXAFS is the modulation of an atom’s x-ray absorption probability at energies near and above the binding energy of a core-level electron of the atom This behavior turns out to be a “fingerprint” of a given material; it also depends on the detailed atomic structure and electronic and vibrational properties of the material (REHR; ALBERS, 2000)(SCHNOHR; MARK, 2015).

3.4.2 x-ray absorption

When x-ray beam of intensity I_0 is incident on a sample (with thickness t) (Figure 3.5(a)), the process of absorption is governed according to Beer's law as follow:

$$I_t = I_0 e^{-\mu(E)t} \ . \tag{6}$$

where $\mu\,(E)$ is the energy-dependent x-ray absorption coefficient. At most x-ray energies, the absorption coefficient μ is a smooth function of energy (Figure 3.5(b)), with a value that depends on the sample density ρ, the atomic number *Z*, atomic mass *A*, and the x-ray energy *E* roughly as $\mu\,(E)\sim\frac{\rho Z^4}{m(E)^3}$ (REHR; ALBERS, 2000)(NEWVILLE, 2014).

Figure 3.5-**.** (a)Schematic of incident and transmitted x-ray beam and (b) absorption coefficient $\mu\,(E)$ versus photon energy E around an absorption edge.

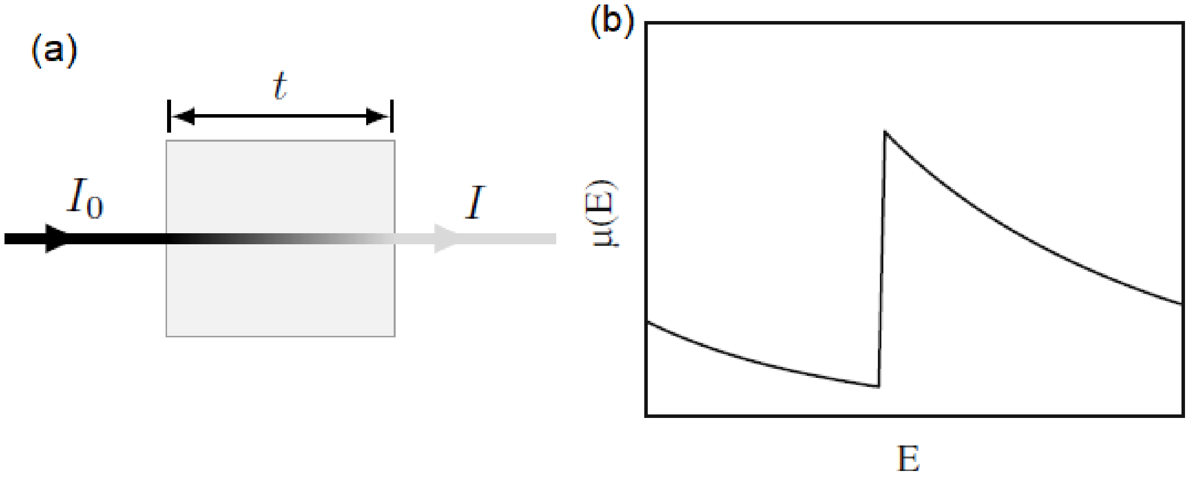

References: (a) (NEWVILLE, 2014), (b)(SCHNOHR; MARK, 2015).

Using the x-ray absorption position as a reference, two different regions are typically distinguished as indicated in Figure 3.6. The x-ray absorption near edge structure (XANES) constitutes the edge itself and the region very close to it while the extended x-ray absorption fine structure (EXAFS) extends from approximately 30 eV above the edge up to 1000 eV or more above the edge(KONINGSBERGER; PRINS, 1988)(NEWVILLE, 2014)(REHR; ALBERS, 2000)(SCHNOHR; MARK, 2015).

Figure 3.6 - x-ray absorption coefficient versus photon energy measured at the In K-edge (27.94 keV) of crystalline InSb. The black and blue arrows indicate the region of the x-ray absorption near edge structure (XANES) and the extended x-ray absorption fine structure (EXAFS), respectively.

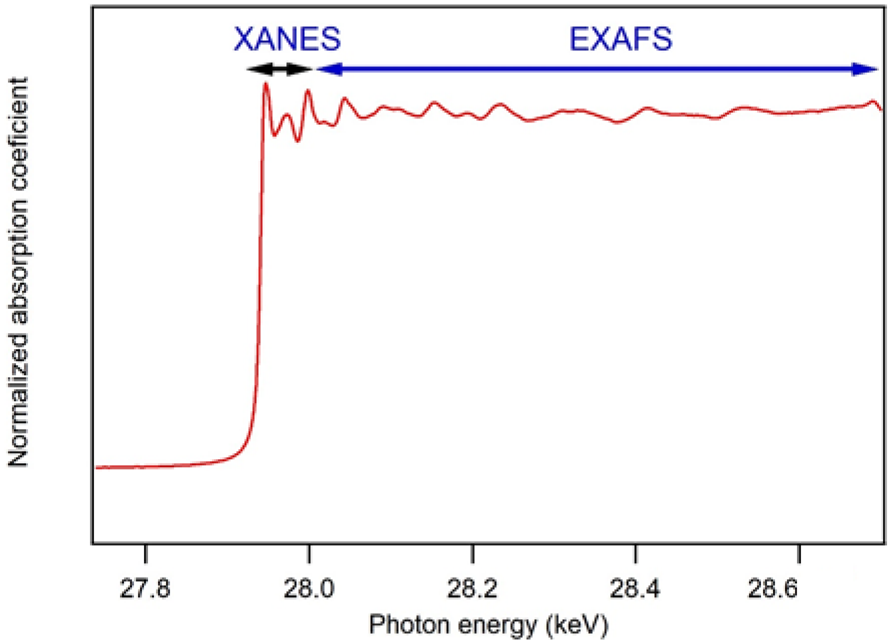

3.4.3 EXAFS theory

The extended fine structure fundamentally derives from the wave nature of photoelectrons. When an electron, with binding energy E_0, is ejected from an isolated atom due to an x-ray of energy E, the photoelectron's final state can be represented by an expanding spherical wave such as $\lambda \; \alpha \; \frac{1}{\sqrt{E-E_0}}$ (Figure 3.7(left)). It is worth mentioning that there is a sharp jump in the probability of absorption as the x-ray energy is increased above a core level binding energy. In fact, these binding levels are often referred to as absorption edges due to this strong increase in absorption probability as shown in Figure 3.7 (right). However, the absorption of the x-ray by the particular core electron level requires there to be an available quantum state for the ejected photoelectron to go to or if the photoelectron receives sufficient kinetic energy, it is going to be ejected to the continuum state.

Figure 3.7- X-ray absorption through the photoelectric process of an isolated atom. As the energy of the x-rays is increased to just above the energy of a tightly bound core electron level, *E*0, the probability of absorption has a sharp rise—an edge jump. In the process of absorption , a photoelectron is created with $\lambda \sim \frac{1}{\sqrt{E-E_0}}$.

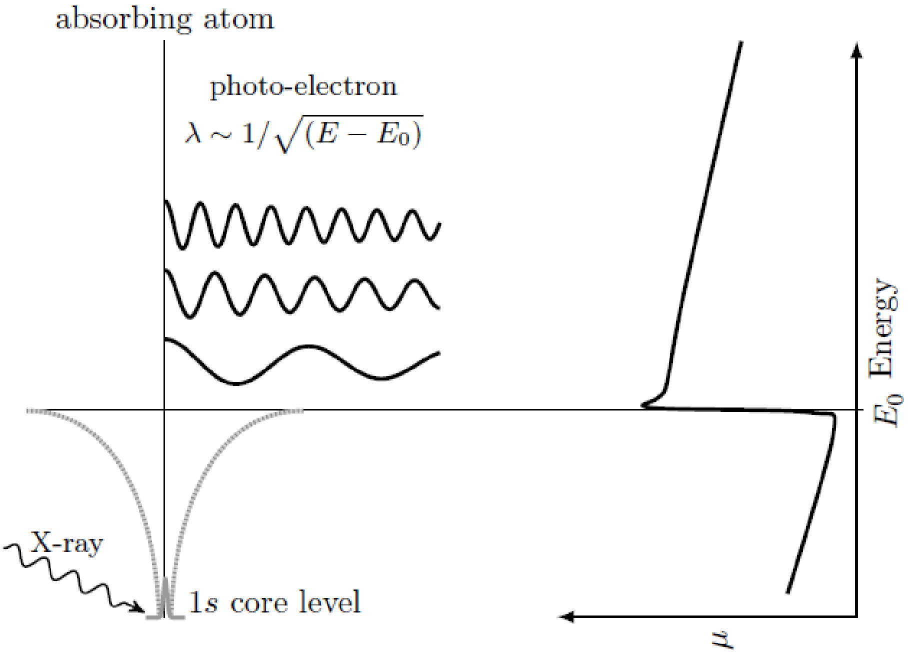

Reference: (NEWVILLE, 2014).

The picture described above is for an isolated atom. When the absorbing atom is not isolated, the photoelectron can scatter from the nearby atoms. The final electron state is then a superposition of the outgoing and scattered waves as shown in Figure 3.8. Since the absorption coefficient depends on whether there is an available, unfilled electronic state at the location of the atom and at the appropriate energy (see section 3.4.2) (and momentum), the presence of the photoelectron scattered back from the neighboring atom will alter the absorption coefficient. This is the simple theoretical description of EXAFS(SCHNOHR; MARK, 2015)(NEWVILLE, 2014)(REHR; ALBERS, 2000).

Figure 3.8- The origin of EXAFS is due to the fact that the photoelectron can scatter from a neighboring atom. The scattered photoelectron modulates the amplitude of the photoelectron wave-function at the absorbing atom. Thus this modulates the absorption coefficient μ(E), causing the EXAFS.

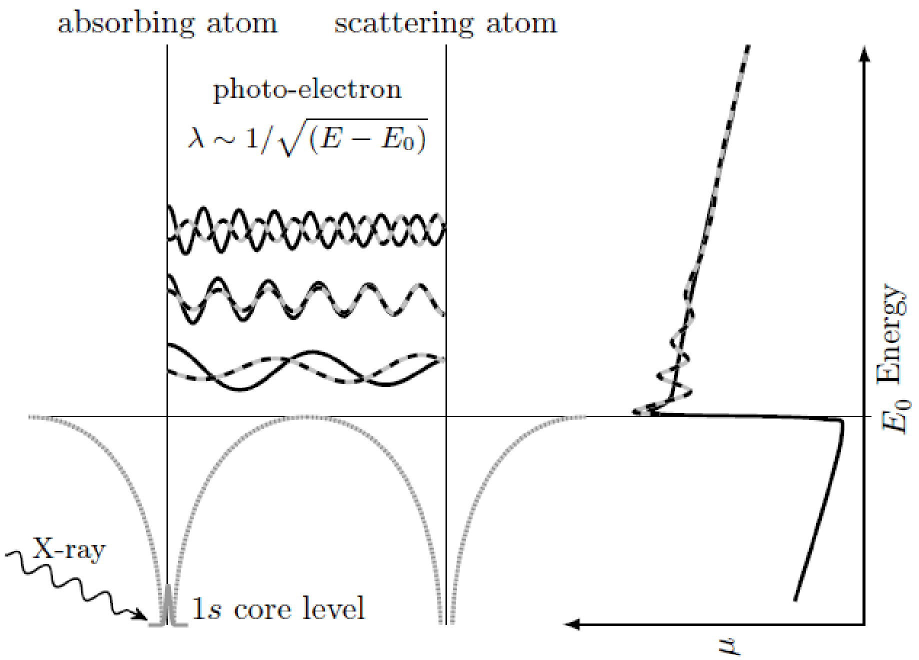

Reference: (NEWVILLE, 2014).

3.4.4 EXAFS equation

For EXAFS analysis, we are interested in the oscillations above the absorption edge, and define the EXAFS oscillations $\chi(E)$ as a change to $\mu(E)$, as follow

$$\mu(E) = \mu_0(E)(1 + \chi(E)) \rightarrow \chi(E) = (\mu(E) - \mu_0(E))/\Delta\mu \, , \qquad (7)$$

where $\mu_0(E)$ is the absorption of an isolated atom and $\Delta\mu$ is the measured jump in the absorption $\mu(E)$ at the threshold energy. Usually, $\chi(E)$ is represented as a function of the photoelectron wave number $k = \sqrt{\left(\frac{2m_e(E-E_0)}{\hbar}\right)}$. where m_e stands for the electron mass and $\hbar$ denotes Planck's constant divided by 2π. Using the multiple scattering path expansion(REHR; ALBERS, 2000) , EXAFS oscillations can be expressed as follow:

$$\chi(k) = \sum S_0^2 \, N_R \left(\frac{|f(k)|}{kR^2}\right) \sin(2kR + 2\,\delta_c + \vartheta) \, e^{-\frac{2R}{\lambda(k)}} e^{-2\sigma^2 k^2} \, . \qquad (8)$$

Here the structural parameters are the interatomic distances *R*, the coordination number (or number of equivalent scatterers) N_R , and the temperature-dependent root-mean-square fluctuation in bond length σ, which should also include effects due to structural disorder. In addition, $f(k) = |f(k)|e^{i\vartheta(k)}$ is the complex scattering amplitude, δ_c is central-atom partial-wave phase shift of the final state, and $\lambda(k)$ is the energy-dependent XAFS mean free path. The overall amplitude factor S_0^2 (which takes into account the relaxation of the system in response to the creation of the core-hole) did not appear in the original formula, however it was added here for completeness, since the resulting equation can be obtained from a more detailed many-body theory (NEWVILLE, 2014)(SCHNOHR; MARK, 2015)(REHR; ALBERS, 2000).

3.4.5 XANES

XANES region is characterized by transitions of the photoelectron to unoccupied bound states. Based on this, XANES is sensitive to the chemical bonding, exhibiting for example characteristic features for different oxidation states of the absorbing atom. Theoretical calculations of the fine structure in this region are complex, although significant progress in recently years has been made, such simulations are still limited. Therefore, analysis normally compares the measured spectra to those of known standards and quantifies the ratios by which these standards are present in the sample using linear combination fitting (LCF). Further details about LCF can be found elsewhere(KONINGSBERGER; PRINS, 1988)(REHR; ALBERS, 2000).

3.4.6 Experimental aspects: Synchrotron radiation and Detection modes

EXAFS requires a high x-ray beam intensity of finely tunable energy, therefore, most modern EXAFS experiments are performed at Synchrotron Radiation Sources. Synchrotron radiation is a generic term to describe radiation from charged particles traveling at relativistic speeds in an applied magnetic field, which forces them to travel on curved paths. When charged particles are accelerated, they emit radiation, and when relativistic electrons are forced to travel a curved path, they emit photons in a continuous spectrum, high intensity, strong polarization and a pulsed nature. Initially, electrons are injected and accelerated in a linear accelerator up to the energy of hundreds of MeV to several GeV. After, the electrons pass to the synchrotron ring. In this region, due to the circular trajectory of electrons, they lose energy during their emission of electromagnetic radiation (which is emitted tangentially in a narrow angled cone). As a way to compensate for this energy lost by the electrons and synchronize them (origin of the name synchrotron), radio frequency generators are used around the ring. The current gradually decreases because of electron collisions with any molecules contained within the ring, despite the conditions of ultra-high vacuum (10^{-9} - 10^{-10} Torr), therefore requiring a new injection of electrons in the accelerator every ~ 15h (depending on the synchrotron ring)(JAESCHKE; HASTINGS, 2016)(BUNKER, 2010)(SCHNOHR; MARK, 2015). Recently, nonetheless, top-up operation is a new way of injecting beam into the accelerators. The new mode sees the accelerators refilled with electrons every 20 minutes rather than every ~ 15h as previously. This results in a much higher integrated current over a 24-hour period, providing users with better beam stability, low vertical emittance in all filling modes (with correspondingly higher brilliance and resolution) and a nearly constant beam current.

Regarding the detection modes, there are different ways to measure the absorption coefficient. Here it was included only the description of transmission and fluorescence modes, since those are effectively the most simplest detection modes. The schematic configuration of both experimental setups is shown in Figure 3.9. In the transmission mode, both the incoming (I_0) and the transmitted beam (I) are measured by ion chambers, thus the absorption coefficient can be obtained via Beer's law (section 3.4.2). To use this mode, the samples need to be highly homogeneous, of constant thin thickness and free of pinholes. Concerning the fluorescence mode, incoming beam I_0 is again measured by an ion chamber while the intensity of the characteristic fluorescence x-rays is usually detected by an energy dispersive Si or Ge solid state detector. The big advantage of this method is the ability to measure highly dilute and non-homogeneous samples(SCHNOHR; MARK, 2015)(NEWVILLE, 2014).

Figure 3.9- Sketch of the detection modes. Through Synchrotron Radiation Sources, a collimated beam of x-rays with a broad energy spectrum is produced. The corresponding energy of these x-rays are selected by a slit and monochromator. The incident x-ray intensity, I_0, is sampled. EXAFS can be measured by the intensity transmitted through the sample or by measuring the intensity x-ray fluorescence resulting from the x-ray absorption.

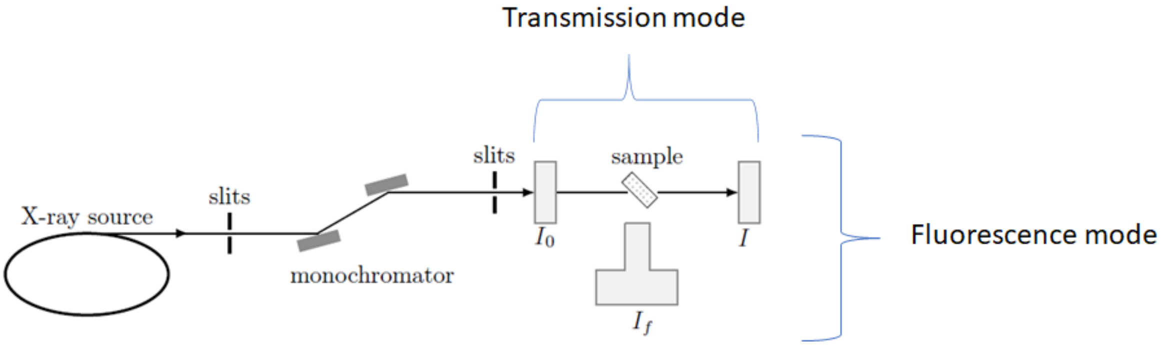

Reference: Adapted from (NEWVILLE, 2014).

3.4.7 Experimental details

For $In_xGa_{1-x}Sb$ films, EXAFS measurements of In and Ga K-edges were performed in fluorescence mode at the XAS Beamline (Melbourne, Australia) at 300 K. EXAFS data were processed and analyzed using software code IFEFFIT(NEWVILLE, 2001) together with FEFF6(REHR; ALBERS, 1990), for non-linear least-squares fitting of the first nearest-neighbor (NN) shell. EXAFS spectra were Fourier transformed over a photoelectron wave-number (k) range of k= 2-12 A^{-1} for both In and Ga edges. The radial space windows of 1.9-3 Å was used for both edges. The amplitude reduction factor S_0^2 and the threshold energy E_0 were acquired from InSb and GaSb and were maintained constant while fitting the ternary compounds. Whereas the coordination number of four was set for the first NN shell, the interatomic distance and Debye-Waller factor were floated for all scattering paths to fit this shell.

3.5 SCANNING ELECTRON MICROSCOPY

Unlike optical microscopy, in which the image is produced through reflected or transmitted light, in scanning electron microscopy (SEM) it is not necessarily the electrons reflected by the surface of the sample, the so-called backscattered electrons, that give rise to the observed image. In most applications, so-called secondary electrons are used for this purpose. A schematic diagram of a modern SEM is shown in Figure 3.10.

Figure 3.10- Simplified scheme of the SEM components.

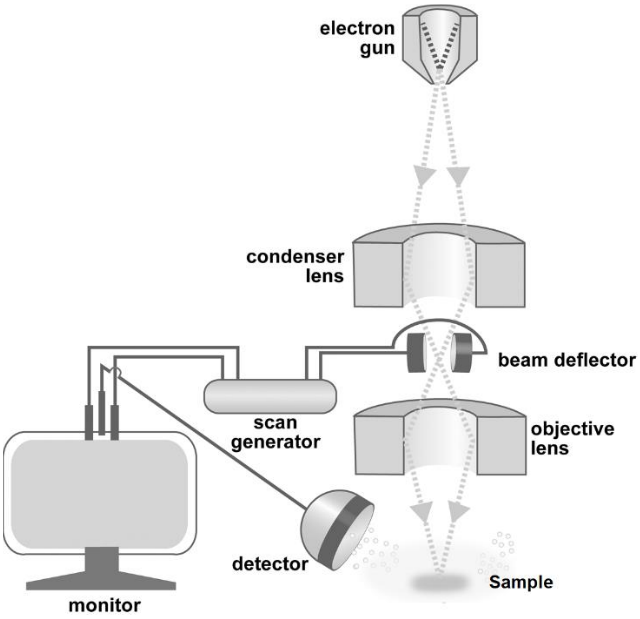

Reference: adapted from (SCHATTEN, 2013).

The instrument has an electron gun, the source of primary electrons. These electrons are accelerated by a potential difference and focused on the material under study. A set of electromagnetic lenses allows the electrons to converge through the vacuum chamber. They play a role for electrons similar to that of ordinary lenses in relation to light. In the absence of these lenses, the primary electrons would diverge, many of them crashing against the instrument's walls.

The electromagnetic lens system, responsible for the convergence of the electron beam, is nothing more than a set of coils in which an electric current circulates which is controlled by the electron microscope operator. By varying the current of these coils, it is possible to sweep the electron beam over the entire surface of the sample, hence the name scanning electron microscope.

Once impinged on the surface of the sample, the beam of primary electrons produces secondary electrons. The stripped electrons are collected by a detector and the resulting signal is amplified, digitized and stored as a numerical value in the corresponding computer memory. Subsequently, the digital image is transformed (converting the numerical values stored in the computer into an analog signal) for viewing on a TV monitor.

The scan of the image on the tv monitor is kept synchronized with the scan of the primary electron beam incident on the surface of the sample. This means that each point on the screen corresponds to a point on the surface of the sample swept by the primary electron beam, which is proportional to the signal intensity captured by the detector at each specific point. The image that is formed on the TV monitor makes it possible to distinguish the surface relief due to the contrast differences observed on the screen (Figure 3.11). The topography of the examined surface is done through the same procedure that the brain uses, that is, it processes the information coming from the two eyes, producing depth perception. In the case of the electron microscope, two images of the sample are taken with angles of inclination in relation to the incident primary electron beam differing by a few degrees, to simulate the visual parallax. The surface topography is then reproduced from photographs of the images. In more sophisticated SEM systems, the three-dimensional image is obtained through a computerized data acquisition and processing system (EGERTON, 2005), (VALADARES, 1992).

Figure 3.11- SEM image of an InSb sample irradiated with fluence of 1x10^{14} cm^{-2}.

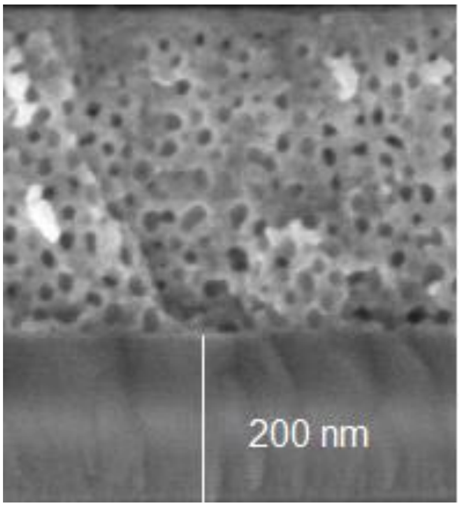

3.5.1 Experimental details

A Carl Zeiss Auriga FEG-SEM microscope was used for acquiring SEM images. The microscope was equipped with in-lens SE detector and the micrographs were registered using low electron beam energy (1–5 keV) to minimize possible modifications induced by the electron beam on the porous films. A FEI Verios FEG-SEM operated at 5 kV, with an in-lens SE detector was also used.

3.6 FOUR-POINT-PROBE TECHNIQUE: RESISTIVITY

The bulk resistivity is an intrinsic electrical property related to carrier drift in materials such as metals and semiconductors. Resistivity is one of the most important electrical parameters of semiconductors. With the measurement of this parameter as a function of temperature is possible to classify materials into metals, semiconductors and isolators (SAFA KASAP; PETER CAPPER, 2017).

The resistivity is given by:

$$\rho = \frac{RA}{L}, \tag{9}$$

where R is the bulk resistance, A is the cross-sectional area and L is the distance between the two probes shown in Figure 3.12.

For thin semiconductor layers, the sheet resistivity ρ_s is often used instead of the bulk resistivity. The sheet resistivity is the bulk resistivity divided by the sample's thickness t. This normalized parameter is related to the resistance of a square of side L. For this particular geometry $\rho_s = R_s$, the sheet resistance. The measure of this parameter is the lateral resistance through a thin square of material, i.e. the resistance between opposite sides of a square. The key advantage of sheet resistance over other resistance measurements is that it is independent of the size of the square - enabling an easy comparison between different samples. Another advantage is that it can be measured directly using a four-point probe technique.

The four-point probe method, also known as the Kelvin technique, is the primary technique for measuring sheet resistance. A four-point probe consists of four electrical probes in a line, with equal spacing between each of the probes as shown in Figure 3.12. It operates by applying a current (*h*) on the outer two probes and measuring the resultant voltage drop between the inner two probes. The sheet resistance and resistivity, respectively, can then be calculated using the equations below:

$$R_S = 4.532\,\frac{V}{h}\,; \tag{10}$$

$$\rho = 4.532\,t\frac{V}{h}\,. \tag{11}$$

The equations (10) and (11) are corrects for a thin semiconductor wafer or thin semiconducting layer deposited on an insulating substrate, and for the condition *t* < *s*/2, which represents most practical cases because the probe spacing *s* is usually on the order of a millimeter(SAFA KASAP; PETER CAPPER, 2017).

Figure 3.12- A schematic diagram of a four-point probe. The four probes have equal spacing (s) and are shown in contact with a surface. A current (I) is injected through probe 1 and collected through probe 4, whilst the voltage is measured between probes 2 and 3.

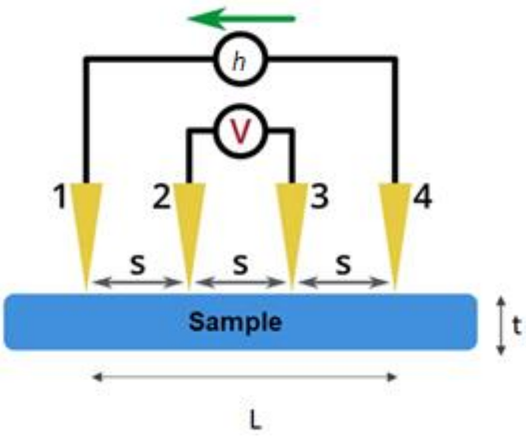

3.7 SEEBECK EFFECT AND THE FIGURE OF MERIT ZT

If a single conducting rod is heated on one end and cooled on the other, the electrons on the hot end are more energetic and have greater velocities than electrons on the cold end. Therefore, the electrons on the hot end diffuse to the cold end until the developing electric field prevents further diffusion. The diffusion of electrons gives the conducting rod an increased negative electron concentration at the cold end, leaving some uncompensated positive ions at the hot end. A voltage potential difference, therefore, results with the hot end at a positive potential due to lower electron density (Figure 3.13). This phenomena is known as Seebeck effect. In metals, valence electrons are the charge carriers, and in semiconductors, both valence electrons and holes are the charge carriers.

It is interesting to notice that a voltage is measured only during the time when charge carriers have diffused from one material to the other but when the material has not reached a uniform temperature. Therefore, for a material to have a large thermoelectric effect, it must have a large electrical conductivity and small thermal conductivity.

Figure 3.13- Simple schematics of measurement of the Seebeck effect, drawn for electron-like charge carriers.

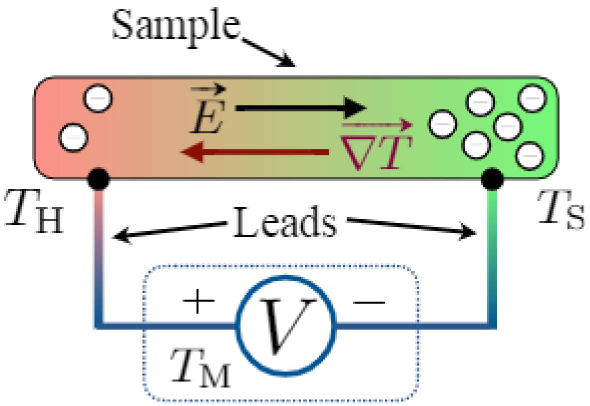

Reference: adapted from (MASON et al., 2020)

Highly-efficient thermoelectric materials are important for power generation devices that convert waste heat into electrical energy. Compared to conventional power generators, which convert thermal energy into mechanical energy then to electrical energy, thermoelectrics own many advantages such as less noise, no pollution, no moving parts, and greater reliability(ZHENG et al., 2014)(YANG et al., 2018). The conversion of waste heat into electrical energy plays a key role in our current challenge to develop alternative energy technologies to reduce our dependence on fossil fuels and to reduce greenhouse gas emissions.

With that in mind, $In_xGa_{1-x}Sb$ films were tested as possible thermoelectrics (TE). The thermal conductivity of InSb, GaSb and AlSb binaries is high (17, 33 and 60 W/mK at 300 K, respectively), hence, they are usually considered as low-efficient materials for TE applications. Recently, however, the enhanced TE performance of $In_xGa_{1-x}Sb$ by nanoinclusion of gallium (x up to 0.15) has shed light on high-mobility semiconductors for TE applications (ZHANG et al., 2011). An important aspect to be considered for TE materials is the potential to convert heat into electricity, usually measured by the dimensionless figure of merit ZT(MINNICH et al., 2009), which represents the conversion efficiency of thermoelectric materials defined as follows:

$$ZT = \frac{S^2 \sigma T}{k} = \frac{S^2 T}{k\rho} = \frac{S^2 T}{(k_e + k_l)\rho}, \tag{12}$$

where S is the Seebeck coefficient, σ and k are the electrical and thermal conductivity, respectively, T is the absolute temperature, ρ is the electrical resistivity, and thermal conductivity (k) of thermoelectric materials consists of two parts: lattice thermal conductivity (k_l) and electronic thermal conductivity(k_e). The S, is the voltage, V, induced between two points in a material under a temperature gradient, divided by the temperature difference, ΔT, between the two points such that

$$S = -\frac{\Delta V}{\Delta T} - S_p, \tag{13}$$

where S_p is the parasitic Seebeck voltages from the probes themselves thus it is common to report Seebeck data with respect to the lead material (BAHK; FAVALORO; SHAKOURI, 2013). The relative S value, considering the material used in the measuring probes, can be measured by the equipment developed in this work (see section 3.7.1). Since it is necessary to obtain the voltage value, data acquisition requires only two probes.

3.7.1 Experimental details

The electrical and thermoelectric characteristics of the materials were measured with the aid of an equipment specially developed for this purpose (ROSSETTO, 2021) (see Figure 3.14) and will be described briefly as follow. Figure 3.15 shows in detail the structure for specimen fixation (specimen holder). It consists of parts such as holder for clamping samples and probes for measuring voltage and current. The two blocks (masses) positioned above the sample serve as the surface cooling and surface warming mass, and the block under the sample, global warming. Also arranged are two surface temperature sensors and the heating mass selector switch.

The device has two heating controls for monitoring samples when subjected to different temperatures. One of them is the base (lower) control, to obtain resistivity values as a function of temperature. In this control, an overall mass, located under the sample, fully heats the sample, including its substrate. With it, it is possible to determine the behavior of the electrical resistivity of the semiconductor(AVIA, 2017), as it allows the measurement of voltage and current when the sample is subjected to different temperatures. On the other hand, the surface control (upper) is intended for the acquisition of the coefficients of the ZT parameter. In this control, the equipment generates a thermal difference between two generic points on the sample surface and, from this temperature gradient, measures the voltage difference between the same points, in addition to the electrical power used for this, which is converted into thermal power and applied directly to the sample. To amplify the thermal gradient and increase the temperature resolution, samples were measured under negative pressure (10^{-2}mbar), which reduces heat loss by convection, improving the thermal transfer by conduction. For the thermal conductivity measurements, the thickness of the films was determined by scanning electron microscopy, as reported in appendix B. The choice of which control to use is made using the sampler selector switch (Figure 3.15). Both can have the temperature rise ramp (degrees Celsius per minute) set as needed.

Figure 3.14 - Schematic diagram of the complete structure of the equipment and photo with the indicative parts. (I) electronics, (II) measuring base, (III) sealed chamber, (1) AC voltage selector, (2) USB port, (3) on/off switch, (4) protection fuse, (5) signal input and auxiliary power, (6) control buttons, (7) LCD display, (8) cooling fan, (9) injection current adjustment, (10) feed-throughs, (11) cap/seal , (12) valve for meter and (13) gas inlet valve.

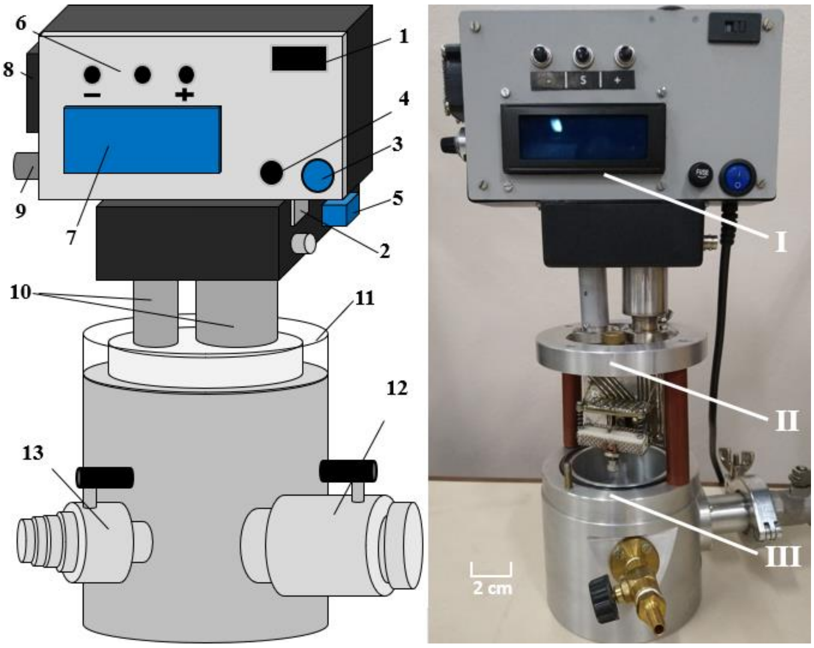

Reference : (ROSSETTO, 2021)

Figure 3.15- Schematic diagram of the structure for specimen fixation. (1) heating selection switch, (2) measuring probes, (3) surface cooling mass, (4) temperature sensors, (5) sample clamp, (6) surface heating mass and (7) heating mass global.

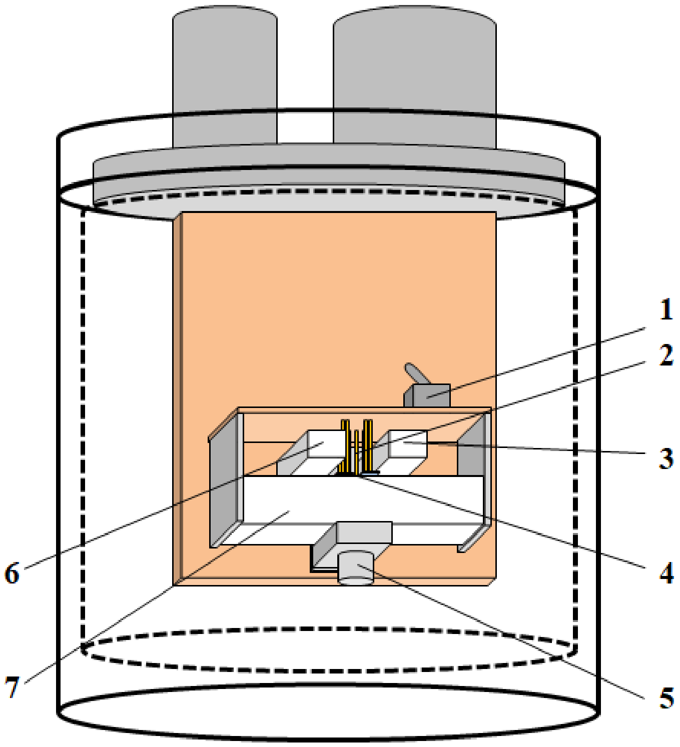

Reference: (ROSSETTO, 2021)

4 CHARACTERIZATION OF $In_xGa_{1-x}Sb$ FILMS: RESULTS AND DISCUSSIONS

$In_xGa_{1-x}Sb$ films deposited by magnetron sputtering were structurally characterized using RBS, PIXE, GIXRD and SEM techniques, described in chapter 3, before and after irradiation with Au^{+7} ions. The thermoelectric characterization of unirradiated and irradiated $In_xGa_{1-x}Sb$ films were performed using an equipment specially developed for this purpose(ROSSETTO, 2021).

Firstly, the local atomic-structure of $In_xGa_{1-x}Sb$ ternary compounds were investigated considering only the change in In/Ga concentration ratio. Afterwards, a second variable was added, the irradiation fluence, and its effect on the films was studied for different concentrations. A similar approach was used for the thermoelectric characterization.

In this chapter, it is presented the characterization of $In_xGa_{1-x}Sb$ ternary compounds from atomic-scale to nanoscale structure before and after ion irradiation. Subsequently, thermal stability and thermoelectric properties of these ternaries are also shown.

4.1 $In_xGa_{1-x}Sb$: THE EXTENDED ATOMIC PICTURE BEFORE AND AFTER ION IRRADIATION

For $In_{1-x}Ga_xSb$ films, GIXRD results are presented in Figure 4.1, with the corresponding crystallographic planes indicated above each peak. The formation of polycrystalline zincblende phase can be seen in as-deposited films (shown on the right of Figure 4.1). Diffractograms from different stoichiometries are vertically offset for clarity. All films exhibit the same set of diffraction peaks (same crystalline structure); however, there is a clear shift in diffraction angle with increasing Ga concentration, which can be easily seen in Figure 4.2-(a), where a highlight of the (220) diffraction peak of Figure 4.1 is shown. The displacement in angle with increasing Ga concentration is due to the decrease in lattice parameter promoted by the shorter atomic distances of the Ga-Sb bonds compared to those of the In-Sb bonds in the $In_xGa_{1-x}Sb$ films. This behavior is also known as alloying effect, which is described by the virtual crystal approximation (VCA) (Figure 4.2-(b)), where each atom is considered to be located at the ideal lattice site. In this model, the corresponding pair of neighboring atoms have identical bond lengths, which change linearly (as predicted by Vegard`s law) with composition x. GIXRD data were analyzed and the main structural parameters for $In_xGa_{1-x}Sb$ films are listed in Table 4.1. Lattice parameter and bond length were estimated with the Powder Cell (GIULIAN et al., 2019) software, while crystallite size and microstrain were manually calculated using the Scherrer equation (B.D.CULLITY e S.R.STOCK, 2014) and the Williamson-Hall method (ZAK et al., 2011), respectively.

Table 4.1– Structural parameters from x-ray diffraction analysis, where a is the lattice parameter, size is the crystallite size. The uncertainty in all values is on the last digit.

Sample	a(Å)	Size	Strain	Bond length(Å)
InSb	6.480	28.8	0.0019	2.805
$In_{0.8}Ga_{0.2}Sb$	6.387	42.3	0.0013	2.758
$In_{0.6}Ga_{0.4}Sb$	6.333	31.6	0.0027	2.742
$In_{0.5}Ga_{0.5}Sb$	6.279	29.3	0.0025	2.722
GaSb	6.102	18.5	0.0015	2.642

Figure 4.1 X-ray diffraction patterns of $In_xGa_{1-x}Sb$ films. Diffractograms from films with different stoichiometries are vertically offset for clarity. In highlight, it is shown the schematic zincblende structure of all films.

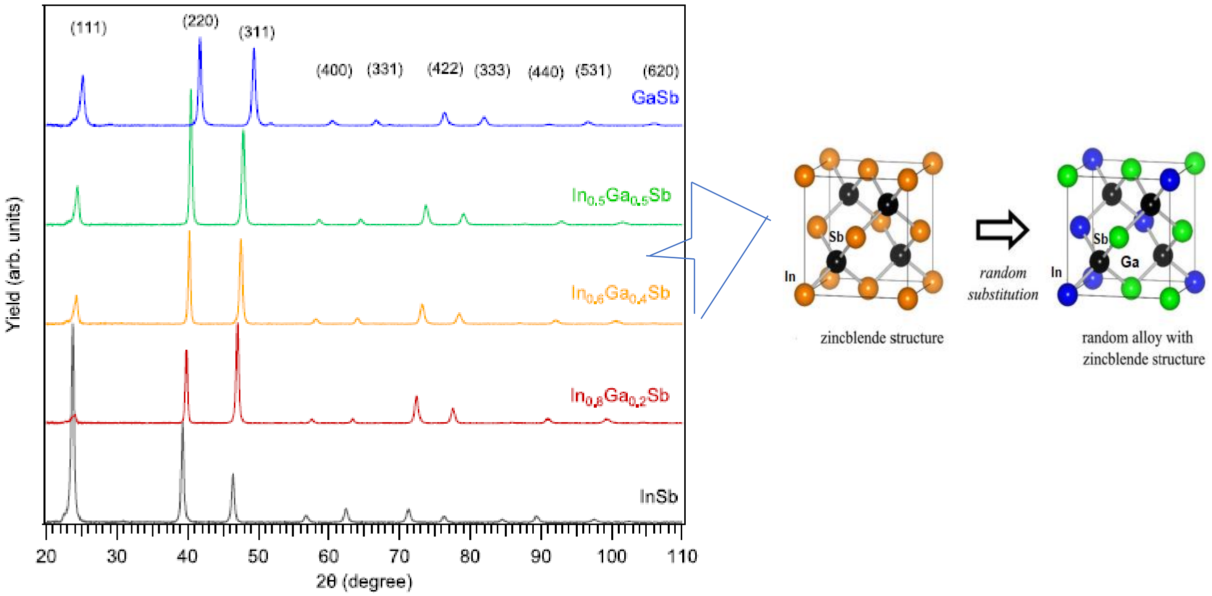

Figure 4.2-(a) Highlight of Figure 4.1 depicting the (220) diffraction peak of In$_{1-x}$Ga$_x$Sb films. (b) alloying effect describe by VCA model.

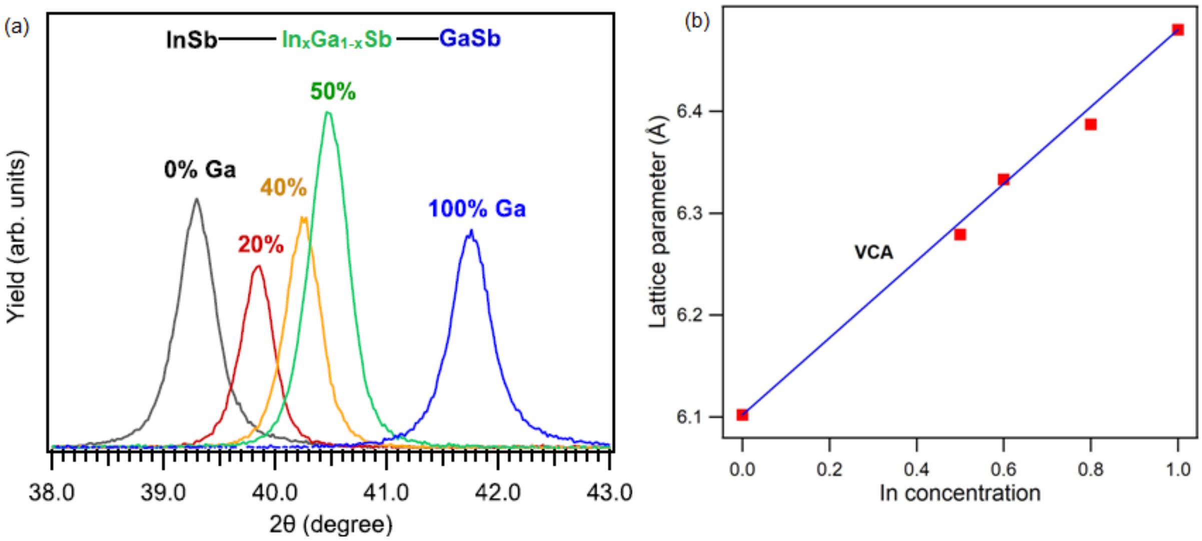

Regarding the variations in irradiation fluence, Figure 4.3 shows GIXRD results for three representative samples, In$_{0.8}$Ga$_{0.2}$Sb, In$_{0.6}$Ga$_{0.4}$Sb and In$_{0.5}$Ga$_{0.5}$Sb films, as-deposited and after irradiation with 16 MeV Au^{+7} ions to a total fluence of 2x10^{14} cm^{-2}. There is a clear reduction in amplitude for the diffraction peaks (after irradiation), for the In$_{0.5}$Ga$_{0.5}$Sb sample, with no change in lattice parameter. The increase in full width at half maximum (FWHM) of the peaks indicate a decrease in crystallite size as discussed in the next paragraph. For the In$_{0.8}$Ga$_{0.2}$Sb sample (and similarly for the In$_{0.6}$Ga$_{0.4}$Sb one), the same irradiation conditions result in the complete amorphization of the material. Counterintuitively, InSb films irradiated under similar conditions exhibit a reduction in crystallite size, but still retaining part of their crystallinity (GIULIAN et al., 2017b), while GaSb films can be easily amorphized by ion irradiation (MANZO et al., 2019). With that in mind, the expected results would be that the ternary compounds with the higher In concentration should exhibit the highest levels of crystallinity upon irradiation as suggested by Vegard’s law, however, the results in Figure 4.3 show the opposite. The resistance of semiconductors to amorphization may be related to their fundamental properties, such as the type of chemical bonding (TRACHENKO, 2004). This factor is empirically measured via Phillip`s ionicity (*p*), which is defined as the chemical bond ionicity. Materials with $p>0.47$ are non-amorphizable, while materials with $p<0.47$ may be amorphized (NAGUIB; KELLY, 1975). According to Adachi (ADACHI, 2009), $p = 0.321$ and 0.261, for InSb and GaSb, respectively, which means both compounds can be amorphized using an appropriate ion irradiation fluence, a result that was achieved only for GaSb within the range of irradiation fluences used in the present work. Concerning the amorphization of the ternary $In_xGa_{1-x}Sb$, a similar behavior was observed for $In_xAl_{1-x}Sb$ (BOLZAN et al., 2021c), $In_xGa_{1-x}As$ (HUSSAIN et al., 2009) and $In_xGa_{1-x}P$ (HUSSAIN et al., 2016) at 300 K, where it was shown that it is easier to amorphize the ternary compound than its binary counterparts. As reported by Hussain *et al.*, this phenomenon may be connected with the structure disorder in ternary alloys, resultant of lattice mismatch of two different binaries, serving as preferential sites for stimulated amorphization. It is worth mentioning, nonetheless, that $In_xGa_{1-x}As$ and $In_xGa_{1-x}P$ measured at 15 K exhibit the standard behavior observed for a ternary compound, which is an intermediate result of that observed for its two binary compounds.

The crystallite size for $In_{0.5}Ga_{0.5}Sb$ sample as-deposited (irradiated with 2×10^{14} cm^{-2}) is 29.3 nm (18.4 nm) with a microstrain of 0.00255 (0.00583). The decrease in crystallite size and increase in microstrain is consistent with the ion irradiation-induced defects, also observed in other antimonides irradiated under similar conditions (MANZO et al., 2019)(DE ANDRADE et al., 2017)(GIULIAN et al., 2019). InGaSb films deposited by magnetron sputtering with thickness 560 nm, nearly stoichiometric ($In_{0.24}Ga_{0.27}Sb_{0.49}$), show average crystallite size of 140 nm, with strong preferential orientation along the [220] direction (NISHIMOTO; FUJIHARA, 2019).

Figure 4.3- X-ray diffraction analysis of $In_xGa_{1-x}Sb$ films, before and after irradiation with 16 MeV Au^{+7} ions to a total fluence of $2x10^{14}$ cm^{-2}.

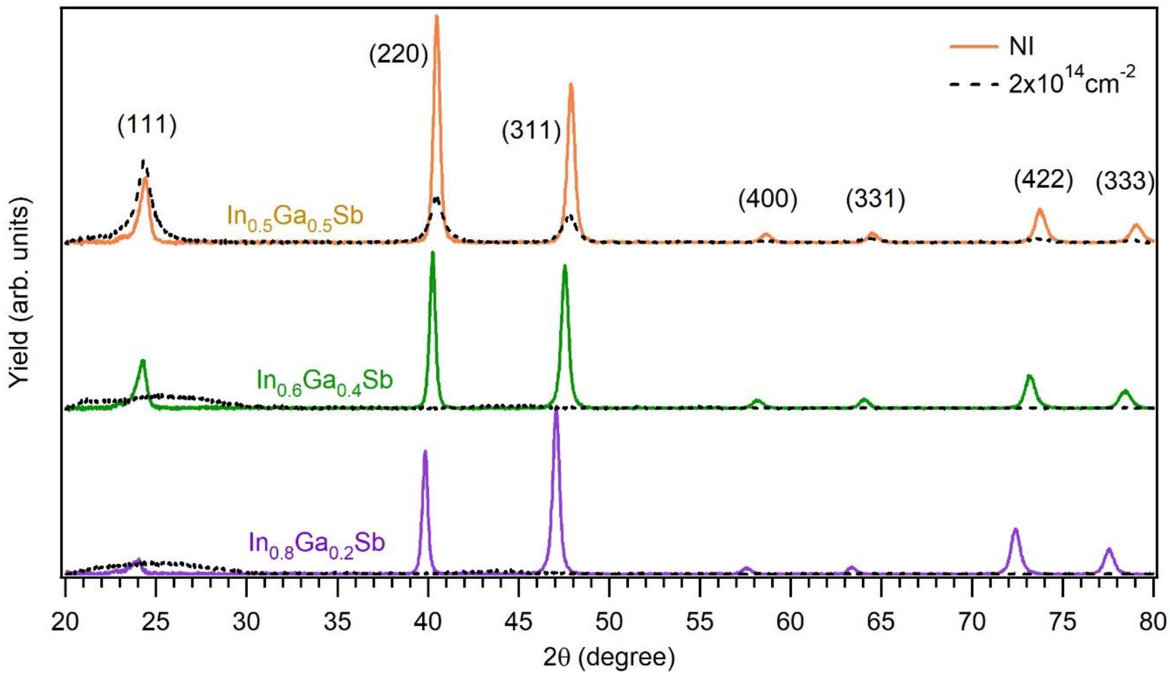

4.2 $In_xGa_{1-x}Sb$: THE LOCAL ATOMIC PICTURE BEFORE ION IRRADIATION

For room-temperature, k^3-weighted EXAFS oscillations measured at the In and Ga K-edges are shown in Figure 4.4-a and Figure 4.4-b as a function of the photoelectron wavenumber, exhibiting the oscillation behavior of zincblende polycrystalline $In_xGa_{1-x}Sb$, previously observed through x-ray diffraction (Figure 4.1). Fourier-transformed spectra and the respective fits are presented in Figure 4.4-c and Figure 4.4-d. For the In edge, the R-factor of the fittings was 0.004, 0.004, 0.002 and 0.004, for $In_xGa_{1-x}Sb$ films with x = 0.5, 0.6, 0.8 and 1, respectively. For the Ga edge, the R-factor of the fittings was 0.007, 0.01, 0.02 and 0.02 for x = 0, 0.5, 0.6 and 0.8, respectively. As reported by Newville(NEWVILLE, 2014), the value of this factor is typically found to be below 0.05 for good fits in agreement with our values and the high quality of the fits observed from Figure 4.4.

Figure 4.4-(a), (b) k^3-weighted EXAFS spectra of $In_xGa_{1-x}Sb$ for In (left) and Ga (right) K-edges as a function of the photoelectron wavenumber. The corresponding Fourier transform spectra of $In_xGa_{1-x}Sb$ for four different In/Ga ratio concentrations at: (c)In K-edge and (d) Ga K-edge.

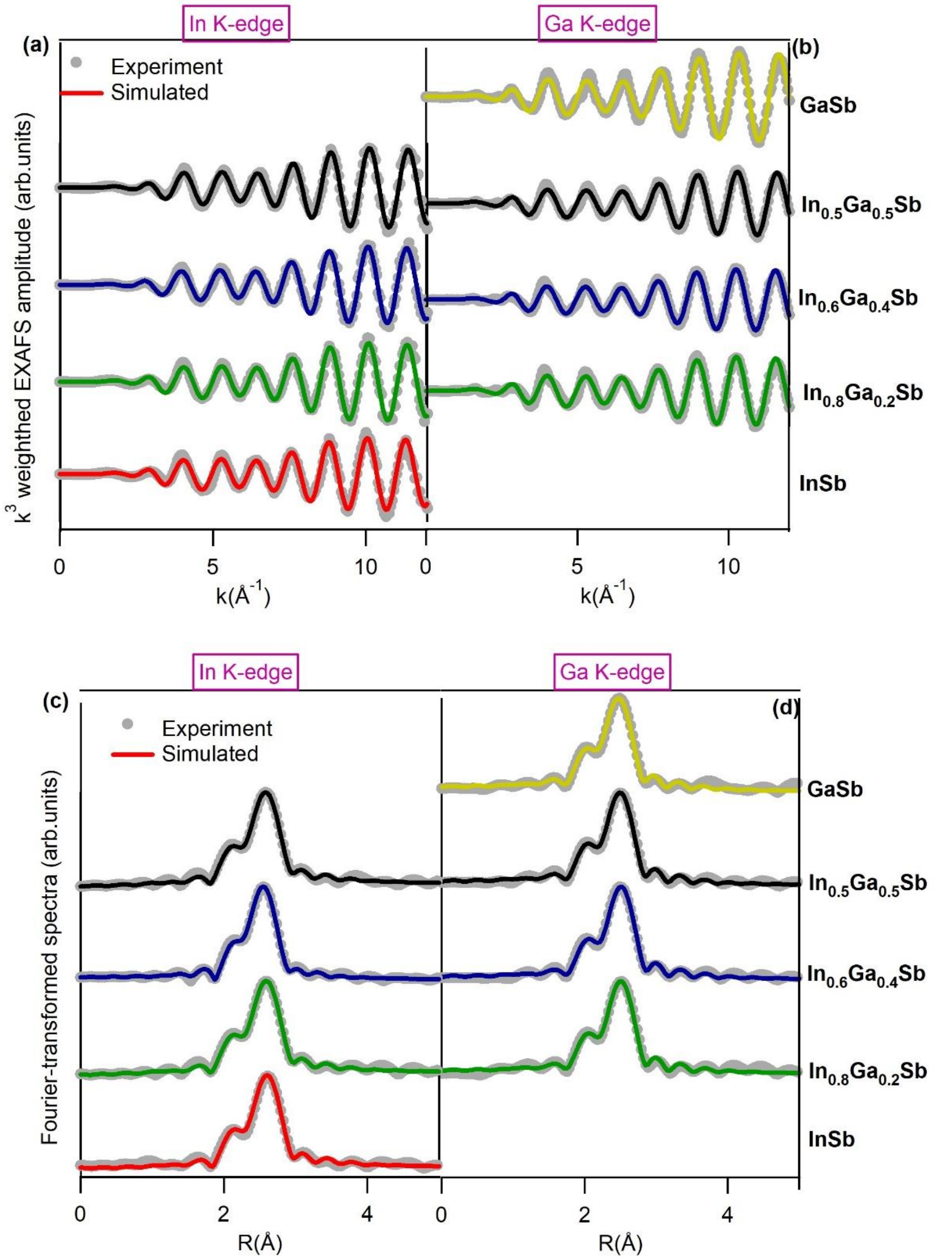

Table 4.2 summarizes the structural parameters for the first shell measured at In and Ga K edges. Figure 4.5 shows the interatomic distance for the mentioned shell as a function of In concentration x. From this figure, it is possible to see that the values of average cation-anion distances remain closer to the respective binary parent compounds than to the ones predicted by the VCA model. In fact, the nearest-neighbor (NN) distances differ by approximately 20% and 18% from the VCA for In-Sb and Ga-Sb, respectively. However, the weighted average of In-Sb and Ga-Sb bond lengths are in agreement with the prediction of the VCA model. The bimodal bond length

distribution in $In_xGa_{1-x}Sb$ ternary alloys was also reported by Boyce *et al.* (BOYCE; MIKKELSEN, 1989) and Hosokawa *et al.* (HOSOKAWA et al., 2009). The Debye-Waller factors are constant within experimental uncertainty (Table 4.2). Considering the first NN shell, the ternary thus resembles a mixture of the binary atomic environments, having two distance distributions corresponding to In-Sb and Ga-Sb bonds, with mean values and widths similar to those of the binary compounds.

Figure 4.5**-** Interatomic distance of $In_xGa_{1-x}Sb$ ternary alloys for the first NN around In and Ga atoms. *Experimental results*: The values for the In-Sb and Ga-Sb pair are denoted by full circles and squares, respectively. The open dots represents the virtual-crystal approximation and the dash lines denote the Pauling limit. *Theoretical calculations*: The solid lines correspond the best fit yielding ϵ=0.79±0.03 and ϵ=0.82±0.02 for the dilute limit GaSb:In and InSb:Ga, in this order. The stars are relative to the calculations by Balzarotti *et al.* (BALZAROTTI et al., 1985).

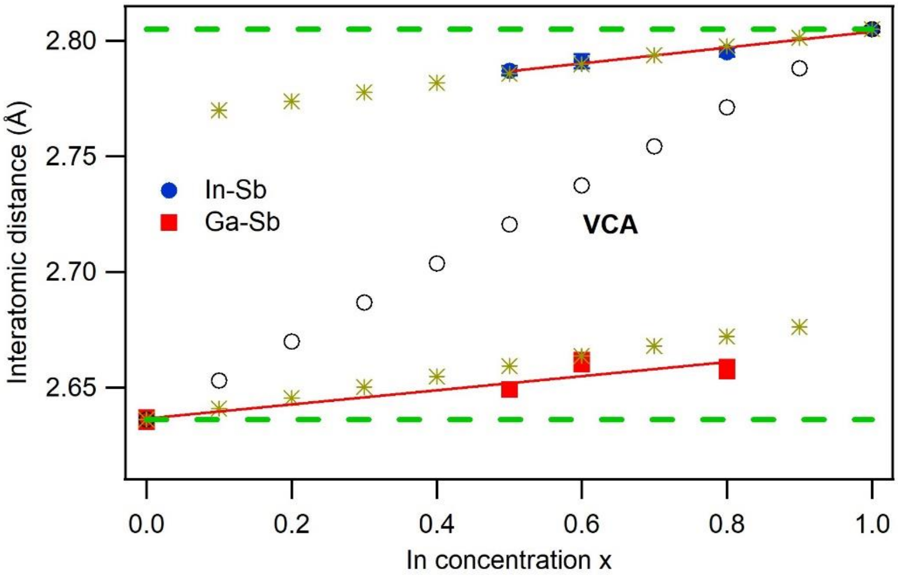

Table 4.2- Interatomic distances obtained from EXAFS measured at the In and Ga K-edges of $In_xGa_{1-x}Sb$ films.

	Interatomic distance(Å)		Debye-Waller factor (10^{-3} A^2)	
	In K-edge	Ga K-edge	In K-edge	Ga K-edge
	1stNN Sb	1stNN Sb	1stNN Sb	1stNN Sb
InSb	2.805±0.002		5.3±0.1	
$In_{0.8}Ga_{0.2}Sb$	2.795±0.003	4.658±0.004	5.3±0.2	4.4±0.5
$In_{0.6}Ga_{0.4}Sb$	2.791±0.002	2.661±0.004	5.1±0.2	4.2±0.4
$In_{0.5}Ga_{0.5}Sb$	2.787±0.001	2.649±0.003	5.2±0.2	4.0±0.4
GaSb		2.636±0.004		3.8±0.4

The bimodal bond length distribution in unstrained ternary alloys is a common behavior reported on a large number of other III-V and II-VI ternary zincblende alloys, such as $In_xAl_{1-x}Sb$ (BOLZAN et al., 2021d) and $Cd_{(x)}Zn_{(1-x)}Te$ (KOTESKI et al., 2004), well-known as cation-mixed systems, and in the anion-mixed systems as $GaAs_{(x)}P_{(1-x)}$ (WU et al., 1993) and $ZnTe_{(x)}Se_{(1-x)}$ (PELLICER-PORRES et al., 2004). This bond length distribution behavior is not specific to ternary alloys with zincblende structure. Both nitrite alloy systems $Ga_{(1-x)}Al_{(x)}N$ and $In_xGa_{1-x}N$, which crystallize in the wurtzite structure, also show the bimodal bond length distribution with their corresponding first nearest-neighbor distances again much closer to their respective binary values than to the ones predicted by the VCA model (KACHKANOV et al., 2006; KATSIKINI et al., 2003; MIYANO et al., 1997; YU et al., 1999).

4.2.1 Theoretical predictions and bandgap bowing correlation

There are many theoretical models to describe the bimodal distribution presented by the 1^{st}NN shell of $B_{(x)}A_{(1-x)}C$ zinc blende ternary alloys. All of them are compared via a dimensionless relaxation parameter (ϵ) defined as follow:

$$\varepsilon_A = ({d^{dil}}_A - {d^{bin}}_B)/({d^{bin}}_A - {d^{bin}}_B), \tag{14}$$

where ${d^{dil}}_A$ is the impurity-anion distance in the host crystal and ${d^{bin}}_A$ or ${d^{bin}}_B$ represent the host bond length. The limit $\varepsilon = 0$ (no relaxation) corresponds the VCA model, in which the alloy is thought of as sustaining a single average chemical bond, whereas the Pauling limit $\varepsilon = 1$ (complete relaxation) is when the alloy is thought of as sustaining two different chemical bonds that are equal to their ideal binary values (see Figure 4.5). Table 4.3 shows the ϵ values calculated through different models for $In_xGa_{1-x}Sb$ ternary compounds.

The model of Shih *et al.* (SHIH et al., 1985) considers that tetrahedral symmetry around the impurity, embedded in the host matrix, is preserved in the calculation of impurity-anion bond length. Also, the 1^{st}NN interaction is assumed to be a simple spring, whose force constant is independent of bond types. Thus, the relaxation parameter is dependent only on the crystal geometry, being $\varepsilon = 0.75$ for zincblende structure. More elaborated models (MARTINS; ZUNGER, 1984) consider the relaxation of the first two shells around the impurity, assuming the transferability of the binary force constants to ternary alloy systems with the deformation energy caused by the insertion of the impurity in the host matrix modeled by valence force field (VFF) potentials of Keating. Although the hypothesis of the transferability of the force constants reported good results, recent studies suggest that this is not necessarily valid (ECKNER et al., 2018). Shen (SHEN, 1994) obtained the relaxation parameter through the bond orbital model. Chen and Sher (CHEN; SHER, 1985) also incorporate the chemical effects in it, besides the distortion energy due to substitution of an isoelectronic atom A for a B in the host zincblende compound BC, evaluated using VFF. More details of these and other theoretical models can be found somewhere else (SCHNOHR, 2015).

Table 4.3 - Values of ε using different models. GaSb:In denotes the case of In impurities in GaSb while InSb:Ga refers to the Ga impurities in InSb. The last line is the value determined experimentally using equation (1).

Theoretical Model	Ref.	GaSb:In	InSb:Ga
Shih *et al.*	(SHIH et al., 1985)	0.75	0.75
Matins and Zunger	(MARTINS; ZUNGER, 1984)	0.60	0.74
Shen	(SHEN, 1994)	0.72	0.78
Cai and Thorpe	(CAI; THORPE, 1992)	0.68	0.76
Chen and Sher	(CHEN; SHER, 1985)	0.69	0.76
Balzarotti *et al.*	(BALZAROTTI et al., 1985)	0.77	0.73
Boyce *et al.*	(BOYCE; MIKKELSEN, 1989)	0.78 ± 0.05	0.79 ± 0.05
Hosokawa *et al.*	(HOSOKAWA et al., 2009)	0.79 ± 0.05	0.87 ± 0.05
This work		0.79 ± 0.03	0.82 ± 0.02

It is important to discuss the bond length distribution in more details, because it is the variable that is correlated with other properties such as refractive index and bulk modulus, as reported by Reddy *et al.* (REDDY et al., 2003) and Cohen(COHEN, 1985). The VCA model indicates that the impurity bond length is relaxed in the host lattice solely by bond stretching while Pauling limit model is only by bonding bending. Table 4.3 shows that the relaxation parameter values are between 0.60 and 0.87, for $In_xGa_{1-x}Sb$, including the ones acquired from theoretical models, evidencing that the lattice mismatch in ternary compounds is accommodated favorably through bond bending over bond stretching. This behavior is common among the III-V cation-mixed alloys ($B_{(x)}A_{(1-x)}C$), whose values of ε are mostly between 0.75 and 0.85 (SCHNOHR, 2015). It should be noted that the majority of the models establish for the dilute limit InSb:Ga and GaSb:In two different values of ε owing to the distinct force constants of the respective binary compounds, in accordance with results of this work. Cai and Thorpe (CAI; THORPE, 1992) also predict a slight bowing in the bond length of a few ternary alloys such $Cd_{(x)}Zn_{(1-x)}Te$ due to a force constant disorder. However, this behavior was not observed in $In_xGa_{1-x}Sb$ (see Figure 4.5).

From all models presented in Table 4.3, the model by Balzarotty et al. can estimate unambiguously the structural and electronic contributions to the bandgap bowing via the magnitude of the average cation-anion distances in the first NN bimodal distribution for the whole compositional range. Although an explanation regarding this model can be found elsewhere (SCHNOHR, 2015), a brief consideration of Balzarotti et al. (BALZAROTTI et al., 1985) model is presented in appendix A. The bandgap bowing of ternary alloy semiconductors have long been known to be correlated with changes in the microscopic atomic structure of the alloy (ZUNGER; JAFFE, 1983)(HASS; LEMPERT; EHRENREICH, 1984) and electronic effects resultant of charge redistribution between the anion and the two different cations. As reported by Schnohr (SCHNOHR, 2012), the total bandgap bowing ($\Delta E=\Delta E_{struc}+\Delta E_{elec}$) can be defined, hence, as the sum of the structural (ΔE_{struc}) and electronic contributions (ΔE_{elec}) with the corresponding bowing parameter as $b = b_{struc}+b_{elec}$. The structural contribution ΔE_{struc} can be calculated using the model by Balzarotti et al.. Figure 4.6 shows ΔE_{struc} and the experimentally determined ΔE values for $In_xGa_{1-x}Sb$ (ADACHI, 2009). From this figure, the ΔE_{struc} contribution is significant to the total bandgap bowing, however, it does not cover the full magnitude of it. The remaining bandgap bowing corresponds to ΔE_{elec} which also constitutes a significant contribution to ΔE. Hence, structural and electronic effects both contribute to the bandgap change in a similar way and neither local atomic arrangements nor charge redistribution can be neglected. A similar result was obtained for $In_xGa_{1-x}P$ (SCHNOHR, 2012).

Figure 4.6- Bowing of the bandgap versus composition x for $In_xGa_{1-x}Sb$. The shaded area corresponds the range of experimental values reported in the literature together with the average values (ΔE^{av}) exposed in Ref (ADACHI, 2009). The bowing structural contribution is plotted as blue squares whist the electronic contribution is represented by the black arrow.

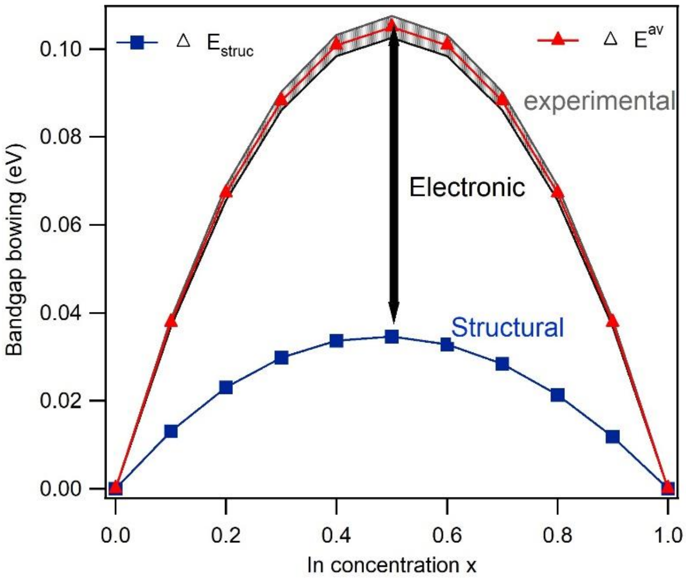

4.3 $In_xGa_{1-x}Sb$: THE LOCAL ATOMIC PICTURE AFTER ION IRRADIATION

Since the behavior of InSb upon ion irradiation is similar to GaSb and $In_xGa_{1-x}Sb$ compounds, InSb results are shown firstly as follows. The results are shown for samples irradiated with 14 MeV Au^{+6} ions at room temperature, normal incidence, with ion fluences ranging from 1×10^{13} cm^{-2} to 2×10^{14} cm^{-2}. EXAFS measurements were performed at 8 K temperature. Figure 4.7-(a) and (b) show the k^2- weighted EXAFS spectra and the respective fittings for In and Sb K-edges as a function of the photoelectron wavenumber, showing that the EXAFS oscillations from the polycrystalline, unirradiated InSb, slightly diminish with increasing irradiation fluence, but are still present in samples irradiated with fluences up to $2x10^{14}$ cm^{-2}. Figure 4.7-(c) and (d) show Fourier transformed EXAFS spectra for In and Sb K-edges as a function of the non-phase-corrected radial distance R at different fluences. For both edges, the presence of three prominent peaks below R~5.5 Å is characteristic of the first three atomic shells in the zincblende structure. The decrease in amplitude with increasing ion fluence is consistent with the introduction of irradiation-induced disorder, however, no evidence of complete amorphization in the atomic-scale was observed for fluences up to 2×10^{14} cm^{-2} , in agreement with previous work (BOLZAN et al., 2021a). Additional peaks become apparent in the In and Sb spectra at R~1.8 Å and R~1.4 Å, respectively, for the highest fluence used in this work. These oxides were not taken into account in the EXAFS analysis due to their small contributions (BOLZAN et al., 2021b).

Table 4.4 and Table 4.5 summarize the structural parameters obtained via EXAFS fittings for the first three shells of InSb measured at both In and Sb edges. The uncertainties were obtained from the non-linear least-squares fits to the experimental data. For the In edge, the R-factor of the fittings was 0.01, 0.009, 0.007, 0.007 and 0.02, for In-Sb films irradiated with fluences of 0, 1×1013 cm-2, 5× 1013 cm-2, 1×1014cm-2 and 2 × 1014 cm-2, respectively. For the Sb edge, the R-factor of the respective fittings was 0.01, 0.01, 0.01, 0.03 and 0.01.

Figure 4.8 (a), (c) and (e) show the corresponding atomic-scale behavior upon ion irradiation with the dotted line representing the fluence that InSb becomes porous, based on SEM micrographs (BOLZAN et al., 2021a).

Figure 4.7 - (a) (b) k^2- weighted EXAFS spectra of InSb for In (left) and Sb (right) K-edges as a function of the photoelectron wavenumber and (c) (d) corresponding Fourier transforms as a function of the non-phase-corrected radial distance R from the absorber for InSb films irradiated with 14 MeV Au^{+6} ions at different fluences.

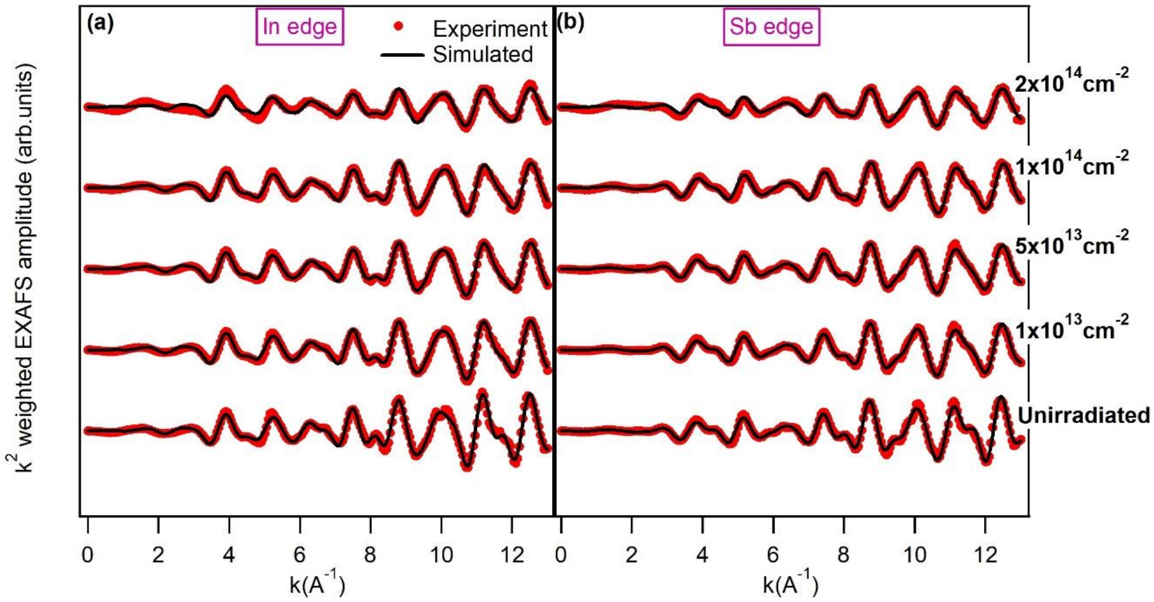

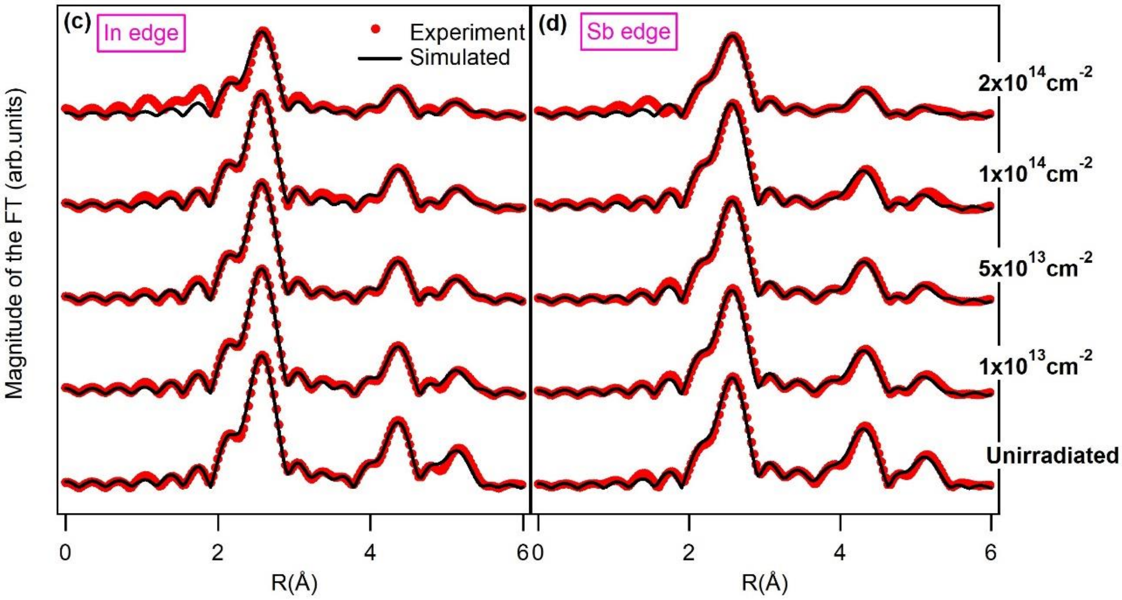

Figure 4.8-(a), (c) and (e) Interatomic distances of the first three NN shells and (b), (d) and (f) the respective coordination number. The Sb-In interatomic distances corresponding to the first and third shell present the same value of the respective In-Sb distances as observed in Table 4.4, therefore they

are not shown here. The dotted lines indicate the fluence for which InSb is rendered porous. The Y axis span was set to be the same for interatomic distance and coordination number, evidencing that the changes in 1st NN is the smallest.

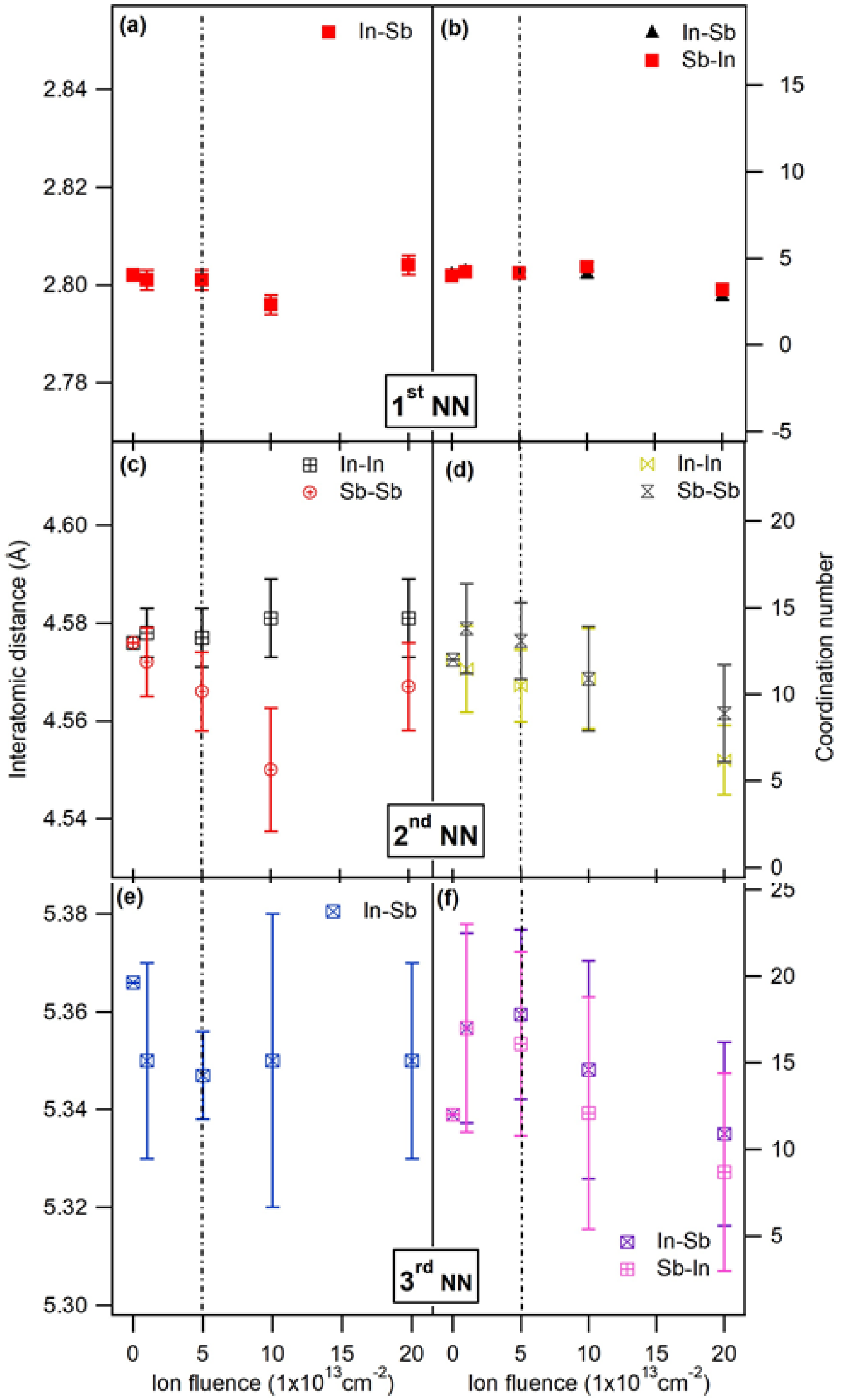

Table 4.4- Interatomic distances obtained from EXAFS measured at the In and Sb edges of InSb films irradiated with different fluences.

	Interatomic distance(Å)			
Ion Fluence	1stNN Sb	2ndNN In	2ndNN Sb	3rdNN Sb
NI	2.802 set	4.576 set	4.576 set	5.366 set
1e13	2.801±0.002	4.578±0.005	4.572±0.007	5.35±0.02
5e13	2.801±0.002	4.577±0.006	4.566±0.008	5.347±0.01
1e14	2.796±0.002	4.581±0.008	4.550±0.010	5.35±0.03
2e14	2.804±0.002	4.581±0.008	4.567±0.009	5.35±0.02

Table 4.5 - Debye-Waller factor obtained from EXAFS measured at the In and Sb edges of InSb films irradiated with different fluences.

	Debye-Waller factor (10^{-3}Å^2)			
Ion Fluence	1stNN Sb	2ndNN In	2ndNN Sb	3rdNN Sb
NI	1.3±0.1	4.2±0.3	3.1±0.3	4.1±0.4
1e13	1.8±0.3	6±1	5±1	9±2
5e13	1.9±0.2	6 ±1	5.8±0.9	10±2
1e14	2.1±0.3	7±2	5±1	9±3
2e14	1.7±0.4	6±2	6±2	10±3

According to the Stopping and Range of Ions in Matter (SRIM) (ZIEGLER; BIERSACK; ZIEGLER, 2008), 14 MeV Au ions have electronic energy loss (S_e) of 2.72 keV/nm and nuclear energy loss (S_n) of 1.56 keV/nm, with a variation of ~0.1 keV/nm and ~0.4 keV/nm in relation to depth, respectively. Therefore, for this energy (14 MeV), both regimes of energy loss in ion-matter interaction are of the same order of magnitude and none of them can be ignored in the process of damage formation. Nonetheless, as reported by Schnohr *et al.* (SCHNOHR et al., 2008), InP amorphized by ion irradiation in the two regimes separately did not show appreciable difference in the atomic structure, despite the fundamentally different energy transfer process, attributed to a common “melt and quench” process for amorphization. As a comparison, Wendler *et al.* (WENDLER; WESCH, 2006) observed, via Rutherford backscattering spectrometry in channelling configuration, that the damage production is more pronounced in InSb than InP upon Ar ion implantation at 15 K due to the fact that the latter presents a higher atomic force constant, for which damage formation in binary III-V compounds has a systematic dependence.

Figure 4.7 evidences that InSb films remain crystalline for irradiation fluences up to 2x10^{14}cm^{-2}. The reduced amplitudes of the first three NN peaks reflect, for 14 MeV Au^{+6} ions, that the ion irradiation induce damage to the crystal lattice. Moreover, there is no observation of homopolar bonding, which has been experimentally detected in other III-V compounds (RIDGWAY et al., 2003). For the first NN, it was observed that its respective structural parameters (Table 4.4 and Table 4.5) are, in general, unchanged, within uncertainty, within the ion fluence range investigated here, except the coordination number for samples irradiated with fluence of 2x10^{14}cm^{-2}, for which the coordination number decreases by ~ 30 % in comparison to the unirradiated one. The conservation of coordination number was also reported on nano-porous GaSb prepared by swift heavy-ion irradiation with 185 MeV Au^{+13} ions at similar fluences (NOTTHOFF et al., 2018). Moreover, the authors also reported no sign of homo-polar bonding in contrast to nano-porous GaSb prepared by low energy ion irradiation (KLUTH et al., 2011). For the second NN shell, the coordination number decreases by ~ 48 % and ~ 26 % at 2x10^{14}cm^{-2} in comparison to the unirradiated one, respectively, for In-In and Sb-Sb bond due to irradiation-induced disorder (RIDGWAY et al., 2003). This significant structural disorder is corroborated through increases of In-In and Sb-Sb DW factors, in this order, of $\sim$1.4 and $\sim$1.9 the respective crystalline values. As a parallel (BOLZAN et al., 2021a), crystalline InSb becomes porous at fluence of 5x10^{13} cm^{-2} upon irradiation with 14 MeV Au^{+6} ions, remaining simultaneously crystalline (with zincblende structure) and porous up to 3x10^{14} cm^{-2} , in agreement with EXAFS spectra shown in Figure 4.7. Therefore, it seems that the degree of porosity has an influence not only in the microscale, but in the atomic-scale as well. In the third shell, the ratio of the DW factor increases $\sim$2.4 times the respective crystalline value. However, the value of the third NN shell distance, on average, decreases from NI to 5x10^{13} cm^{-2}, remaining constant up to the highest fluence used in this work.

It is interesting to mention that the bond length conservation in InSb in the atomic-scale was also observed for GaSb and $In_xGa_{1-x}Sb$ samples irradiated with 8 MeV Au^{+3} ions with ion fluences ranging from 1 × 10^{13} cm^{-2} to 5 × 10^{14} cm^{-2} as shown Figure 4.9-(a) and (b). The k^3-weighted EXAFS oscillations at the In and Ga K-edges and the structural parameter for the first shell measured at In and Ga K edges, after ion irradiation with 8 MeV Au^{+3} ions for the highest fluence used here, are presented in appendix C. In this case, both EXAFS measurements and ion irradiation were performed at room temperature.

Figure 4.9 - Interatomic distances of the first NN shell of (a) InSb and GaSb and (b) In$_{1-x}$Ga$_x$Sb as a function of ion irradiation.

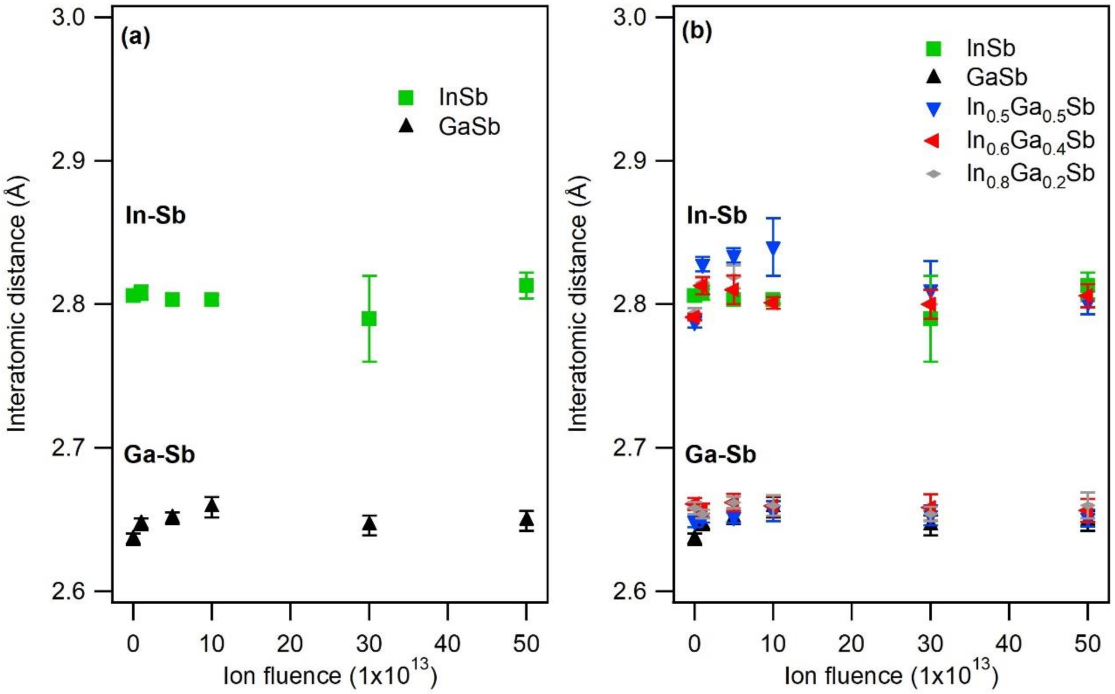

4.3.1 Relationship between the optical properties and nearest neighbor distance

As reported by Carles et al. (CARLES; LANDA; RENUCCI, 1985), the frequency of optical phonons is dominated by nearest-neighbor bond stretching force constants and has been shown to correctly predict local mode frequencies in III-V semiconductor alloys. Rucker H. (RUCKER; METHFESSEL, 1995) observed that optical frequency shift induced by the relaxation in alloys can be explained via three contributions. They are the mass disorder, Δw^{mass}, (here relative to the difference in the reduced mass between InSb and GaSb), microscopic strain, Δw^{micro}, (corresponding to how the ternary alloy accommodates the mismatch lattice parameter of their binary counterparts) and macroscopic strain, Δw^{macro}, (resulting of external stress). Hence, the total optical frequency shift is:

$$\Delta w = \Delta w^{\text{mass}} + \Delta w^{\text{micro}} + \Delta w^{\text{macro}} \tag{15}$$

In the case of InSb and GaSb, $\Delta w^{\text{mass}} = \Delta w^{\text{micro}} = 0$, and since Figure 4.8 and Figure 4.9 show a bond length conservation in the atomic-scale for the range of ion fluences used in this work, consequently, $\Delta w^{\text{macro}} \approx 0$. Then, there is no variation of optical frequency in InSb and GaSb after ion irradiation. Concerning the ternary alloy ($In_xGa_{1-x}Sb$), both Δw^{mass} and $\Delta w^{\text{micro}} \neq 0$, however, $\Delta w^{\text{macro}} \approx 0$ (see Figure 4.9), which means the optical frequency shift behavior is similar before and after ion irradiation in $In_xGa_{1-x}Sb$ for the range of ion fluences used in this work. The optical frequency shift, here predicted for unirradiated $In_xGa_{1-x}Sb$ alloys, was experimentally determined through Raman spectroscopy by Kumar et al. (KUMAR et al., 2016) and Feng et al. (FENG et al., 1991).

4.4 $In_xGa_{1-x}Sb$ NANOFOAMS MADE BY ION IRRADIATION

After showing how $In_xGa_{1-x}Sb$ behaves upon ion irradiation in the atomic-scale level, this chapter explores the effects of ion irradiation in nanoscale.

In the present section of the work, $In_xGa_{1-x}Sb$ films were irradiated with 16 MeV Au^{7+} ions and for such energy, both nuclear and electronic energy loss also have to be taken into account, as calculated using SRIM, as shown in Figure 4.10. Researchers have reported the different behaviors observed for these combined regimes (nuclear and electronic energy loss), showing this interaction may be competitive (TOULEMONDE et al., 2001), synergetic (TOULEMONDE et al., 2011) or cooperative (THOME et al., 2013) depending on the type of compound under ion irradiation. In spite of their intrinsically different energy loss mechanisms, both regimes induce foam-like structures with similar features to those reported for GaSb (KLUTH et al., 2014) and other III-V semiconductors (WESCH; WENDLER; SCHNOHR, 2012).

Figure 4.10- The electronic (S_e) and nuclear (S_n) energy loss as a function of depth for InSb and $In_{0.5}Ga_{0.5}Sb$ irradiated with 16 MeV Au^{+7} ions, calculated using SRIM (ZIEGLER; BIERSACK; ZIEGLER, 2008).

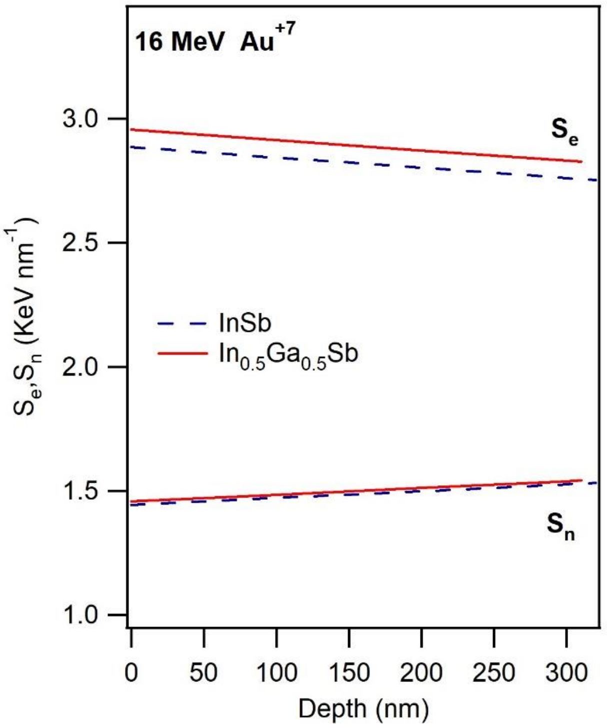

Figure 4.11 shows SEM micrographs of $In_xGa_{1-x}Sb$ films, in cross sectional configuration, as-deposited (not irradiated (NI)), and after irradiation with 16 MeV Au^{+7} ions to a total fluence of $1x10^{14}$ cm^{-2}. All images are on scale, hence, the dramatic transformations induced on the films by ion irradiation can be readily seen and the relative swelling for each stoichiometry can be directly appreciated.

Figure 4.11- Scanning electron microscopy micrographs of $In_xGa_{1-x}Sb$ films, as deposited and irradiated with 16 MeV Au^{+7} ions to a total fluence of $1x10^{14}$ cm^{-2}. NI – not irradiated.

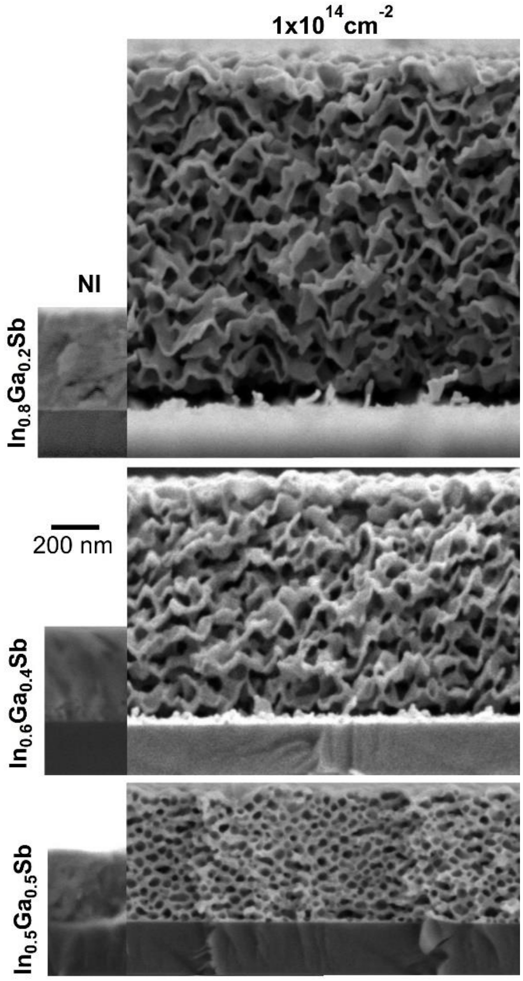

Ion irradiation induces the formation of pores in $In_xGa_{1-x}Sb$ films, and for sufficient irradiation fluences, porosity evolves towards a solid foam with nanometric dimensions, an effect also observed in other ternary and binary antimonide films irradiated with swift heavy ions (GIULIAN et al., 2020a)(BOLZAN et al., 2021c). InSb and GaSb also exhibit significant swelling upon irradiation, with the formation of pores in a similar manner (MANZO et al., 2019)(GIULIAN et al., 2017b). Upon sufficient irradiation fluence, the once spherical pores grow and coalesce forming large disform voids separated by solid walls with approximately the same thickness (~25 nm). This wall thickness minimum value seem to be independent of stoichiometry and it is the same for InSb and GaSb films irradiated under similar conditions (MANZO et al., 2019)(GIULIAN et al., 2017b).

The most pronounced swelling was observed for $In_{0.8}Ga_{0.2}Sb$ films as shown in Figure 4.12, when comparing films with different stoichiometries irradiated with the same fluence ($1x10^{14}$ cm^{-2}), while for films with lower In concentrations the swelling diminishes consistently: the higher the In fraction on the films, the more it swells upon irradiation (considering the ternaries only). Swelling was estimated by measuring the film thickness after irradiation and dividing by the initial thickness of the film (as-deposited), and those values are presented in Figure 4.12-(a) as a function of irradiation fluence, for all stoichiometries.

Figure 4.12– Swelling as a function of irradiation fluence for (a) $In_xGa_{1-x}Sb$ and (b) $In_xAl_{1-x}Sb$ films, for comparison(BOLZAN et al., 2021c), irradiated with 16 MeV and 14 MeV Au ions, respectively. Film thicknesses were measured directly from scanning electron microscopy micrographs.

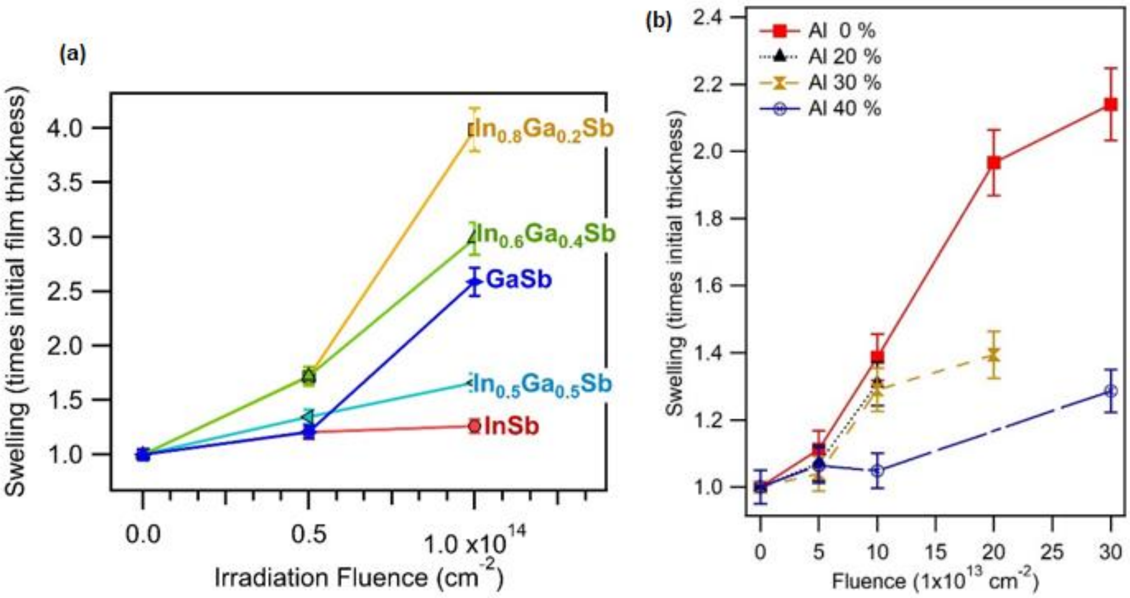

From Figure 4.12-(a), it is visible that swelling is more pronounced for the ternary films with the highest In concentration. Interestingly, InSb exhibits the lowest swelling of all samples, and from that we can infer that swelling is not governed solely by composition, otherwise one would expect to see the highest swelling for InSb films. Surely, other aspects like structure and pre-existing defects may also play an important role in ion irradiation-induced porosity. Such a behavior, however, is not observed in $In_xAl_{1-x}Sb$ films, which expand upon increasing the irradiation fluence (with 14 MeV Au^{6+}) with a more pronounced swelling at lower Al concentrations as shown in Figure 4.12-(b). Therefore, despite both isovalent ternary alloys having similar crystalline structure, only $In_xAl_{1-x}Sb$ follows the Vegard`s law in terms of swelling.

From Table 4.1 we can see that PIXE and RBS results are in good agreement. Prior to irradiation, all films exhibit a small amount of C and O (and N). After irradiation with $1x10^{14}$ cm^{-2}, the formation of nanofoams (see Figure 4.11) and consequently the large increase in effective surface area promotes the adsorption of C and O, which in some cases increases more than 5 times. For the heavier atoms (Ga, In and Sb), differences in areal density between films with different stoichiometries are mainly due to differences in film thickness. As shown previously (GIULIAN et al., 2020b), films with different stoichiometries have different initial thickness (prior to irradiation), mainly due to differences in the sputtering rate of each element, and for that reason, the areal density of each stoichiometry is quite different. The relative concentration of Ga, In and Sb, however, do not change significantly with irradiation, meaning there is no loss of material or sputtering induced by the ion irradiation process. The same (no loss of material) was also observed for $In_{1-x}Al_xSb$ films upon ion irradiation at similar fluences (BOLZAN et al., 2021c).

As shown in Figure 4.13 and Table 4.1, the ion irradiation-induced changes affect several aspects of the material, including the uniformity, the overall atomic density and also the morphology, as observed via SEM analysis (see Figure 4.11). As-deposited films exhibit sharp edges in the RBS spectra, indicative of well-defined boundaries between the film and the substrate (SiO_2/Si). The RBS of InSb and GaSb films (as-deposited) can be perfectly simulated by considering the films as single layers with homogenous composition, and the presence of oxygen atoms is also identified, representing 6% of the atomic fraction in GaSb film and 19% in InSb one. The RBS from $In_xGa_{1-x}Sb$, on the other hand, reveals that the films can be separated in two layers, at least, with slightly different compositions. The surface layer (L1) represents approximately 18-25% of each film thickness with a C contribution of 3-6 % of the total number of atoms and O, between 8-18%. Ga, In and Sb concentrations are not significantly different comparing layers 1 and 2 (for as-deposited films, within uncertainty), except for the $In_{0.6}Ga_{0.4}Sb$ sample, where Ga and In concentrations appear slightly depleted towards the surface. The high segregation tendency of In has been also observed in InGaSb crystals grown by the modified Czochralski method (KOZHEMYAKIN, 2000) and grown from the melt that contain appropriate ratio of Ga, In and Sb elements via emission electron probe microanalyzer (KUMAR et al., 2016).

Figure 4.13– Rutherford backscattering spectrometry of InSb and $In_{0.5}Ga_{0.5}Sb$ films, as deposited and irradiated with 16 MeV Au^{+7} ions to a total fluence of $2x10^{14}$ cm^{-2}. NI – not irradiated. The grey area indicates the approximate thickness of L1 (see Table *4.2*), where a depletion of Sb and In has been identified.

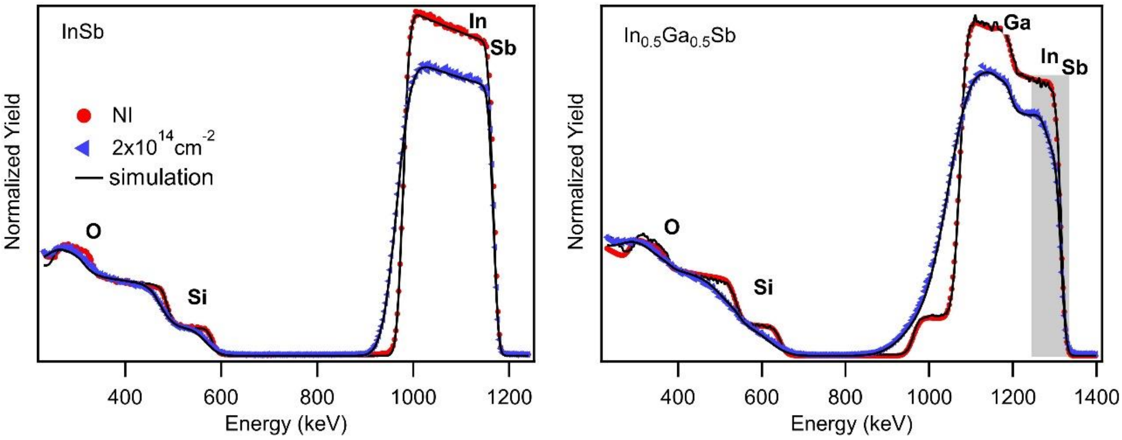

After ion irradiation, the sharp edges of the well defined as-deposited films give place to a smooth RBS curve upon irradiation, clearly apparent for the $In_{0.5}Ga_{0.5}Sb$ sample (Figure 4.13), and similar for all films with different stoichiometries (not shown). RBS results shown in Figure 4.13 (and Table 4.2) are consistent with those from SEM analysis shown in Figure 4.11. Pore diameter in $In_xGa_{1-x}Sb$ films increases consistently with irradiation fluence and, for the fluence range used in the present work, the increase is approximately linear (within uncertainty). The same trend can be seen for volume fraction and thickness (Table 4.2). Volume fraction of pores is related to the portion of empty space (not filled by atoms). Pore diameter and thickness are given in units of 10^{15} at/cm^2, which is the areal density and represents, roughly, one monolayer of material. A description of how the properties presented in Table 4.2 are obtained via SIMNRA has been reported in detail in literature (MAYER et al., 2012)(MAYER, 2017). $In_{0.8}Ga_{0.2}Sb$ films exhibit the largest pore diameter, followed by the other two ternaries (see Figure 4.14). InSb and GaSb present the smallest pore diameters, once again implying that porosity on $In_xGa_{1-x}Sb$ films is not solely dependent on stoichiometry. In the specific case of InSb and GaSb upon irradiation with 60 keV Sn^+ and fluence of $0.25x10^{18}$ m^{-2}, Nitta *et al.* (NITTA et al., 2010) observed that the void size in InSb is larger than that in GaSb, as opposed to the observed in this work.

Figure 4.14– Pore diameter (from RBS analysis) as a function of (a) irradiation fluence and (b) Ga concentration for $In_xGa_{1-x}Sb$ films irradiated with 16 MeV Au^{+7} ions.

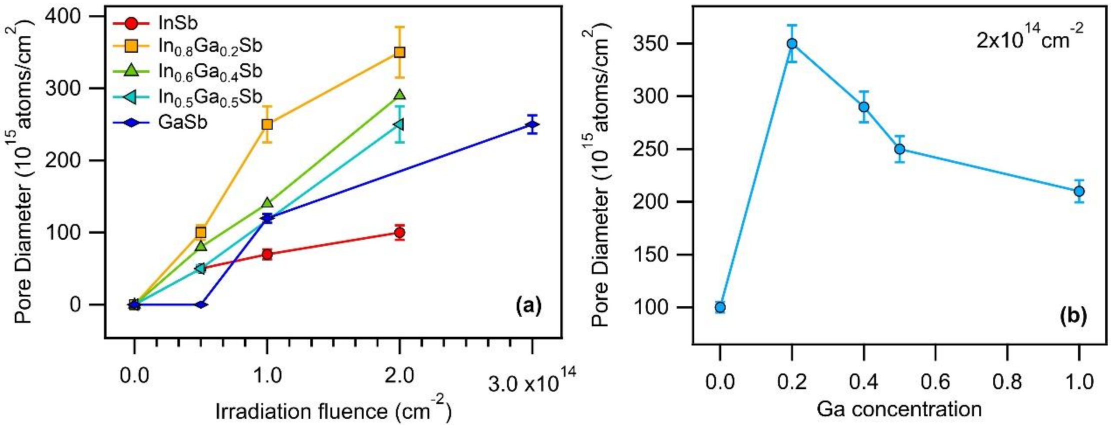

Table 4.1 - Areal density measured by RBS and PIXE techniques for $In_xGa_{1-x}Sb$ films before and after irradiation with 16 MeV Au^{+7} ions. NI – not irradiated. All values are given in units of 10^{15} atoms/cm^2 and have an uncertainty ~ 10%.

		C		O		Ga		In		Sb	
		PIXE	RBS	PIXE	RBS	PIXE	RBS	PIXE	RBS	PIXE	RBS
InSb	NI		59		83			383	456	354	421
	$1x10^{14}$		66		73			369	374	337	366
	$2x10^{14}$		232		235			366	366	344	368
$In_{0.8}Ga_{0.2}Sb$	NI		17		270	120	157	446	519	523	610
	$1x10^{14}$		311		311	123	191	396	396	529	529
$In_{0.6}Ga_{0.4}Sb$	NI		41		61	157	174	253	245	398	405
	$1x10^{14}$		196		251	167	173	254	248	419	401
$In_{0.5}Ga_{0.5}Sb$	NI		23		100	223	229	229	231	407	473
	$1x10^{14}$					222		238		443	
GaSb	NI				42	264	335	-	-	290	335
	$1x10^{14}$		92		237	257	235	-	-	381	234

Table 4.2 - Relative concentration of $In_xGa_{1-x}Sb$ films irradiated with different fluences. NI – not irradiated. All values have an uncertainty of approximately 10%. L1 (L2) represents the first (second) layer of the film, from the surface.

	Fluence (at/cm^2)	Thickness (10^{15} at/cm^2)		Vol. Frac. Pores (%.)		Pore Diam. (10^{15} at/cm^2)		Elemental concentration (at. %)									
								C		O		Ga		In		Sb	
		L1	L2	L1	L2	L1	L2	L1	L2	L1	L2	L1	L2	L1	L2	L1	L2
InSb	NI	-	1080	-	-	-	-	-	-	-	19	-	-	-	41	-	40
	5x10^{13}	-	1090	-	20	-	50	-	-	-	19	-	-	-	41	-	40
	1x10^{14}	150	940	20	30	50	70	10	6	16	15	-	-	34	40	40	39
	2x10^{14}	150	1290	50	60	80	100	25	24	20	19	-	-	26	28	29	29
$In_{0.8}Ga_{0.2}Sb$	NI	321	1293	-	-	-	-	5	0	16	21	10	11	25	27	44	42
	5x10^{13}	600	1223	20	50	80	100	5	10	12	22	14	9	31	27	38	32
	1x10^{14}	374	1750	50	60	200	250	21	14	23	22	10	12	20	18	26	34
	2x10^{14}	390	1749	55	85	250	350	28	15	28	21	5	11	14	21	25	32
$In_{0.6}Ga_{0.4}Sb$	NI	200	960	-	-	-	-	6	0	18	14	13	18	21	26	42	42
	5x10^{13}	300	920	20	30	40	80	11	0	15	14	13	19	19	27	42	41
	1x10^{14}	300	1330	40	60	100	140	10	17	30	21	14	13	15	19	31	30
	2x10^{14}	320	1343	60	75	100	290	34	16	27	19	7	15	5	19	27	31
$In_{0.5}Ga_{0.5}Sb$	NI	200	1133	-	-	-	-	3	0	8	18	24	20	22	20	44	42
	5x10^{13}	200	1203	30	45	50	50	7	6	17	15	18	19	16	20	42	40
	2x10^{14}	340	1483	60	65	100	250	24	18	29	19	12	16	10	15	25	32
GaSb	NI	-	712	-	-	-	-	-	-	-	6	-	47	-	-	-	47
	1x10^{13}	-	766	-	-	-	-	-	-	-	16	-	41	-	-	-	42
	1x10^{14}	338	860	60	60	100	120	25	23	23	22	26	28	-	-	26	27
	3x10^{14}	358	1025	70	70	200	250	34	21	28	30	18	25	-	-	20	25

In previous work, for $In_xAl_{1-x}Sb$ films irradiated with 14 MeV Au^{6+} at similar fluences, a very different trend was observed. InSb exhibited the largest pore diameter, followed by the ternary with the smallest relative Al concentration, and porosity was not observed in AlSb. In addition, a non-uniform pore size distribution was shown, with larger voids forming far from the sample surface. This phenomenon was attributed to the enhanced diffusion of voids towards the surface of the Al-containing samples due to surface sink effects and/or the presence of a Al_2O_3 concentration gradient along the film depth (BOLZAN et al., 2021c). Alkhaldi *et al.*(ALKHALDI et al., 2017) also reported a stoichiometry-dependent porosity by ion implantation in $GaAs_{1-x}Sb_x$ (irradiated with 140 keV As^- and ion fluences ranging from $1x10^{13}$ to $2x10^{17}$ cm^{-2}) with void formation and sputtering both playing a significant role. For x=0.25, porosity was largely suppressed, whereas for x=0.5 and for GaAs, no pores were formed. Comparing $In_xGa_{1-x}Sb$ with $In_xAl_{1-x}Sb$ and $GaAs_{1-x}Sb_x$ alloys upon ion irradiation, a different behavior is verified. $In_xGa_{1-x}Sb$ becomes porous throughout all In/Ga concentration ratio, while the other two ternary alloys do not respond the same way. For $In_xGa_{1-x}Sb$ alloys, both binary parent compounds (GaSb and InSb) are rendered porous upon sufficient ion irradiation, whereas for $In_xAl_{1-x}Sb$ and $GaAs_{1-x}Sb_x$, AlSb and GaAs do not show evidences of pores formation.

Comparing the effects of ion irradiation in nanoscale and atomic-scale, it was observed, respectively, a pronounced continuous-to-porous transformation and a bond length conservation in $In_xGa_{1-x}Sb$ films.

4.4.1 Ion-matter interactions and mechanisms of void formation

Energetic ions traveling through matter lose energy in two distinct ways: transferring energy to the nuclei (via elastic collision) or electrons (through inelastic collision) of the material. The latter results in excitation or ionization of the target atoms whist the former produces phonons or displaced target atoms, among other defects. Which of the two effects are dominant depends on the specific range of energy and mass of the accelerated ion, as well as the mass and atomic number of the medium (H.; RUGE, 1987).

The mechanisms involved in ion irradiation-induced porosity are still a matter for discussion, although some researchers suggest this process, in the antimonides, can be understood using a classical model of nuclear collision displacement (ballistic collisions (KLUTH; LLEWELLYN; RIDGWAY, 2006)) considering the nuclear energy loss regime. In this model, the nuclear energy loss of incident ions inside the target matrix results in the formation of defects, i.e., vacancies and interstitials by displacing the constituent atoms from crystallographic sites, if sufficient energy is transferred to the matrix. Due to the inefficient recombination of interstitials with vacancies, an excess of vacancies is left and cluster to form voids, which coalesce leading to the gradual formation of a porous layer (NITTA; TANIWAKI, 2003). For swift heavy ion irradiation (electronic energy loss regime), void formation cannot be explained based on the classical model previously described, but should include a cooperative mechanism: The thermal spike model. In this model, when energetic heavy ions pass through a solid, the ions lose energy by exciting electrons and these excited electrons lose energy to the atoms via electron-phonon coupling increasing the energy of a small volume around the ion path, inducing a significant increase of the lattice temperature. If this temperature overcomes the melting or boiling point of the material, molten or boiled zones are created, which rapidly quench, forming regions with different density and sometimes different structures (DESTEFANIS; GAILLIARD, 1980; SCHIWIETZ et al., 2004).

4.5 $In_xGa_{1-x}Sb$ NANOFOAMS : THERMAL STABILITY AND THERMOELECTRIC PROPERTIES

In the previous sections, it was shown that $In_xGa_{1-x}Sb$ exhibits a stoichiometry-dependent porosity, with structural and morphological changes even more pronounced than those observed for $In_xAl_{1-x}Sb$. The great surface area offered by $In_xGa_{1-x}Sb$ nanofoams, in addition to the flexibility in terms of tunning structural and electrical properties of this ternary antimonide, makes it very well suited for applications, in particular, in gas detectors and thermoelectric materials. However, this kind of devices often operate at high temperatures, and even if operating temperatures are not elevated by external heat sources, the voltage difference applied to the material generates current, consequently inducing an increase in temperature (at least locally). Taking this factor into account, the following section discusses about the thermal stability of $In_xGa_{1-x}Sb$ nanofoams. It should be noted that there is virtually no information in the literature about the stability of ion irradiation-induced nanofoams subjected to high temperatures, in particular regarding $In_xGa_{1-x}Sb$.

Figure 4.15 shows RBS spectra for $In_{0.8}Ga_{0.2}Sb$ samples, as-deposited and after irradiation with 16 MeV Au^{+7} ions to a total fluence of $2x10^{14}$ cm^{-2}. Spectra on the left panel correspond to the samples as-prepared, and the ones on the right panel are from the same samples after annealing in vacuum ($1x10^{-3}$ Pa), for 1 h, at 200 ºC. The RBS analysis from $In_xGa_{1-x}Sb$ samples with different In/Ga concentration ratio (x value ranging from 0-1) were analysed in a similar way and the complete results are listed in Table 4.3.

Figure 4.15-– Rutherford backscattering spectrometry of $In_{0.8}Ga_{0.2}Sb$ films, before and after irradiation with 16 MeV Au^{+7} ions to a total fluence of $2x10^{14}$ cm^{-2}. The spectra on the right correspond to the same samples shown on the left, after annealing in vacuum for 1 h at 200 ºC.

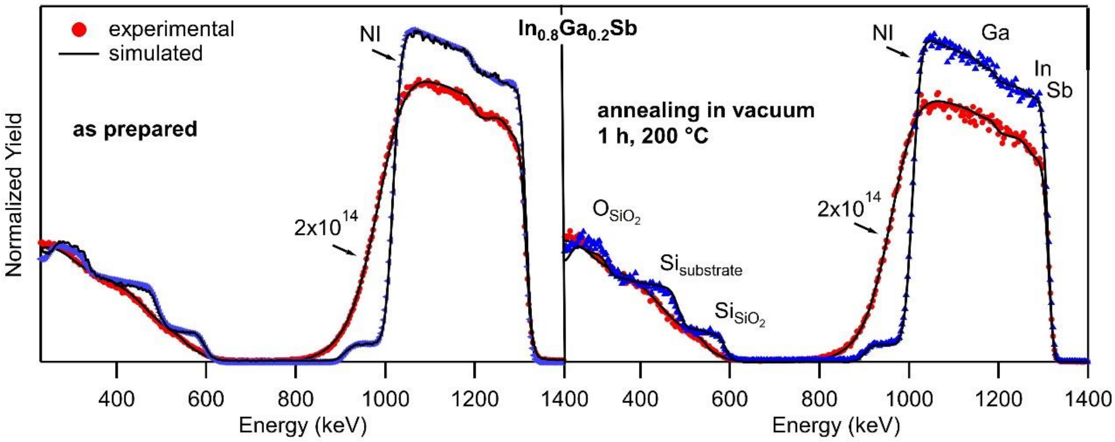

Table 4.3 - Relative concentration of $In_xGa_{1-x}Sb$ films irradiated with 16 MeV Au^{+7} ions to a total fluence of $1x10^{14}$ cm^{-2}, before and after annealing in vacuum, for one hour, at 200 ºC. _a – annealed. NI – not irradiated. All values have an uncertainty of approximately 10%. L1 (L2) represents the first (second) layer of the film, from the surface.

	Fluence (at/cm^2)	**Thickness (10^{15} at/cm^2)**		**Vol. Frac. Pores (%.)**		**Pore Diam. (10^{15} at/cm^2)**		**Elemental concentration (at. %)**									
								C		**O**		**Ga**		**In**		**Sb**	
		L1	L2	L1	L2	L1	L2	L1	L2	L1	L2	L1	L2	L1	L2	L1	L2
InSb	NI	-	1080	-	-	-	-	-	-	-	19	-	-	-	41	-	40
	NI_a	**-**	**1090**	**-**	**-**	**-**	**-**	**-**	**-**	**-**	**19**	**-**	**-**	**-**	**41**	**-**	**40**
	$1x10^{14}$	150	940	20	30	50	70	10	6	16	15	-	-	34	40	40	39
	$1x10^{14}$_a	**-**	**1260**	**-**	**25**	**-**	**100**	**-**	**18**	**-**	**16**	**-**	**-**	**-**	**33**	**-**	**33**
$In_{0.8}Ga_{0.2}Sb$	NI	-	1617	-	-	-	-	-	-	-	21	-	10	-	24	-	45
	NI_a	**246**	**1440**	**-**	**-**	**-**	**-**	**8**	**0**	**23**	**22**	**6**	**10**	**27**	**30**	**36**	**38**
	$1x10^{14}$	374	1751	50	60	200	250	21	14	23	22	10	12	20	18	26	34
	$1x10^{14}$_a	**405**	**2101**	**50**	**60**	**200**	**230**	**30**	**24**	**29**	**25**	**5**	**8**	**17**	**20**	**19**	**23**
$In_{0.6}Ga_{0.4}Sb$	NI	200	960	-	-	-	-	6	-	18	14	13	18	22	26	42	42
	NI_a	**174**	**968**	**-**	**-**	**-**	**-**	**7**	**-**	**15**	**14**	**13**	**17**	**20**	**26**	**45**	**43**
	$1x10^{14}$	300	1331	40	60	100	140	10	17	30	21	14	13	15	19	31	30
	$1x10^{14}$_a	**296**	**1310**	**40**	**60**	**100**	**140**	**12**	**16**	**27**	**21**	**14**	**14**	**15**	**19**	**31**	**30**
	Ni	200	1134	-	-	-	-	3	-	8	18	24	20	22	20	44	42

	NI_a	**223**	**1113**	**-**	**-**	**-**	**-**	**8**	**-**	**11**	**19**	**22**	**21**	**20**	**20**	**40**	**40**
	$1x10^{14}$_a	**309**	**1694**	**60**	**60**	**100**	**140**	**29**	**18**	**27**	**26**	**8**	**14**	**12**	**13**	**24**	**28**
GaSb	NI	-	712	-	-	-	-	-	-	-	6	-	47	-	-	-	47
	NI_a	**-**	**760**	**-**	**-**	**-**	**-**	**-**	**-**	**-**	**12**	**-**	**44**	**-**	**-**	**-**	**44**
	$1x10^{14}$	338	861	60	60	100	120	25	23	23	22	26	28	-	-	26	28
	$1x10^{14}$_a	**305**	**980**	**50**	**50**	**100**	**100**	**25**	**24**	**28**	**25**	**22**	**26**	**-**	**-**	**25**	**25**

To obtain a good fit to the RBS data, some samples were divided in two layers (in the SIMNRA simulations), named L1 and L2, L1 being closer to the surface. For samples with similar L1 and L2 values, only one layer was considered (L2).

InSb NI film shows a slight difference before and after annealing. GaSb NI shows a slight increase in O concentration upon annealing, which contributes to a slight increase in film thickness. For the NI ternaries, the amount of C in L1 slightly increases with annealing and the relative amounts of In, Ga and Sb change, but all the other parameters remain the same (comparing samples before and after annealing). For the ternary nanofoams (samples irradiated with $1x10^{14}$ cm^{-2}), $In_{0.8}Ga_{0.2}Sb$ exhibits the most prominent swelling (SEM images shown in Figure 4.11) and consequently, the highest porosity levels, almost twice as much as $In_{0.6}Ga_{0.4}Sb$ and $In_{0.5}Ga_{0.5}Sb$. With the greater increase in effective surface area promoted by the larger pore sizes, it is expected that a greater amount of lighter atoms can be incorporated into the foams. When $In_{0.8}Ga_{0.2}Sb$ foams are subjected to annealing, the adsorption of C and O atoms induces an overall increase in film thickness, but with no significant changes in the relative amount of Ga, In and Sb, which explains the similarity between RBS spectra (before and after annealing) shown in Figure 4.15. The similarity between RBS results (see Table 4.3) from samples before and after annealing, especially regarding porosity, confirms the stability of $In_xGa_{1-x}Sb$ nanofoams subjected to elevated temperatures. The stability of $In_xGa_{1-x}Sb$ nanofoams allow this compound to be used as a gas sensor not only at room temperature but also at elevated temperatures.

4.6 THERMOELECTRIC PROPERTIES OF $In_xGa_{1-x}Sb$ NANOFOAMS

An important aspect to be considered for thermoelectric (TE) materials is the potential to convert heat into electricity, usually measured by the dimensionless figure of merit ZT as explained in details in section 3.7.

Figure 4.16 shows the electrical conductivity, Seebeck coefficient, thermal conductivity and the values of ZT for $In_xGa_{1-x}Sb$ samples prior to irradiation (NI), and the same parameters are displayed in Figure 4.19 for $In_{0.8}Ga_{0.2}Sb$ samples irradiated with different fluences.

Figure 4.16– (a) electrical conductivity, (b) Seebeck coefficient, (c) thermal conductivity and the values of (d) ZT for $In_xGa_{1-x}Sb$ films prior to irradiation (NI). The uncertainties on all points are smaller than the symbols.

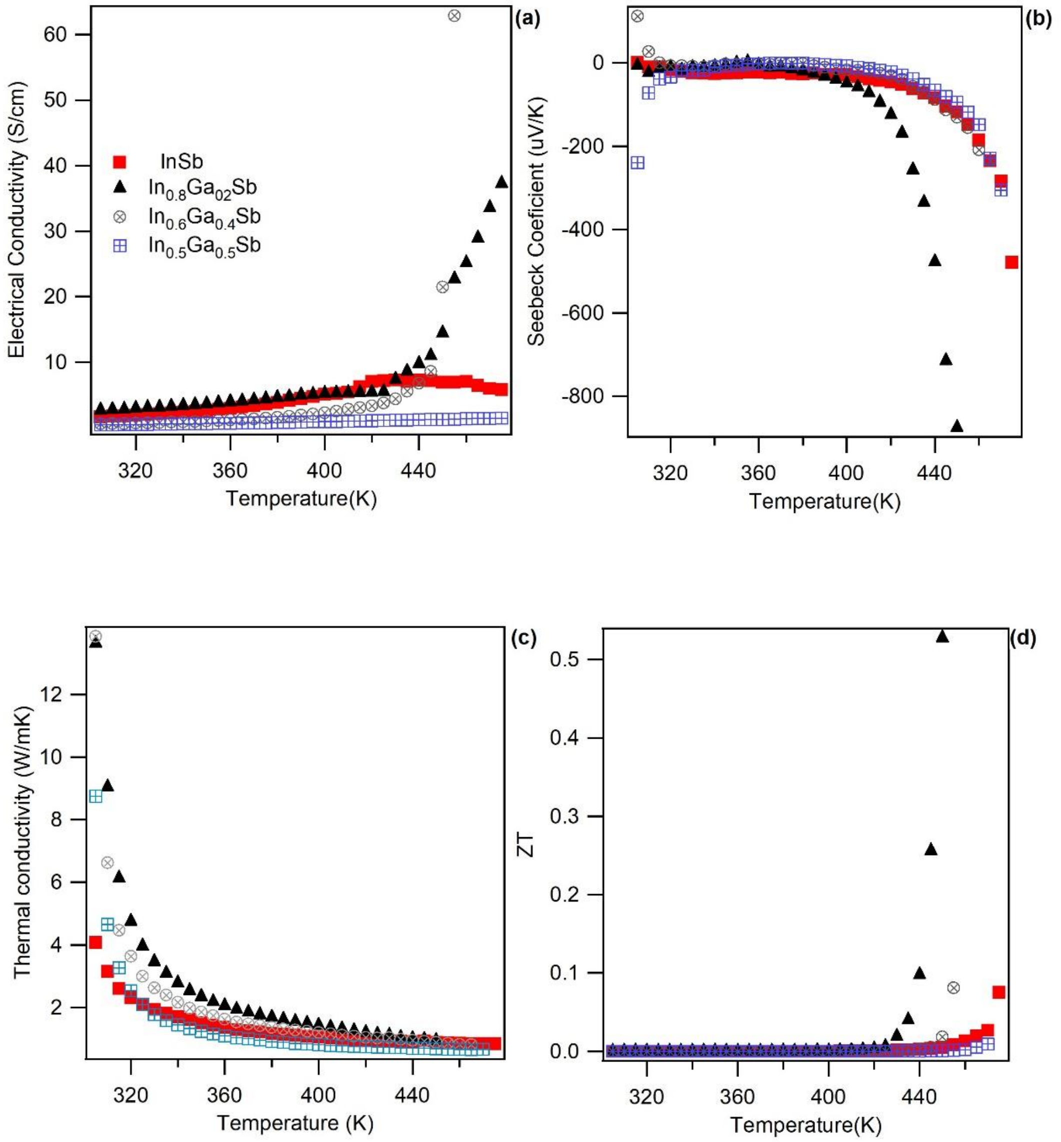

From Figure 4.16-(a), it is observed that the electrical conductivity of $In_xGa_{1-x}Sb$ was increased with the temperature which is the typical behavior of undoped semiconductors. When compared with $In_xAl_{1-x}Sb$, for the same range of temperatures (298-373K), a different behavior is verified (Figure 4.17). Whereas the electrical conductivity of $In_xGa_{1-x}Sb$ does not change drastically for a specific temperature, for $In_xAl_{1-x}Sb$ “a knee” stoichiometry-dependent is observed. Such disparity between both electrical behaviors can be explained via bandgap energy (E_g). Figure 4.18 shows that $E_{g\text{-}In1\text{–}xAlxSb} > E_{g\text{-}In1\text{–}xGaxSb}$ for all In concentrations which means it is easier to promote electrons from the valence band to the conduction band in $In_xGa_{1-x}Sb$ in comparison to $In_xAl_{1-x}Sb$, explaining the results shown in Figure 4.17. The same behavior observed for $In_xAl_{1-x}Sb$ compounds was also reported in literature for many other semiconductors (KINGERY, 1960). It should be noted that it was observed no clear relationship between In-Ga relative atomic concentration and electrical conductivity in $In_xGa_{1-x}Sb$ films deposited by magnetron sputtering, although its effect is evident in Figure 4.17-(a). The same tendency was reported by Kumar et.al (KUMAR et al., 2016).

Figure 4.17 - Electrical conductivity comparison between $In_xGa_{1-x}Sb$ and $In_xAl_{1-x}Sb$ compounds.

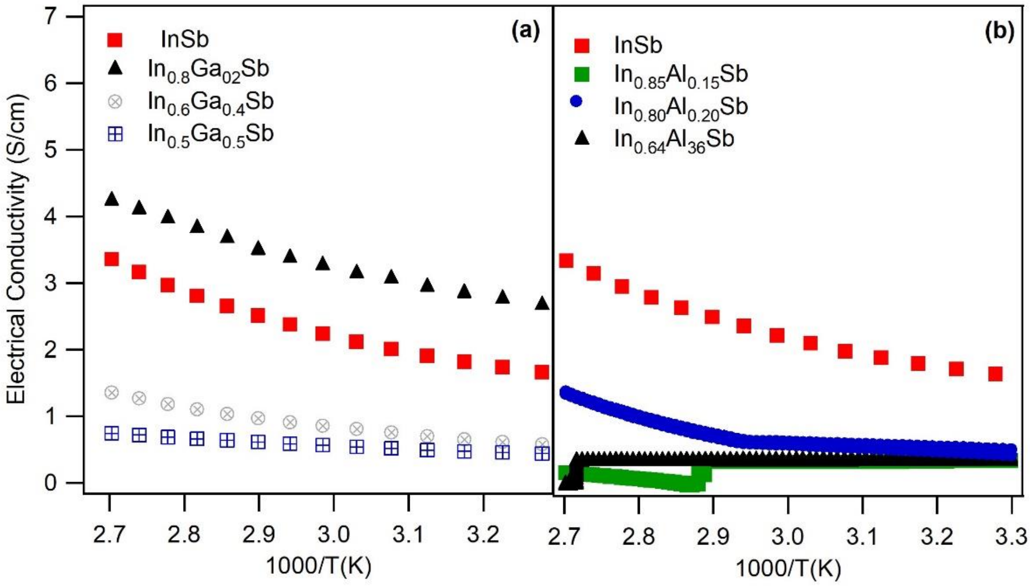

The variation in Seebeck coefficient (S) of $In_xGa_{1-x}Sb$ with temperature is shown in Figure 4.16-(b). All $In_xGa_{1-x}Sb$ samples have negative Seebeck coefficient that show n-type conductivity in agreement with previous Hall measumments (GIULIAN et al., 2020b). The highest Seebeck coefficient values were observed for $In_{0.8}Ga_{0.2}Sb$ films which reached the maximum value of 875 μV/K at 450 K. The Seebeck coefficient value was higher than that of $In_xGa_{1-x}Sb$ (280 μV/K and 335 μV/K) prepared, respectively, by nanoinclusion of gallium (ZHANG et al., 2011) and melt solidification process (KUMAR et al., 2016).

Figure 4.18– Bandgap comparison between $In_xGa_{1-x}Sb$ and $In_xAl_{1-x}Sb$ compounds as a function of In concentration.

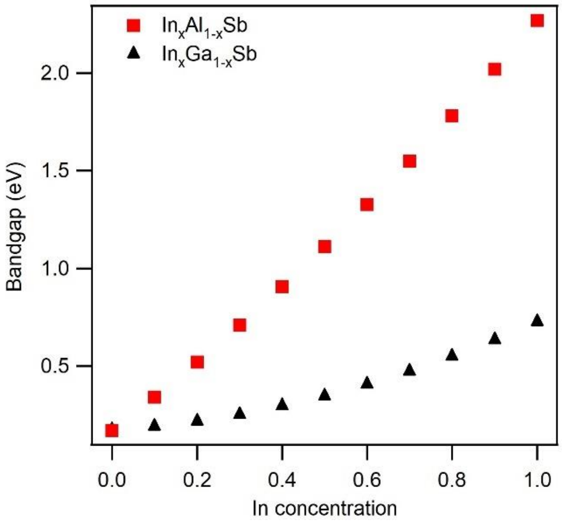

Reference: data from (ADACHI, 2009)

The temperature dependences of thermal conductivity are shown in Figure 4.16-(c). For all the samples, the total thermal conductivity decreases with temperature. The lattice thermal conductivity (κ_L) was calculated by $\kappa = \kappa_L + L_0T\sigma$, where L_0 is the Lorentz number $L_0=2\times10^{-8}$ V^2K^{-2} is used for estimation, T is the temperature and $k_e = L_0T\sigma$. Since $\kappa \approx \kappa_L$, $In_{1-x}Ga_xSb$ thin films presents high electrical resistivities, so heat conduction is then, in effect, due solely to lattice vibrations in the range of temperatures used in this work. At 305 K, K_L is clearly dependent of the ratio In/Ga concentration, however, it is opposite to the Nordheim rule or equivalently to Abeles's model(ADACHI, 2009). In such models, the lattice thermal conductivity reduction (which is well below that of their individual components) is mainly due to scattering of the phonons from the mass fluctuation and strain field fluctuation between Ga and In. These models, nevertheless, do not take into account the scattering of phonons on the crystal boundaries that has been known since the work of Casimir (BÖER; POHL, 2018), possibly explaining the differences between the results presented here and the ones predicted in literature. Moreover, κ_L is practically independent of stoichiometry at 450 K (not shown). Du et al. (DU et al., 2018) observed this same behavior only at 700 K in $In_xGa_{1-x}Sb$ samples prepared by a two-step B_2O_3 flux method combined with the spark plasma sintering (SPS) technique.

Regarding the figure of merit ZT, equation (11) was used to obtain it, where $In_{0.8}Ga_{0.2}Sb$ exhibited the highest ZT values (0.53 at 450 K). Kumar et al. (KUMAR et al., 2019) recorded the highest ZT of 0.62 at 573 K of any reported values of III-V binary or ternary semiconductors. The results obtained here are very promising, especially considering the relatively low measurement temperature. It is worth mentioning that the relationship between thermoelectric figure of merit and energy conversion efficiency (ε) is not straightforward as reported by Kim et al.(KIM et al., 2015). The ε values vary greatly depending on how the average ZT values are used, raising questions about the applicability of ZT in the case of a large temperature difference between the hot and cold sides due to the neglect of the temperature dependences of the material properties that affect ZT. To avoid the complex numerical simulation that gives accurate efficiency, usually the ZT parameter is published in scientific articles instead of energy conversion efficiency.

Since $In_{0.8}Ga_{0.2}Sb$ films exhibited the highest ZT values, it was decided to compare the TE properties of these films irradiated with different fluences, and consequently showing different levels of porosity. From Figure 4.19-(a) we see that the electrical conductivity is significantly reduced after irradiation, and that affects the ZT parameter. Samples irradiated with $5x10^{13}$ cm^{-2} show a ZT value of 0.23, while for samples irradiated with $1x10^{14}$ cm^{-2} the ZT value is 0.12.

Several works have been reported on the thermoelectric properties of $In_xGa_{1-x}Sb$ compounds, and the ZT value in the range 0.2-0.3 are the most recurrent for measurement temperatures around 450 K, as shown in Table 4.4. In comparison to other works reported in the literature (DU; YAN; ZHU, 2018) (KUMAR et al., 2016) (DU et al., 2018) (ZHOU et al., 2010) (KUMAR et al., 2019) (JIANG et al., 2013) we see that the $In_{0.8}Ga_{0.2}Sb$ films deposited by magnetron sputtering (this work) exhibit ZT value significantly higher than all the other works published to date for the measurement temperature of 450 K. Some of these works report ZT values of about 5.2 and even higher, but for much higher measurement temperatures (between 600 and 700 K). The same material, after irradiation with 16 MeV Au^{+7} ions, was transformed into nanofoams (see Figure 4.11), and the ZT values obtained for samples irradiated with a total fluence of $5x10^{13}$ cm^{-2} ($1x10^{14}$ cm^{-2}) substantially decreased, attaining a value of 0.23 (0.12) (see Figure 4.19). Therefore, although $In_xGa_{1-x}Sb$ nanofoams is a potential candidate to be applied in gas sensor from room to elevated temperatures, the same is not observed for thermoelectric material.

Table 4.4 - ZT values for $In_xGa_{1-x}Sb$ compound measured at 450 K from different literature sources.

Compound	ZT	Reference
$In_{0.8+y}Ga_{0.2}Sb$	0.3	(DU; YAN; ZHU, 2018)
$In_{0.8}Ga_{0.2}Sb$	0.1	(KUMAR et al., 2016)
$In_{0.8}Ga_{0.2}Sb$	0.2	(DU et al., 2018)
InSb nanowires	~0.01	(ZHOU et al., 2010)
$In_{0.95}Ga_{0.05}Sb$	0.35	(KUMAR et al., 2019)
InSb	0.2	(JIANG et al., 2013)
InSb	0.3	(KUMAR et al., 2016)
$In_{0.8}Ga_{0.2}Sb$	0.53	this work
$In_{0.8}Ga_{0.2}Sb$ $5x10^{13}$ cm^{-2}	0.23	this work
$In_{0.8}Ga_{0.2}Sb$ $1x10^{14}$ cm^{-2}	0.12	this work

Figure 4.19– (a) electrical conductivity, (b) Seebeck coefficient, (c) thermal conductivity and the values of (d) ZT for $In_{0.8}Ga_{0.2}Sb$ films prior (NI) and after irradiation. The uncertainties on all points are smaller than the symbols.

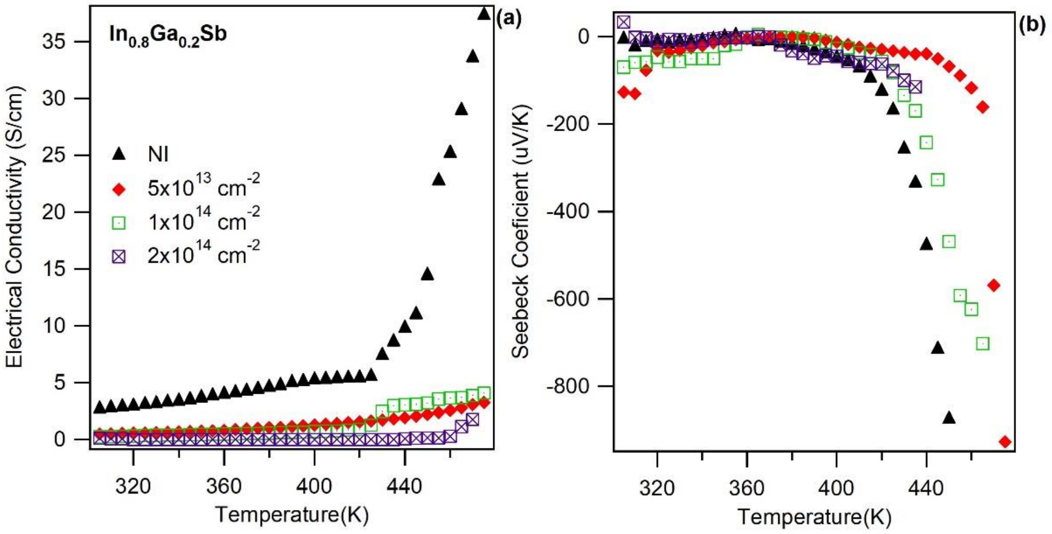

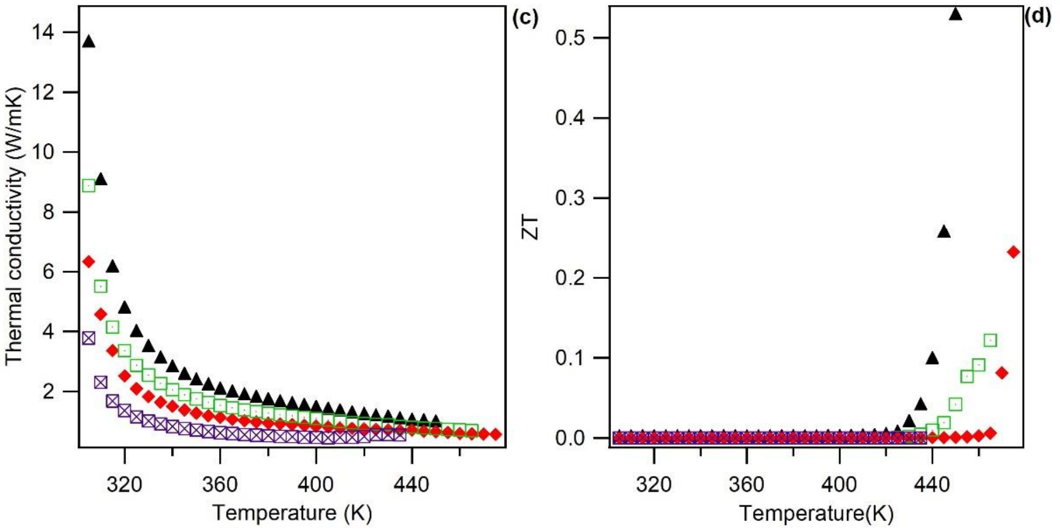

4.6.1 Understanding the thermoelectric properties of III−V ternary $In_xGa_{1-x}Sb$ alloys

The performance of TE generators depends on the thermoelectric figure of merit (ZT) of semiconductor materials used for fabrication. From equation (11), ZT is directly proportional to the thermoelectric power factor and an inversely proportional to the thermal conductivity. Thus, enhancement of the power factor and a reduction in thermal conductivity are ideal to obtain a high ZT in TE materials. The experimental techniques mostly focus to reduce the thermal conductivity in a multicomponent system by controlling their lattice thermal conductivity. That can be attained through various phonon scattering processes given that phonons contribute more than 80% of the total thermal conductivity in many semiconductor materials (LI et al., 2016)(KUMAR et al., 2016)(WU et al., 2015). However, increasing ZT is difficult due to the interdependency of all the related properties. As the phonons can be considered virtual atomic positions arising from thermal agitation in a crystal lattice, controlling those atomic positions could affect electron transport as well. To overpass this problem, the lattice sites should behave as a “crystal” for electrons and “glass/amorphous” for phonons, i.e., the corresponding material should be a phonon glass electron crystal, in which electrical properties are separated from thermal properties (SALES et al., 1997). Such behavior, although observed in some materials experimentally (SALES et al., 1997)(KHALIQ et al., 2014), is quite challenging to achieve in many other materials.

A way to overcome this issue is through understanding and engineering the defects in materials, because various imperfections/defects can affect the electron and phonon transports, and their effect depends on the nature of defects in crystalline materials (ZHOU et al., 2018)(ZHANG et al., 2018).

To comprehend and improve the TE properties of materials, the crystalline imperfections in bulk can be separated as (i) charged and (ii) structural defects. Point defects can be classified as "charged defects," and other lattice imperfections such as grain boundaries, lattice strain, slip planes, twinning, etc. can be considered "structural defects", in crystalline materials. This approach is schematically shown in Figure 4.20.

Point defects highly affect charge carrier transport, though they have an important role in reducing the phonon wavelengths, because they are charged and serve as compensation centers for the electrons and holes, which impact the electrical properties of a material. However, the lattice strains behave as scattering centers to phonon transport, and they do not affect much the carrier transport. Thus, the charged (structural) defects dominate the electron (phonon) transport properties in a crystal lattice.

Figure 4.20- A schematic of the effects of charged and structural defects on the electron and phonon transport properties in crystalline materials.

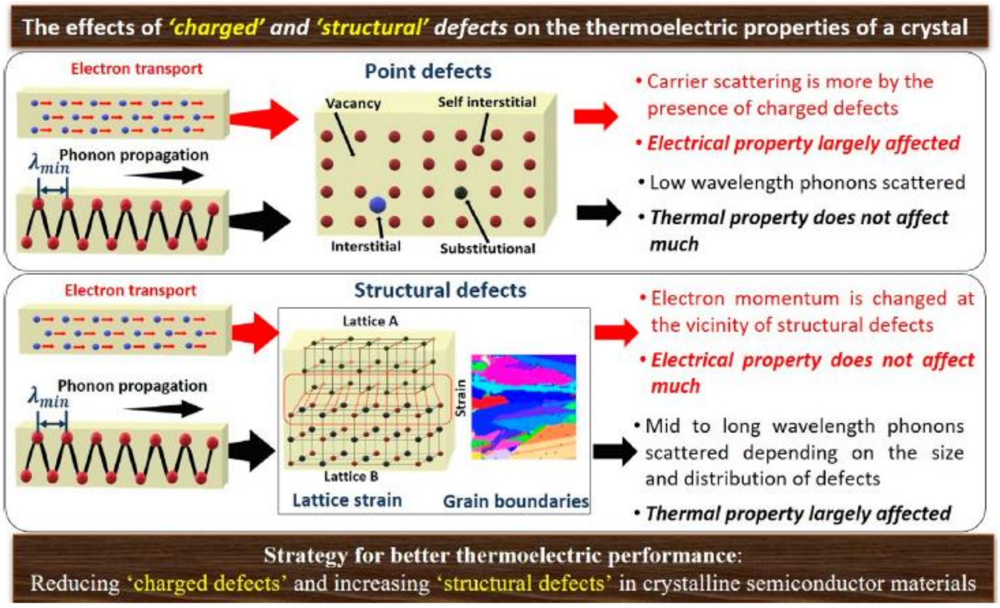

Reference: (KUMAR et al., 2019)

The major scattering processes occurring in the binary III-V semiconductors around 300 K are polar-optical and acoustic phonon scattering, piezoelectric scattering, and ionized-impurity scattering (SAFA KASAP; PETER CAPPER, 2017). In the case of ternary alloys, the alloy scattering is also important, i.e, in the atomic scale defects in alloys scatter phonons due to differences in mass or due to generation of strain fields, and the scattering cross-section follows Rayleigh scattering as $\sim \lambda^{-4}$, where λ is the phonon wavelength. Hence, short wavelength phonons are effectively scattered in alloys, but the mid-to-long wavelength phonons can propagate without significant scattering and thereby still contribute to heat conduction.

Figure 4.20 shows that the grain boundaries do not affect much the electrical properties in bulk. However, Kasap et al. (SAFA KASAP; PETER CAPPER, 2017) reported that scattering by grain boundaries and scattering at the surface need to be considered in the resistivity of thin polycrystalline films. The authors show that the resistivity of a thin polycrystalline film increases as a function of the grain size and thickness decrease. Therefore, the no clear relationship between In-Ga relative atomic concentration and electrical conductivity in $In_xGa_{1-x}Sb$ films (this work), can be explained considering these two additional effects.

As previously explained, thermal conductivity of thermoelectric materials consists of two parts: k_l, which results from heat transporting phonons travelling through the crystal lattice, and k_e, which arises from heat carrying charge carries (electrons or holes) moving through the crystal lattice. The classical approach gives k as (SAFA KASAP; PETER CAPPER, 2017) (BÖER; POHL, 2018),

$$k = \frac{C_v v_{ph} \lambda_{ph}}{3}, \qquad (16)$$

where C_v is the heat capacity per unit volume, v_{ph} is the mean phonon velocity and λ_{ph} is the mean free path. Since v_{ph} is practically constant as a function of temperature, k is dominated by C_v and λ_{ph}. At high temperatures, k is governed by phonon–phonon scattering. The phonon–phonon collisions that are normally responsible for limiting the thermal conductivity, that is scattering the phonon momentum in the opposite direction to the heat flow, are due to the anharmonicity (asymmetry) of the interatomic potential energy curve. The flipping of the phonon momentum is known as an Umklapp process and is a result of the anharmonicity in the interatomic bond (see Figure 4.21). On the other hand, at low temperatures, there are two factors that control k. The phonon concentration is too low for phonon–phonon collisions to be taken into account.

Instead, the λ_{ph} is determined by phonon collisions with crystal imperfections, most significantly, crystal surfaces and grain boundaries. Thus, λ_{ph} depends on the sample geometry and crystallinity. Moreover, as we expect from the Debye model, C_v depends on T^3 so that k has the same temperature dependence as C_v, that is k α T^3. As observed for Ge, Si and GaAs, k increases with increasing T at low temperatures, and that also depends on the concentration of dopants or impurities in the crystal, which can scatter phonons (JOSHI; VERMA, 1970)(GLASSBRENNER; SLACK, 1964) (SAFA KASAP; PETER CAPPER, 2017). From previous work (GIULIAN et al., 2020b), via Hall measurements, it was observed, for the same set of samples, a non-stoichiometric electron density for $In_xGa_{1-x}Sb$ thin films. All those factors combined (crystal surfaces, grain boundaries and impurities in the crystal) resulted in a non-stoichiometric behavior of the thermal conductivity in $In_xGa_{1-x}Sb$ thin films at room temperatures shown in Figure 4.16-(c)

Figure 4.21– schematic of the phonon–phonon anharmonic interaction that generates a new phonon whose momentum is towards the hot region.

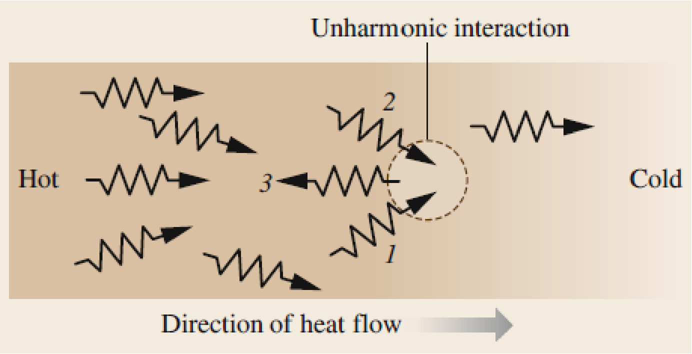

Reference: (SAFA KASAP; PETER CAPPER, 2017)

As the temperature increases, k is controlled by λ_{ph} instead of C_v, which changes only slowly with T. The λ_{ph} becomes limited by phonon–phonon collisions that obey the Umklapp process. The concentration of such phonons is proportional to $\exp(T_D/2T)$, where T_D is the Debye temperature. Since λ_{ph} is inversely proportional to the Umklapp-obeying phonon concentration, k decreases with increasing temperature, following a k α exp ($T_D/2T$) type of behavior. At temperatures higher than the Debye temperature, C_v is constant, and the phonon concentration n_{ph} increases with temperature (n_{ph} α T). Thus, the mean free path decreases as λ_{ph} α 1/T, which means that k = AT^n (with A a constant and n a negative value) type of power law to model the k–T data, and has provided an extensive table for various group IV, III–V and II–V semiconductors (ADACHI, 2009). In summary, Figure 4.22 shows the dependence of k on T for general semiconductors, which is also applied for $In_xGa_{1-x}Sb$ compounds.

Figure 4.22- Behavior of the thermal conductivity in semiconductors(left) and its comparison with $In_xGa_{1-x}Sb$ compounds.

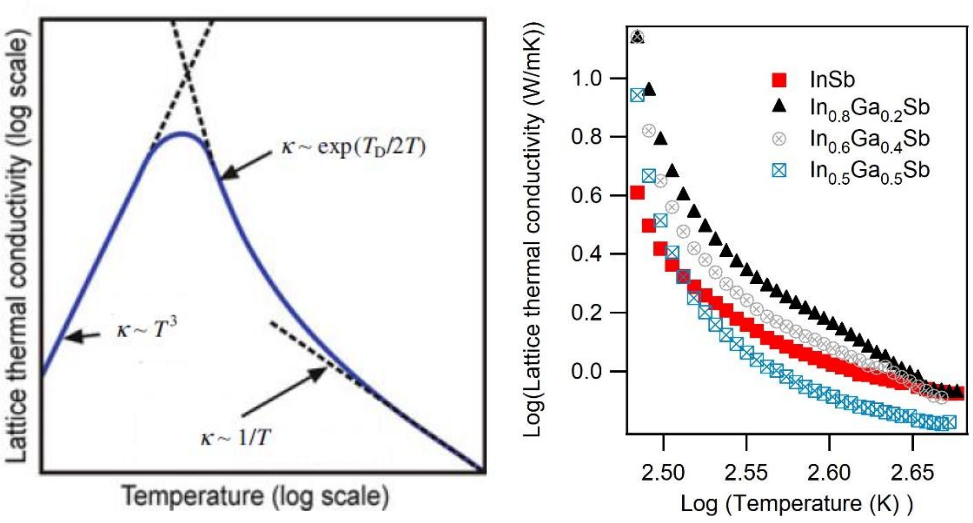

Reference: adapted from (BÖER; POHL, 2018)

An extensive study on the thermal conductivity of unirradiated semiconductors is given by Boer and Pohl (BÖER; POHL, 2018).

In principle, the addition of porosity to TE materials can significantly increase the figure of merit, ZT, by reducing the thermal conductivity. Based on the effective medium theory (BAUER, 1993), the lattice thermal conductivity of a porous material is given by:

$$k_{eff} = k\,(1 - porosity)^{1.5}. \tag{17}$$

Comparing the equation (17) with the Figure 4.19-(c), it is clear the porous dependence at room and intermediate temperatures. At high temperatures, nonetheless, the power law dominates, making the difference in porosity between the samples almost imperceptible, especially for T>450K, as shown in Figure 4.19-(c). However, porosity is also detrimental to the electrical performance for $In_{0.8}Ga_{0.2}Sb$ (see Figure 4.19-(a)) and, consequently, the figure of merit, ZT as shown in Figure 4.19-(d). A similar behavior was also reported by Lee et at. (LEE et al., 2010), analyzing the effect of nanoscale porosity of SiGe. This author observed a reduction of thermal conductivity as a function of porosity, however, the benefit was not large enough to overcome the deficit in the electrical conductivity.

It is worth mentioning, nonetheless, that Qiao et al. (QIAO et al., 2019) observed a ∼60% enhancement in ZT at room temperature, that is, from ∼0.42 for the dense film to ∼0.67 for the nanoporous Bi_2Te_3 film fabricated by evacuating over-stoichiometry Te through the grain boundary diffusion route.

5 CONCLUSIONS

The results showed that it is possible to manufacture $In_xGa_{1-x}Sb$ (x = 0.5, 0.6, 0.8 and 1) films via deposition by radio frequency magnetron sputtering onto SiO_2/Si substrates at 420 °C. GIXRD showed the formation of polycrystalline zincblende structure in as-deposited films with the lattice parameter changing linearly with composition x as predicted by Vegard`s law. Hence, the lattice parameter (and therefore bandgap) can be modulated through the In/Ga ratio in this compound. From the atomic local picture, it was observed that the lattice mismatch in $In_xGa_{1-x}Sb$ is accommodated favorably through bond bending over bond stretching. The atomic-scale structure of $In_xGa_{1-x}Sb$ was modelled through In-Sb and Ga-Sb bond lengths obtained by EXAFS, and from those values, it was possible to determine the bandgap bowing contributions (structural and electronic) arising from the change of the In-Sb and Ga-Sb bond lengths for any stoichiometry. Using this approach, we show that structural and electronic effects both account for to the bandgap change in a similar way and neither local atomic arrangements nor charge redistribution can be neglected. Moreover, for the same mixed sublattice (In and Ga), the ΔE_{elec} contribution, for x=0.5, corresponding 41% of the ΔE for $In_xGa_{1-x}P$. Regarding $In_xGa_{1-x}As$ and $In_xGa_{1-x}Sb$, ΔE_{elec} represents 30% and 33% of the ΔE, respectively, showing the importance of distinct anion sublattice.

$In_xGa_{1-x}Sb$ films upon irradiation with 16 MeV Au^{+7} ions present an specific behaviors, characteristic of antimonides, such as thickness expansion, amorphization and pore formation from a certain fluence, which strongly depend on the In/Ga ratio in the compound. This dependence, however, is not linearly stoichiometric, i.e, does not follow the Vegard`s law as observed in the isovalent $In_xAl_{1-x}Sb$ ternary alloy, which has the same crystalline structure. The most pronounced swelling was attained by the ternary compound with the highest In concentration, with a swelling significantly greater than the binary InSb film (for the same irradiation conditions). PIXE shows the films are composed of C, O, Ga, In and Sb, with C and O concentrations greatly increased by ion irradiation. The total concentration of Ga, In and Sb are not significantly modified by ion irradiation. However, RBS analysis revealed the films can be separated in two layers, with slightly different compositions, where the surface layer corresponds to approximately 18–25% of the total film thickness. O and C relative concentrations are greatly enhanced towards the surface and are greatly increased by ion irradiation, as a result of the pronounced increase in effective surface area offered by the nanofoams. The polycrystalline $In_xGa_{1-x}Sb$ films give place to amorphous structures after irradiation with 2x10^{14} cm^{-2} (16 MeV Au^{+7} ions), except for InSb and the ternary films with the highest Ga concentration ($In_{0.5}Ga_{0.5}Sb$), where the films retain part of their crystallinity, with the crystallite size decreasing from 29.3 nm to 18.4 nm, and the microstrain increasing from 0.00255 to 0.00583 in the ternary films with 50% Ga concentration.

Concerning the atomic-scale structure of $In_xGa_{1-x}Sb$ when irradiated with 8 MeV Au^{+3} ions, this alloy presents a stability in its bond length value with ion fluences ranging from 1×10^{13} cm^{-2} to 5×10^{14} cm^{-2}. This indicates that the degree of porosity has influence only in the microscale, with the material becoming porous, but in the atomic-scale, at least for the first NN distance, the same is not observed and the optical frequency shift behavior is similar before and after ion irradiation in $In_xGa_{1-x}Sb$ for the range of ion fluences used in this work.

$In_{0.8}Ga_{0.2}Sb$ exhibited the highest ZT values (0.53 at 450 K), which is a very promising result and shows that this material may be used as an efficient thermoelectric, especially considering the relatively low measurement temperature. $In_{0.8}Ga_{0.2}Sb$ films exhibit the highest Seebeck coefficient of all samples investigated, with also the highest thermal conductivity for all temperatures analysed here. A ZT value of 0.53 was found for this compound, at a measurement temperature of 450 K. The same material, after irradiation with 16 MeV Au^{+7} ions, was transformed into nanofoams, and the ZT values obtained for samples irradiated with a total fluence of 5x10^{13} cm^{-2} (1x10^{14} cm^{-2}) substantially decreased, attaining a value of 0.23 (0.12).

$In_xGa_{1-x}Sb$ nanofoams also showed a remarkable stability under annealing in vacuum at 200 °C, with very small changes in atomic concentration induced by thermal annealing. In terms of the ZT parameter, it was obtained that its value substantially decreased after ion irradiation.

These results show that $In_xGa_{1-x}Sb$ films deposited by magnetron sputtering exhibit new properties due to the exclusive combination of their crystalline structures and large internal surface areas, which allows higher adsorbate effects and lower thermal conductivity coefficient, making them very attractive for gas sensor at room and elevated temperatures.

6 REFERENCES

ADACHI, S. **Properties of Semiconductor Alloys : Group-IV , III – V and II – VI Semiconductors**. [s.l: s.n.].

ALKHALDI, H. S. et al. Void evolution and porosity under arsenic ion irradiation in GaAs1-xSbx alloys. **JOURNAL OF PHYSICS D-APPLIED PHYSICS**, v. 50, n. 12, p. 125101, mar. 2017.

AVIA. Data Sheet - HX-711. **Avia Semiconductor**, v. 1, n. 1, p. 1–9, 2017.

BAHK, J.-H.; FAVALORO, T.; SHAKOURI, A. Thin Film Thermoelectric Characterization Techniques. **Annual Review of Heat Transfer**, v. 16, n. 1, p. 51–99, 2013.

BALZAROTTI, A. et al. MODEL OF THE LOCAL-STRUCTURE OF RANDOM TERNARY ALLOYS - EXPERIMENT VERSUS THEORY. **PHYSICAL REVIEW B**, v. 31, n. 12, p. 7526–7539, 1985.

BAUER, T. H. A GENERAL ANALYTICAL APPROACH TOWARD THE THERMAL-CONDUCTIVITY OF POROUS-MEDIA. **INTERNATIONAL JOURNAL OF HEAT AND MASS TRANSFER**, v. 36, n. 17, p. 4181–4191, nov. 1993.

BERGGREN, J.; HANKE, M.; TRAMPERT, A. Bowing effect in elastic constants of dilute Ga(As,N) alloys. **APPLIED PHYSICS LETTERS**, v. 108, n. 18, maio 2016.

BERNARD, J. E.; ZUNGER, A. ELECTRONIC-STRUCTURE OF ZNS, ZNSE, ZNTE, AND THEIR PSEUDOBINARY ALLOYS. **PHYSICAL REVIEW B**, v. 36, n. 6, p. 3199–3228, ago. 1987.

BIRKHOLZ, M. **Thin Film Analysis by X-ray Scattering**. [s.l: s.n.].

BISWAS, K.; FRANCESCHETTI, A.; LANY, S. Generalized valence-force-field model of (Ga,In)(N,P) ternary alloys. **Physical Review B**, v. 78, n. 8, p. 085212, 22 ago. 2008.

BÖER, K. W.; POHL, U. W. **Semiconductor physics**. [s.l: s.n.].

BOLZAN, C. A. et al. Stoichiometry-dependent porosity by ion irradiation: In(1-x)Al(x)Sb films. **Journal of Physics and Chemistry of Solids**, v. 148, p. 109769, 2021a.

BOLZAN, C. A. et al. Local structure of porous InSb films: From first to third-shell EXAFS investigation. **Solid State Sciences**, v. 119, n. February, p. 106705, 2021b.

BOLZAN, C. A. et al. Stoichiometry-dependent porosity by ion irradiation: In(1-x)Al(x)Sb films. **JOURNAL OF PHYSICS AND CHEMISTRY OF SOLIDS**, v. 148, jan. 2021c.

BOLZAN, C. A. et al. Local and extended atomic structure of strained polycrystalline In(1-x)Al(x)Sb alloys. **JOURNAL OF PHYSICS AND CHEMISTRY OF SOLIDS**, v. 150, mar. 2021d.

BOYCE, J. B.; MIKKELSEN, J. C. Local structure of pseudobinary semiconductor alloys: An x-ray absorption fine structure study. **Journal of Crystal Growth**, v. 98, n. 1–2, p. 37–43, 1 nov. 1989.

BRACCO, G.; HOLST, B. **Surface Science Techniques**. [s.l: s.n.]. v. 51

BUNKER, G. **Introduction to XAFS**. [s.l: s.n.].

CAI, Y.; THORPE, M. F. LENGTH MISMATCH IN RANDOM SEMICONDUCTOR ALLOYS .2. STRUCTURAL CHARACTERIZATION OF PSEUDOBINARIES. **PHYSICAL REVIEW B**, v. 46, n. 24, p. 15879–15886, dez. 1992.

CARLES, R.; LANDA, G.; RENUCCI, J. B. BOND RELAXATION PHENOMENON AND IMPURITY MODES FREQUENCIES IN III-V-COMPOUNDS. **SOLID STATE COMMUNICATIONS**, v. 53, n. 2, p. 179–182, 1985.

CHANG, S. L. Thin-film characterization by grazing incidence X-ray diffraction and multiple beam interference. **JOURNAL OF PHYSICS AND CHEMISTRY OF SOLIDS**, v. 62, n. 9–10, p. 1765–1775, 2001.

CHEN, A. B.; SHER, A. SEMICONDUCTOR PSEUDOBINARY ALLOYS - BOND-LENGTH RELAXATION AND MIXING ENTHALPIES. **PHYSICAL REVIEW B**, v. 32, n. 6, p. 3695–3711, 1985.

CHEN, G.; SUN, W.; LV, Y. Empirical expression for the composition and temperature dependence of the energy gap in InAlSb. **INFRARED PHYSICS & TECHNOLOGY**, v. 81, p. 262–265, mar. 2017.

COHEN, M. L. Calculation of bulk moduli of diamond and zincblende solids.

PHYSICAL REVIEW B, v. 32, n. 12, p. 7988–7991, 1985.

DATTA, D. P.; SOM, T. Nanoporosity-induced superhydrophobicity and large antireflection in InSb. **APPLIED PHYSICS LETTERS**, v. 108, n. 19, maio 2016.

DE ANDRADE, A. M. H. et al. Ion irradiation-induced polycrystalline InSb foam. **Journal of Physics D: Applied Physics**, v. 50, n. 48, p. 485104, 2017.

DESTEFANIS, G. L.; GAILLIARD, J. P. VERY EFFICIENT VOID FORMATION IN ION-IMPLANTED INSB. **APPLIED PHYSICS LETTERS**, v. 36, n. 1, p. 40–42, 1980.

DU, Z. et al. Effect of Ga alloying on thermoelectric properties of InSb. **CURRENT APPLIED PHYSICS**, v. 18, n. 8, p. 893–897, ago. 2018.

DU, Z.; YAN, M.; ZHU, J. Thermoelectric performance of In0.8+yGa0.2Sb (0 <= y <= 0.06) ternary solid solutions with In excess. **MATERIALS RESEARCH EXPRESS**, v. 5, n. 10, out. 2018.

DUTTA, P. S.; BHAT, H. L.; KUMAR, V. The physics and technology of gallium antimonide: An emerging optoelectronic material. **JOURNAL OF APPLIED PHYSICS**, v. 81, n. 9, p. 5821–5870, maio 1997.

ECKNER, S. et al. Bond-strength inversion in (In,Ga)As semiconductor alloys. **PHYSICAL REVIEW B**, v. 97, n. 19, maio 2018.

FENG, Z. C. et al. RAMAN AND INFRARED-SPECTROSCOPY OF IN1-XGAXSB FILMS GROWN ON GAAS BY METAL-ORGANIC MAGNETRON SPUTTERING. **CANADIAN JOURNAL OF PHYSICS**, v. 69, n. 3–4, p. 386–389, 1991.

FOELL, H.; CARSTENSEN, J.; FREY, S. Porous and nanoporous semiconductors and emerging applications. **JOURNAL OF NANOMATERIALS**, n. 2, p. 91635, 2006.

GIULIAN, R. et al. Structural and electronic characterization of antimonide films made by magnetron sputtering. **Journal of Physics D: Applied Physics**, v. 50, n. 7, p. 075106, 2017a.

GIULIAN, R. et al. Ion irradiation-induced polycrystalline InSb foam. **Journal of Physics D: Applied Physics**, v. 50, n. 48, p. 485104, dez. 2017b.

GIULIAN, R. et al. Ion irradiation effects on Sb-rich GaSb films. **MATERIALS RESEARCH EXPRESS**, v. 6, n. 2, p. 026425, fev. 2019.

GIULIAN, R. et al. Ion irradiation-induced foams in antimonide binary alloys: A combination of small energy bandgap with giant surface-to-bulk ratio. **Energy Reports**, v. 6, n. 4, p. 70–76, fev. 2020a.

GIULIAN, R. et al. Atomic composition, structure, and electrical properties of In1-xGaxSb films deposited by magnetron sputtering. **Thin Solid Films**, v. 709, p. 138213, 1 set. 2020b.

GLASSBRENNER, C. J.; SLACK, G. A. Thermal Conductivity of Silicon and Germanium from 3°K to the Melting Point. **Physical Review**, v. 134, n. 4A, p. A1058–A1069, 1964.

GLOVER, C. J.; FORAN, G. J.; RIDGWAY, M. C. Structure of amorphous silicon investigated by EXAFS. **Nuclear Inst. and Methods in Physics Research, B**, v. 199, p. 195–199, jan. 2003.

GREIN, C. H. et al. Long wavelength InAs/InGaSb infrared detectors: Optimization of carrier lifetimes. **Journal of Applied Physics**, v. 78, n. 12, p. 7143–7152, 1995.

H., R.; RUGE, I. **Ion implatation**. [s.l: s.n.].

HASS, K. C.; LEMPERT, R. J.; EHRENREICH, H. EFFECTS OF CHEMICAL AND STRUCTURAL DISORDER IN SEMICONDUCTING PSEUDOBINARY ALLOYS. **PHYSICAL REVIEW LETTERS**, v. 52, n. 1, p. 77–80, 1984.

HE, P.; WU, Y. Constructing of highly porous thermoelectric structures with improved thermoelectric performance. **NANO RESEARCH**, v. 14, n. 10, SI, p. 3608–3615, out. 2021.

HILL, R. ENERGY-GAP VARIATIONS IN SEMICONDUCTOR ALLOYS. **JOURNAL OF PHYSICS C-SOLID STATE PHYSICS**, v. 7, n. 3, p. 521–526, 1974.

HINRICHS, R. **Técnicas instrumentais não destrutivas aplicadas a gemas do Rio Grande do Sul**. [s.l: s.n.].

HOSOKAWA, S. et al. X-ray fluorescence holography of In1 - x Gax Sb mixed crystal. **Journal of Crystal Growth**, v. 311, n. 3, p. 978–981, 15 jan. 2009.

HUSSAIN, Z. S. et al. Rapid ion-implantation-induced amorphization of InxGa1-xAs relative to InAs and GaAs. **PHYSICAL REVIEW B**, v. 79, n. 8, p. 085202, fev. 2009.

HUSSAIN, Z. S. et al. Ion-implantation-induced amorphization of InxGa1-xP alloys as functions of stoichiometry and temperature. **JOURNAL OF APPLIED PHYSICS**, v. 119, n. 19, p. 195702, maio 2016.

JAESCHKE, E. J.; HASTINGS, J. B. **Synchrotron Light Sources and Free-Electron Lasers**. [s.l: s.n.].

JEONG, I. K. et al. Local structure of Inx Ga1 − x As semiconductor alloys by high-energy synchrotron x-ray diffraction. **Physical Review B**, v. 63, n. 20, p. 205202, 9 abr. 2001.

JIANG, G. et al. Microstructure and thermoelectric properties of InSb compound with nonsoluble NiSb in situ precipitates. **JOURNAL OF MATERIALS RESEARCH**, v. 28, n. 24, p. 3394–3400, dez. 2013.

JOSHI, Y. P.; VERMA, G. S. ANALYSIS OF PHONON CONDUCTIVITY - APPLICATION TO SI. **PHYSICAL REVIEW B-SOLID STATE**, v. 1, n. 2, p. 750-, 1970.

KACHKANOV, V. et al. Local structure of luminescent InGaN alloys. **Applied Physics Letters**, v. 89, n. 10, p. 101908, 4 set. 2006.

KATSIKINI, M. et al. **Microstructural characterization of InxGa 1-x N MBE samples**. Nuclear Instruments and Methods in Physics Research, Section B: Beam Interactions with Materials and Atoms. **Anais**...North-Holland, 1 jan. 2003

KELLY, P. J.; ARNELL, R. D. Magnetron sputtering : a review of recent developments and applications. **Vacuum**, v. 56, n. 3, p. 159–172, 2000a.

KELLY, P. J.; ARNELL, R. D. Magnetron sputtering: a review of recent developments and applications. **VACUUM**, v. 56, n. 3, p. 159–172, mar. 2000b.

KHALIQ, J. et al. Utilizing the phonon glass electron crystal concept to improve the thermoelectric properties of combined Yb-stuffed and Te-substituted CoSb3. **SCRIPTA MATERIALIA**, v. 72–73, p. 63–66, fev. 2014.

KIM, H. S. et al. Relationship between thermoelectric figure of merit and energy conversion efficiency. **Proceedings of the National Academy of Sciences of the United States of America**, v. 112, n. 27, p. 8205–8210, 2015.

KINGERY, W. D. **Introduction to Ceramics**. [s.l: s.n.].

KLUTH, P. et al. Extended x-ray absorption fine structure study of porous GaSb formed by ion implantation. **JOURNAL OF APPLIED PHYSICS**, v. 110, n. 11, dez. 2011.

KLUTH, P. et al. Nano-porosity in GaSb induced by swift heavy ion irradiation. **APPLIED PHYSICS LETTERS**, v. 104, n. 2, p. 023105, jan. 2014.

KLUTH, S. M.; LLEWELLYN, D.; RIDGWAY, M. C. Irradiation fluence dependent microstructural evolution of porous InSb. **NUCLEAR INSTRUMENTS & METHODS IN PHYSICS RESEARCH SECTION B-BEAM INTERACTIONS WITH MATERIALS AND ATOMS**, v. 242, n. 1–2, p. 640–642, jan. 2006.

KONINGSBERGER, D. .; PRINS, R. **X-ray Absorption**. [s.l: s.n.].

KOROTCENKOV, G.; CHO, B. K. Porous Semiconductors: Advanced Material for Gas Sensor Applications. **CRITICAL REVIEWS IN SOLID STATE AND MATERIALS SCIENCES**, v. 35, n. 1, p. 1–37, 2010.

KOTESKI, V. et al. Bond lengths in Cd-1-xZnxTe beyond linear laws revisited. **JOURNAL OF ALLOYS AND COMPOUNDS**, v. 371, n. 1–2, p. 138–141, maio 2004.

KOZHEMYAKIN, G. N. Indium inhomogeneity in InxGa1-xSb ternary crystals grown by floating crucible Czochralski method. **JOURNAL OF CRYSTAL GROWTH**, v. 220, n. 1–2, p. 39–45, nov. 2000.

KUMAR, V. N. et al. Effects of varying indium composition on the thermoelectric properties of InxGa1-xSb ternary alloys. **APPLIED PHYSICS A-MATERIALS SCIENCE & PROCESSING**, v. 122, n. 10, out. 2016.

KUMAR, V. N. et al. An Approach to Optimize the Thermoelectric Properties of III-V Ternary InGaSb Crystals by Defect Engineering via Point Defects and Microscale Compositional Segregations. **INORGANIC CHEMISTRY**, v. 58, n. 17, p. 11579–11588, set. 2019.

LANGA, S. et al. Waveguide structures based on porous indium phosphide. **ELECTROCHEMICAL AND SOLID STATE LETTERS**, v. 8, n. 2, p. C30–C32, 2005.

LEE, H. et al. Effects of nanoscale porosity on thermoelectric properties of SiGe. **JOURNAL OF APPLIED PHYSICS**, v. 107, n. 9, maio 2010.

LI, D. et al. Flexible Near-Infrared InGaSb Nanowire Array Detectors with Ultrafast Photoconductive Response Below 20 µs. **Advanced Optical Materials**, v. 8, n. 22, p. 1–7, 2020.

LI, W. et al. Low Sound Velocity Contributing to the High Thermoelectric Performance of Ag8SnSe6. **ADVANCED SCIENCE**, v. 3, n. 11, nov. 2016.

MANZO, D. J. et al. Structural and compositional analysis of GaSb nanofoams obtained by ion irradiation of sputtered films. **THIN SOLID FILMS**, v. 687, p. UNSP 137447, out. 2019.

MARTIN, R. M. Elastic properties of ZnS structure semiconductors. **Physical Review B**, v. 1, n. 10, p. 4005–4011, 15 maio 1970.

MARTINS, J. L.; ZUNGER, A. BOND LENGTHS AROUND ISOVALENT IMPURITIES AND IN SEMICONDUCTOR SOLID-SOLUTIONS. **PHYSICAL REVIEW B**, v. 30, n. 10, p. 6217–6220, 1984.

MASON, S. J. et al. Determining absolute Seebeck coefficients from relative thermopower measurements of thin films and nanostructures. **JOURNAL OF APPLIED PHYSICS**, v. 127, n. 8, fev. 2020.

MAURYA, D. K.; SARDARINEJAD, A.; ALAMEH, K. Recent Developments in RF Magnetron Sputtered Thin Films for pH Sensing Applications-An Overview. **COATINGS**, v. 4, n. 4, p. 756–771, dez. 2014.

MAXWELL, J. A.; CAMPBELL, J. L.; TEESDALE, W. J. THE GUELPH PIXE SOFTWARE PACKAGE. **NUCLEAR INSTRUMENTS & METHODS IN PHYSICS RESEARCH SECTION B-BEAM INTERACTIONS WITH MATERIALS AND ATOMS**, v. 43, n. 2, p. 218–230, set. 1989.

MAYER, M. **SIMNRA, a simulation program for the analysis of NRA, RBS and ERDA**. (Duggan, JL and Morgan, IL, Ed.)APPLICATION OF ACCELERATORS IN RESEARCH AND INDUSTRY, PTS 1 AND 2. **Anais**...: AIP CONFERENCE PROCEEDINGS.2 HUNTINGTON QUADRANGLE, STE 1NO1, MELVILLE, NY 11747-4501 USA: AMER INST PHYSICS, 1999

MAYER, M. et al. Rutherford backscattering analysis of porous thin TiO2 films. **NUCLEAR INSTRUMENTS & METHODS IN PHYSICS RESEARCH SECTION B-BEAM INTERACTIONS WITH MATERIALS AND ATOMS**, v. 273, p. 83–87, fev. 2012.

MAYER, M. **SIMNRA User ' s Guide**, 2017.

MIKKELSEN, J. C.; BOYCE, J. B. Extended x-ray-absorption fine-structure study of Ga1-xInxAs random solid solutions. **Physical Review B**, v. 28, n. 12, p. 7130–7140, 15 dez. 1983.

MINNICH, A. J. et al. Bulk nanostructured thermoelectric materials: current research and future prospects. **ENERGY & ENVIRONMENTAL SCIENCE**, v. 2, n. 5, p. 466–479, 2009.

MIYANO, K. E. et al. Extended x-ray absorption fine structure study of AlxGa(1-x)N films. **Applied Physics Letters**, v. 70, n. 16, p. 2108–2110, 21 abr. 1997.

NAGUIB, H. M.; KELLY, R. CRITERIA FOR BOMBARDMENT-INDUCED STRUCTURAL-CHANGES IN NON-METALLIC SOLIDS. **RADIATION EFFECTS AND DEFECTS IN SOLIDS**, v. 25, n. 1, p. 1–12, 1975.

NEE, A. Y. C. **Handbook of manufacturing engineering and technology**. [s.l: s.n.].

NEWVILLE, M. IFEFFIT: interactive XAFS analysis and FEFF fitting. **JOURNAL OF SYNCHROTRON RADIATION**, v. 8, n. 2, p. 322–324, mar. 2001.

NEWVILLE, M. Fundamentals of XAFS. In: HENDERSON, GS AND NEUVILLE, DR AND DOWNS, R. (Ed.). . **Spectroscopic methods in mineralology and materials sciences**. Reviews in Mineralogy & Geochemistry. 3635 Concorde PKWY STE 500, Chantilly, VA 20151-1125 USA: Mineralogical Soc Amer & Geochemical Soc, 2014. v. 78p. 33+.

NISHIMOTO, N.; FUJIHARA, J. Characterization of a Flexible InGaSb/PI Thin Film Grown by RF Magnetron Sputtering and Aqueous Stability Improvement via Surface Coating. **Physica Status Solidi (A) Applications and Materials Science**, v. 216, n. 4, p. 1–8, 2019.

NITTA, N. et al. Void Formation and Structure Change Induced by Heavy Ion

Irradiation in GaSb and InSb. **Materials Transactions**, v. 51, n. 6, p. 1059–1063, 2010.

NITTA, N.; TANIWAKI, M. Novel nano-fabrication technique utilizing ion beam. **NUCLEAR INSTRUMENTS & METHODS IN PHYSICS RESEARCH SECTION B-BEAM INTERACTIONS WITH MATERIALS AND ATOMS**, v. 206, p. 482–485, maio 2003.

NOTTHOFF, C. et al. Structural properties of nano-porous GaSb prepared by swift heavy-ion irradiation. **Nuclear Inst. and Methods in Physics Research B**, v. 435, p. 126–132, nov. 2018.

PELLICER-PORRES, J. et al. X-ray-absorption fine-structure study of ZnSexTe1-x alloys. **JOURNAL OF APPLIED PHYSICS**, v. 96, n. 3, p. 1491–1498, ago. 2004.

QIAO, J. et al. Tailoring Nanoporous Structures in Bi2Te3 Thin Films for Improved Thermoelectric Performance. **ACS Applied Materials and Interfaces**, v. 11, n. 41, p. 38075–38083, 2019.

REDDY, R. R. et al. Dependence of physical parameters of compound semiconductors on refractive index. **DEFENCE SCIENCE JOURNAL**, v. 53, n. 3, p. 239–248, jul. 2003.

REFAAT, T. F. et al. InGaSb photodetectors using an InGaSb substrate for 2 μm applications. **Applied Physics Letters**, v. 85, n. 11, p. 1874–1876, 2004.

REHR, J. J.; ALBERS, R. C. Scattering-matrix formulation of curved-wave multiple-scattering theory: Application to x-ray-absorption fine structure. **Physical Review B**, v. 41, n. 12, p. 8139–8149, 15 abr. 1990.

REHR, J. J.; ALBERS, R. C. Theoretical approaches to x-ray absorption fine structure. **REVIEWS OF MODERN PHYSICS**, v. 72, n. 3, p. 621–654, jul. 2000.

RIDGWAY, M. C. et al. Ion-dose-dependent microstructure in amorphous Ge. **PHYSICAL REVIEW B**, v. 61, n. 19, p. 12586–12589, maio 2000.

RIDGWAY, M. C. et al. Common structure in amorphised compound semiconductors. **Nuclear Inst. and Methods in Physics Research, B**, v. 199, p. 235–239, jan. 2003.

ROSSETTO, L. **Dispositivo para análise e caracterização de materiais**

semicondutores utilizados como sensores de gás. [s.l: s.n.].

RUCKER, H.; METHFESSEL, M. ANHARMONIC KEATING MODEL FOR GROUP-IV SEMICONDUCTORS WITH APPLICATION TO THE LATTICE-DYNAMICS IN ALLOYS OF SI, GE, AND C. **PHYSICAL REVIEW B**, v. 52, n. 15, p. 11059–11072, out. 1995.

SAFA KASAP; PETER CAPPER. **Electronic and Photonic Materials**. [s.l: s.n.].

SALES, B. C. et al. Filled skutterudite antimonides: Electron crystals and phonon glasses. **PHYSICAL REVIEW B**, v. 56, n. 23, p. 15081–15089, dez. 1997.

SCHATTEN, H. **Scanning electron microscopy for the life sciences**. [s.l: s.n.].

SCHIWIETZ, G. et al. Femtosecond dynamics - snapshots of the early ion-track evolution. **NUCLEAR INSTRUMENTS & METHODS IN PHYSICS RESEARCH SECTION B-BEAM INTERACTIONS WITH MATERIALS AND ATOMS**, v. 225, n. 1–2, p. 4–26, ago. 2004.

SCHNOHR, C. S. et al. Comparison of the atomic structure of InP amorphized by electronic or nuclear ion energy-loss processes. **PHYSICAL REVIEW B**, v. 77, n. 7, fev. 2008.

SCHNOHR, C. S. et al. Atomic-scale structure and band-gap bowing in Cu(In,Ga)Se 2. **Physical Review B**, v. 85, n. 24, p. 245204, 6 jun. 2012.

SCHNOHR, C. S. Structural and electronic contributions to the bandgap bowing of (In,Ga)P alloys. **JOURNAL OF PHYSICS-CONDENSED MATTER**, v. 24, n. 32, ago. 2012.

SCHNOHR, C. S. Compound semiconductor alloys: From atomic-scale structure to bandgap bowing. **APPLIED PHYSICS REVIEWS**, v. 2, n. 3, set. 2015.

SCHNOHR, C. S.; MARK, C. R. **X-Ray Absorption Spectroscopy of Semiconductors**. [s.l: s.n.].

SEGMULLER, A. Characterization of Epitaxial Films By X-Ray Diffraction. **Thin Solid Films**, v. 154, p. 33–42, 1987.

SHEN, S. G. BOND LENGTHS AROUND ISOVALENT IMPURITIES AND IN SEMICONDUCTOR SOLID-SOLUTIONS. **JOURNAL OF PHYSICS-CONDENSED**

MATTER, v. 6, n. 24, p. 4449–4456, jun. 1994.

SHIH, C. K. et al. BOND-LENGTH RELAXATION IN PSEUDOBINARY ALLOYS. **PHYSICAL REVIEW B**, v. 31, n. 2, p. 1139–1140, 1985.

SWANN, S. Magnetron sputtering. **Physics in Technology**, v. 19, n. 2, p. 67–75, 1988.

THOME, L. et al. Combined effects of nuclear and electronic energy losses in solids irradiated with a dual-ion beam. **APPLIED PHYSICS LETTERS**, v. 102, n. 14, p. 141906, abr. 2013.

TIT, N.; OBAIDAT, I. M.; ALAWADHI, H. Origins of bandgap bowing in compound-semiconductor common-cation ternary alloys. **JOURNAL OF PHYSICS-CONDENSED MATTER**, v. 21, n. 7, fev. 2009a.

TIT, N.; OBAIDAT, I. M.; ALAWADHI, H. Absence of the bowing character in the common-anion II-VI ternary alloys. **JOURNAL OF ALLOYS AND COMPOUNDS**, v. 481, n. 1–2, p. 340–344, jul. 2009b.

TOULEMONDE, M. et al. MeV gold irradiation induced damage in alpha-quartz: Competition between nuclear and electronic stopping. **NUCLEAR INSTRUMENTS & METHODS IN PHYSICS RESEARCH SECTION B-BEAM INTERACTIONS WITH MATERIALS AND ATOMS**, v. 178, p. 331–336, maio 2001.

TOULEMONDE, M. et al. Synergy of nuclear and electronic energy losses in ion-irradiation processes: The case of vitreous silicon dioxide. **PHYSICAL REVIEW B**, v. 83, n. 5, p. 054106, fev. 2011.

TRACHENKO, K. Understanding resistance to amorphization by radiation damage. **JOURNAL OF PHYSICS-CONDENSED MATTER**, v. 16, n. 49, p. R1491–R1515, dez. 2004.

VURGAFTMAN, I.; MEYER, J. R.; RAMMOHAN, L. R. High-power/low-threshold type-II interband cascade mid-IR laser - Design and modeling. **IEEE PHOTONICS TECHNOLOGY LETTERS**, v. 9, n. 2, p. 170–172, fev. 1997.

WANG, C. A. et al. High-quantum-efficiency 0.5 eV GaInAsSb/GaSb thermophotovoltaic devices. **Applied Physics Letters**, v. 75, n. 9, p. 1305–1307, 1999.

WENDLER, E.; WESCH, W. Ar implantation of InSb and AlN at 15 K. **Nuclear Instruments and Methods in Physics Research, Section B: Beam Interactions with Materials and Atoms**, v. 242, n. 1–2, p. 562–564, 2006.

WESCH, W.; WENDLER, E. **Ion beam modification of solids : ion-solid interaction and radiation damage**. [s.l: s.n.].

WESCH, W.; WENDLER, E.; SCHNOHR, C. S. Damage evolution and amorphization in semiconductors under ion irradiation. **Nuclear Instruments and Methods in Physics Research, Section B: Beam Interactions with Materials and Atoms**, v. 277, p. 58–69, 2012.

WIDJONARKO, N. E. Introduction to Advanced X-ray Diffraction Techniques for Polymeric Thin Films. **COATINGS**, v. 6, n. 4, dez. 2016.

WOLENSKI, C. et al. Composition and surface deformation variance in highly strained In x Ga 1−x Sb structures on (100) GaSb . **Journal of Vacuum Science & Technology A: Vacuum, Surfaces, and Films**, v. 34, n. 2, p. 021403, 2016.

WU, L. et al. **Enhanced Thermoelectric Performance in Cu-Intercalated BiTeI by Compensation Weakening Induced Mobility Improvement**. [s.l: s.n.]. v. 5

WU, Z. et al. Extended x-ray-absorption fine-structure study of GaAsxP1-x semiconducting random solid solutions. **Physical Review B**, v. 48, n. 12, p. 8694–8700, 15 set. 1993.

YANG, L. et al. High Performance Thermoelectric Materials: Progress and Their Applications. **ADVANCED ENERGY MATERIALS**, v. 8, n. 6, fev. 2018.

YONGQIANG, W.; MICHAEL, N. **Handbook of Modern Ion Beam Materials Analysis**. 2. ed. [s.l: s.n.].

YU, K. M. et al. Local structures of free-standing AlxGa1-xN thin films studied by extended x-ray absorption fine structure. **Applied Physics Letters**, v. 75, n. 26, p. 4097–4099, 27 dez. 1999.

ZAK, A. K. et al. X-ray analysis of ZnO nanoparticles by Williamson-Hall and size-strain plot methods. **SOLID STATE SCIENCES**, v. 13, n. 1, p. 251–256, jan. 2011.

ZHANG, Q. et al. Enhanced thermoelectric performance in In1-xGaxSb originating from the scattering of point defects and nanoinclusion. **JOURNAL OF MATERIALS CHEMISTRY**, v. 21, n. 33, p. 12398–12401, 2011.

ZHANG, Q. et al. Deep defect level engineering: a strategy of optimizing the carrier concentration for high thermoelectric performance. **ENERGY & ENVIRONMENTAL SCIENCE**, v. 11, n. 4, p. 933–940, abr. 2018.

ZHENG, X. F. et al. A review of thermoelectrics research - Recent developments and potentials for sustainable and renewable energy applications. **RENEWABLE & SUSTAINABLE ENERGY REVIEWS**, v. 32, p. 486–503, abr. 2014.

ZHOU, C. et al. Defect Engineering for High-Performance n-Type PbSe Thermoelectrics. **JOURNAL OF THE AMERICAN CHEMICAL SOCIETY**, v. 140, n. 29, p. 9282–9290, jul. 2018.

ZHOU, F. et al. Effect of growth base pressure on the thermoelectric properties of indium antimonide nanowires. **JOURNAL OF PHYSICS D-APPLIED PHYSICS**, v. 43, n. 2, jan. 2010.

ZIEGLER, J. F.; BIERSACK, J. P.; ZIEGLER, M. D. **The stopping and ranges of ions in matter**. [s.l: s.n.].

ZUNGER, A.; JAFFE, J. E. STRUCTURAL ORIGIN OF OPTICAL BOWING IN SEMICONDUCTOR ALLOYS. **PHYSICAL REVIEW LETTERS**, v. 51, n. 8, p. 662–665, 1983.

7 APPENDIX A- MODEL BY BALZAROTTI ET AL. AND BANDGAP BOWING.

Balzarotti *et al.* describes, using the Keating VFF potential, for the whole compositional range, the bimodal distribution of NN distances observed in $A_{(1-x)}B_{(x)}C$ ternary alloys, in terms of distortion of the anion sublattice (the cation sublattice is assumed to remain fixed) with use only of the lattice constants of the alloy and the bond-stretching constants of each binary component. In the ternary alloy, there are five possible first NN configurations (see Figure 7.1), where n denotes the number of B-type atoms, varying between 0 and 4, whereas the number of A-type atoms is given by 4-n. The first NN distances measured by EXAFS correspond to the mean value of A-C and B-C distance distribution, namely, $< d_A(x) >$ and $< d_B(x) >$. Balzarotti *et al.* reported that these variable can be obtained at a given composition x as the weighted average over the individual A-C (d_A^n) and B-C (d_B^n) distances, considering a binomial Bernoulli ($P^n(x) = \frac{4!x^n(1-x)^{4-n}}{n!(4-n)!}$) distribution as the probability of finding a tetrahedron with n B-type cations. The three-step process to calculate d_A^n and d_B^n values is well discussed on references (BALZAROTTI et al., 1985) and (SCHNOHR, 2012) . It should be noted, however, that the position of the central C and consequently the first NN distances are estimated through minimization of the sum of the bond stretching terms of the VFF potential, i.e, $U_i(x)$. For an n-type tetrahedron, $U_i(x)$ can be equated as

Figure 7.1- Different first nearest neighbor configurations surrounding the central C atom (black) of the common sublattice in ternary III-V semiconductor alloys with zincblende structure. The mixed sublattice, and thus the first nearest neighbor shell, is populated with A (blue) and B (green) atoms. The configurations are characterized by the number, n, of B atoms.

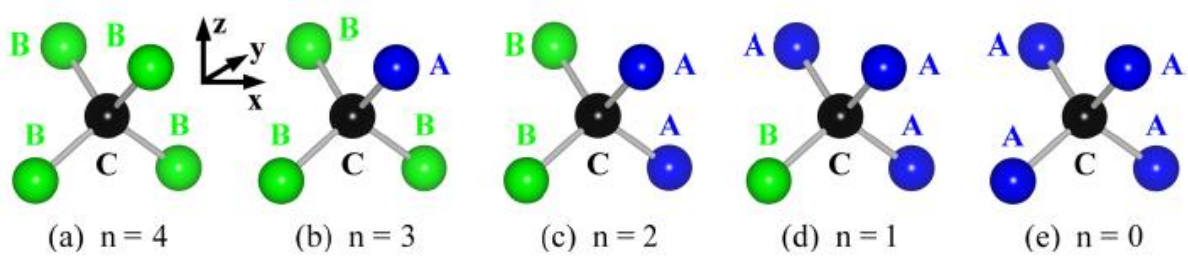

(a) n = 4 (b) n = 3 (c) n = 2 (d) n = 1 (e) n = 0

Reference: adapted from (SCHNOHR, 2015).

$$U_i(x) = \frac{3\alpha_{BC}n\left(\left(d_{BC}^{n}(x)\right)^2-\left(d_{BC}^{bin}\right)^2\right)}{8\left(d_{BC}^{bin}\right)^2} + \frac{3\alpha_{AC}(4-n)\left(\left(d_{AC}^{n}(x)\right)^2-\left(d_{AC}^{bin}\right)^2\right)}{8\left(d_{AC}^{bin}\right)^2}, \qquad \text{(A.1)}$$

where α_{BC} and α_{AC} represent the bond stretching force constants for A-C and B-C, in this order. In the last step, the bond bending term is not considered due to the fact that the respective force constant to be significantly smaller than the bond stretching force constant. The force constants used in this model for $In_xGa_{1-x}Sb$ alloys were taken from (MARTIN, 1970) as k_{Ga} = 33.16 N/m and k_{In} = 29.61 N/m, whereas the binary bond lengths ${d^{bin}}_{In}$ and ${d^{bin}}_{Ga}$ were obtained from EXAFS measurements(Table 4.2). From Figure 4.5 , it is clear the excellent agreement of the In-Sb distance obtained using Balzarotti *et al* model and EXAFS measurements, whilst for Ga-Sb distance, the model slightly overestimates the EXAFS results. This small difference is probably relative to the change in the bond stretching force constants as mentioned by Biswas *et al.* (BISWAS; FRANCESCHETTI; LANY, 2008) and determined by Eckner *et al*.(ECKNER et al., 2018).

There are many different models to predict the bandgap bowing in ternary III-V semiconductors alloys (BERNARD; ZUNGER, 1987). The earliest model used in $A_{(1-x)}B_{(x)}C$ alloys was the VCA model, which can explain properly the stoichiometry-dependency of some properties such as lattice parameter in ternary alloys. In 1974, Hill (HILL, 1974) derived an analytical equation that correlate the physical origin of the bowing parameter to the nonlinear dependence of the crystal potential on the properties of the component ions. Using this approach, the bandgap bowing estimated was 0.41eV for $In_xGa_{1-x}Sb$, which is close to the experimental value of 0.42 eV at 300 K reported in literature(ADACHI, 2009). However, this model neglects charge redistribution and polarization owing to the different properties of Ga and In atoms. The bandgap bowing of ternary alloy semiconductors have long been known to be correlated with changes in the microscopic atomic structure of the alloy (ZUNGER; JAFFE, 1983)(HASS; LEMPERT; EHRENREICH, 1984) and electronic effects resultant of charge redistribution between the anion and the two different cations. In order to distinguish structural and electronic effects in the bandgap bowing parameter, Schnohr (SCHNOHR, 2012) has proposed a two-step process to transform the AC and BC parent compounds to the $A_{(1-x)}B_{(x)}C$ alloy. In the first step, it occurs the compression or dilation of A-C and B-C bonds directly to the different individual first NN distances at any specific composition x. This step corresponds only to the local atomic arrangements, yielding a contribution ΔE_{struc} to the bandgap bowing. In the second step, while conserving all first NN distances at their values obtained in the first step, an appropriate mixing of different A-C and B-C bonds happen, allowing a charge redistribution between A,B and C atoms. This solely change in the charge configuration corresponds to a contribution ΔE_{elec} to the bandgap bowing. The total bandgap bowing (ΔE) can be defined, hence, as the sum of the structural and electronic contributions.

$$\Delta E = \Delta E_{struc} + \Delta E_{elec} \tag{A.2}$$

with the corresponding bowing parameter as

$$\mathrm{b} = b_{struc} + b_{elec} \tag{A.3}$$

The structural contribution ΔE_{struc} can be calculated using Balzarotti *et al.* model, where the A-C and B-C distances are calculated for each of all five different first NN configurations characterized by the number, n, of B atoms. The corresponding energy difference from compressing or dilating the A-C and B-C bonds are, respectively, expressed by (SCHNOHR, 2012):

$$\Delta E^{A-C}(x) = \sum_{n=0}^{4} \frac{P^n(x) 3(4-n) \gamma_{A-C} \ln\left(\frac{d_A^{bin}}{d_A^n(x)}\right)}{4}, \tag{A.4}$$

$$\Delta E^{B-C}(x) = \sum_{n=0}^{4} \frac{P^n(x) 3n \gamma_{B-C} \ln\left(\frac{d_b^{bin}}{d_b^n(x)}\right)}{4}, \tag{A.5}$$

with $P^n(x)$ being the probability for each type of tetrahedron, whereas $\mathrm{d}^{\mathrm{bin}}{}_{\mathrm{A}}$ and $\mathrm{d}^{\mathrm{bin}}{}_{\mathrm{B}}$ stand for the bond lengths of the binary parent compounds. γ_{A-C} and γ_{B-C} represent the deformation potential, in this order, for A-C and B-C bonds. Then, ΔE_{struc} follows the sum of the two terms in equation (A.6), expressly,

$$\Delta E_{struc}(x) = \Delta E^{A-C}(x) + \Delta E^{B-C}(x). \quad \text{(A.6)}$$

Figure 7.2 shows ΔE_{struc} and the experimentally determined ΔE values for $In_xGa_{1-x}Sb$ (ADACHI, 2009). The deformation potential used in the calculation was $\gamma_{GaSb} = -8.3\ eV$ and $\gamma_{InSb} = -7.0\ eV$ (ADACHI, 2009). From this figure, the ΔE_{struc} contribution is significant to the total bandgap bowing, however, it does not cover the full magnitude of it. The remaining bandgap bowing corresponds to ΔE_{elec} which also constitutes a significant contribution to ΔE. Hence, structural and electronic effects both contribute to the bandgap change in a similar way and neither local atomic arrangements nor charge redistribution can be neglected. A similar result was obtained for $Ga_{(1-x)}In_{(x)}P$ (SCHNOHR, 2012). Figure 7.3 compares the ΔE_{struc} for some III-V ternary alloys with zinc blende structure, revealing that this term is almost zero for $In_xAl_{1-x}Sb$, which means the electronic effect practically afford for the experimental band gap measured. Moreover, for the same mixed sublattice (In and Ga), the ΔE_{elec} contribution, for x=0.5, corresponding to 41%, 30% and 33% of the ΔE, for $Ga_{(1-x)}In_{(x)}P$, $Ga_{(1-x)}In_{(x)}As$ and $Ga_{(1-x)}In_{(x)}Sb$, respectively, showing the importance of distinct anion sublattice. Thus, it was observed that $In_xGa_{1-x}P$ is the one with the highest ΔE_{struc} contribution, which is associated with the respective highest lattice mismatch (0.436 Å). Tit *et al*. (TIT; OBAIDAT; ALAWADHI, 2009a), using sp^3 tight-binding method, established for $CdSe_{(x)}Te_{(1-x)}$ and $ZnSe_{(1-x)}Te$, common-cation ternary alloys, that the competition in trapping charges between the anions (Se and Te) should be the main reason for the experimentally observed band gap bowing. The same authors, however, found out that the lack of such competition mentioned should be the explanation of the almost absence of band gap bowing in common-anion II-VI ternary alloys (TIT; OBAIDAT; ALAWADHI, 2009b). Therefore, whereas both structural and electronic effects are relevant to the band gap bowing in III-V ternary alloys, only the former seems to be significant in II-VI ternary alloys.

Figure 7.2 – Bowing of the bandgap versus composition x for $In_xGa_{1-x}Sb$. The shaded area corresponds the range of experimental values reported in the literature together with the average values

(ΔE^{av}) exposed in Ref (ADACHI, 2009). The bowing structural contribution is plotted as blue squares whist the electronic contribution is represented by the black arrow.

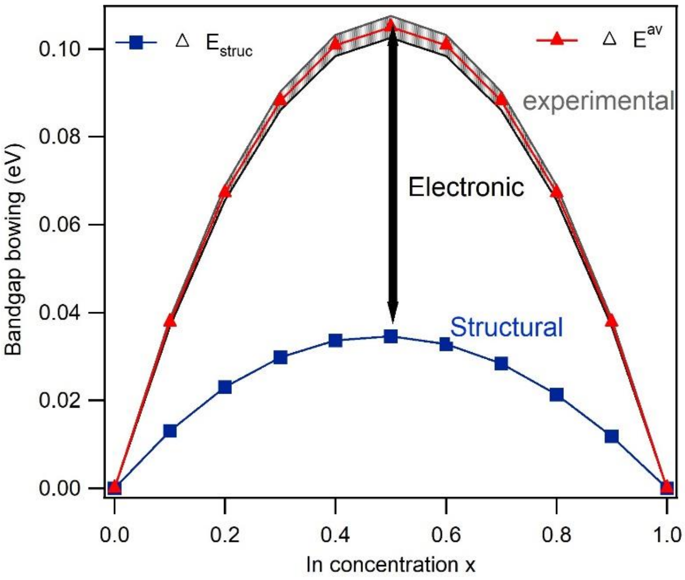

Figure 7.3 Structural bandgap bowing contribution versus composition x for $In_xGa_{1-x}P$,$In_xGa_{1-x}As$, $In_xGa_{1-x}Sb$ and $In_xAl_{1-x}Sb$ ternary alloys. All experimental values necessary to calculate ΔE_{struc} were obtained from the Refs (ADACHI, 2009)(SCHNOHR, 2012)(MIKKELSEN; BOYCE, 1983)(BOLZAN et al., 2021d).

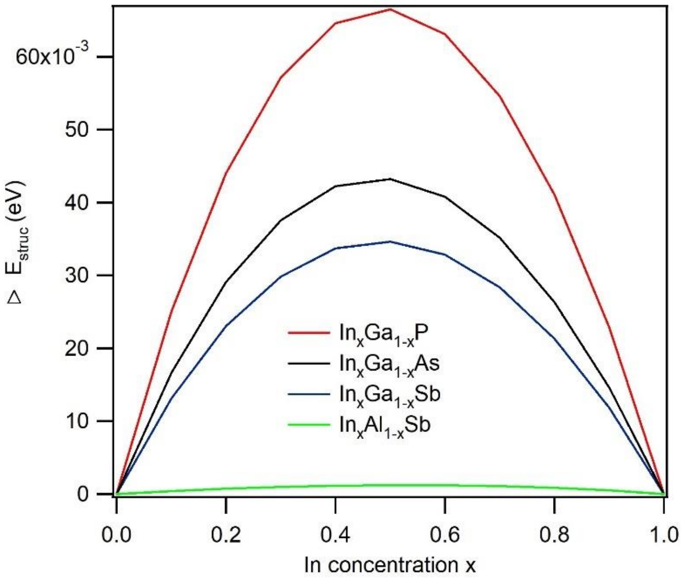

7.1 RELEVANCE OF THE MODEL BY BALZAROTTI *ET AL*

The atomic displacement in $A_{(1-x)}B_{(x)}C$ ternary alloys are significatively different for the common and mixed sublattices as reported experimentally and through simulation (SCHNOHR, 2015). The values of average interatomic distances (A-C-A and B-C-B) associated with the mixed sublattice are closer to the ones predict by the VCA than the respective values of the binary compounds. In the common sublattice, a reverse situation is verified with the interatomic distances (C-A-C and C-B-C) closer to the values of their binary compounds even in strained ternary alloys (BOLZAN et al., 2021d). Therefore, the mixed sublattice is more flexible than the rigid common sublattice. As reported by Jeong *et al.* (JEONG et al., 2001), not just the magnitude of the atomic displacement is distinct in the two sublattices, but also the direction in which they occur. For $In_{(x)}Ga_{(1-x)}As$, it was observed, using Kirkwood potential, that the probability distribution of the cations are nearly isotropic and sharp peaked around vertices of the tetrahedron, whereas for the anion an evident anisotropy along the <100> and <111> directions was obtained and is strictly correlated with the model by Balzarotti *et al*. This findings partly confirm the success of the model by Balzarotti *et al,* which does not take into account neither the bond bending distortion energy nor the relaxation of the mixed sublattice. Furthermore, Zunger and Martins (MARTINS; ZUNGER, 1984) reported that the inclusion of bond bending and cation relaxation effects in the calculation of the first NN distances behave in opposite direction mostly canceling each other. Balzarotty *et al.* included both effect in $Cd_{(1-x)}Mn_{(x)}Te$ and $In_{(1-x)}Ga_{(x)}Sb$, reveling only a slight modification (0.1%) in the average NN bond length compared with the model without both effects. Hence, models that neglect both effects are better than the ones that incorporate solely one of them, supporting the usefulness of the model by Balzarotti *et al.*

8 APPENDIX B- UNIRRADIATED IN$_X$GA$_{1-X}$SB FILM DIMENSIONS

Table B - Dimensions of the unirradiated In$_x$Ga$_{1-x}$Sb samples used in this work (t - thickness, L - width and H - length). The uncertainty in thickness t is 10%.

Samples	t(nm)	L(mm)	H(mm)
InSb	320	7.30	19.85
$In_{0.8}Ga_{0.2}Sb$	440	9.90	10.60
$In_{0.6}Ga_{0.4}Sb$	320	8.26	10.24
$In_{0.5}Ga_{0.5}Sb$	310	10.22	19.02

9 APPENDIX C - EXAFS OSCILLATIONS OF $In_xGa_{1-x}Sb$ FILMS IRRADIATED WITH 8 MEV AU^{+3} IONS

For room-temperature measurements, k^3-weighted EXAFS spectra at the In and Ga K-edges are shown in Figure 9.1-a and Figure 9.1-b as a function of the photoelectron wavenumber for the fluence of 5x10^{14} cm^{-2}. Fourier-transformed spectra and the respective fits are presented in Figure 9.1-c and Figure 9.1-d. Additional peaks become apparent in the In and Ga spectra below R$\sim$ 2 Å for the highest fluence used in this work, which are related to oxide formation. These oxides were not taken into account in the EXAFS analysis due to their small contributions. Table C summarizes the structural parameter for the first shell measured at In and Ga K edges after ion irradiation for the highest fluence used here. Table D shows the R-factor obtained for all samples for different ion fluences.

Figure 9.1 - (a), (b) k^3-weighted EXAFS spectra of $In_xGa_{1-x}Sb$ for In (left) and Ga (right) K-edges as a function of the photoelectron wavenumber for fluence of 5x10^{14}cm^{-2}. The corresponding Fourier-transformed spectra of $In_xGa_{1-x}Sb$ for four different In/Ga ratio concentrations at: (c)In K-edge and (d) Ga K-edge

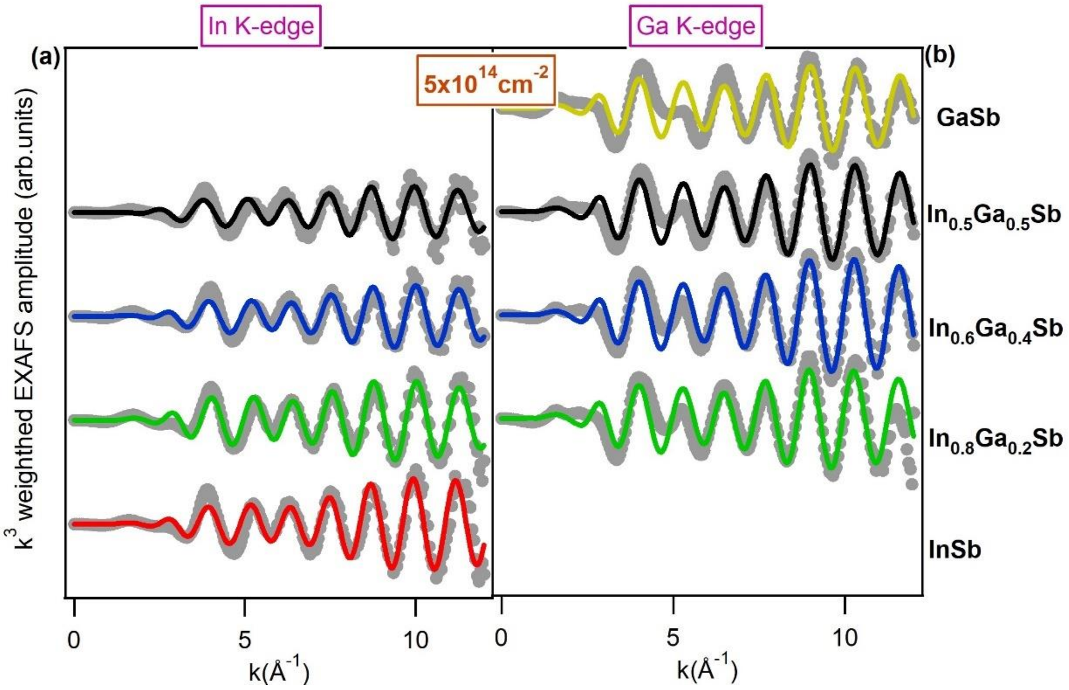

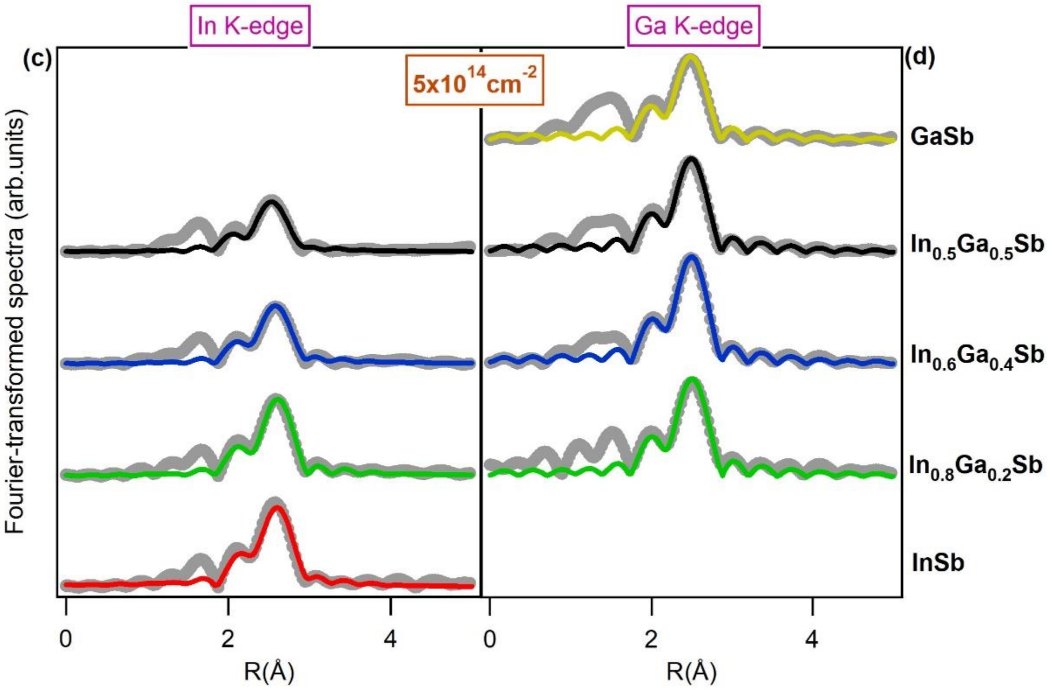

Table C - Interatomic distances obtained from EXAFS measured at the In and Ga K-edges of $In_xGa_{1-x}Sb$ films upon ion irradiation for an irradiation fluence of 5 × 10^{14} cm^{-2}.

	Interatomic distance(Å)		Debye-Waller factor (10^{-3} A^2)	
	In K-edge	Ga K-edge	In K-edge	Ga K-edge
	1stNN Sb	1stNN Sb	1stNN Sb	1stNN Sb
InSb	2.813±0.009		5±1	
$In_{0.8}Ga_{0.2}Sb$	2.809±0.007	2.66±0.01	3±1	7±1
$In_{0.6}Ga_{0.4}Sb$	2.806±0.008	2.656±0.008	7±2	6±2
$In_{0.5}Ga_{0.5}Sb$	2.801±0.008	2.651±0.006	7.4±0.7	6±1
GaSb		2.649±0.007		4±2

Table D – R-factor obtained for all samples for different ion fluences.

	R-factor (In K-edge | Ga K-edge)					
	NI	1x10^{13}	5x10^{13}	1x10^{14}	3x10^{14}	5x10^{14}
InSb	0.004 |	0.02 |	0.005|	0.004 |	0.08 |	0.1 |
$In_{0.8}Ga_{0.2}Sb$	0.002 | 0.02	0.01 | 0.009	0.04 | 0.02	0.008 | 0.008	0.05 | 0.02	0.03 | 0.04
$In_{0.6}Ga_{0.4}Sb$	0.004 | 0.02	0.02 | 0.02	0.08 | 0.03	0.009 | 0.03	0.06 | 0.04	0.03 | 0.02
$In_{0.5}Ga_{0.5}Sb$	0.004 | 0.01	0.02 | 0.01	0.01 | 0.01	0.1 | 0.03	0.1 | 0.04	0.1 | 0.03
GaSb	| 0.007	| 0.02	| 0.02	| 0.06	| 0.04	| 0.04

10 APPENDIX D- PUBLICATIONS

Candidate's journal publications that have originated during the PhD. Articles directly related to this thesis are highlighted.

Giulian, R., Bolzan, C. A., Salazar, J. B., & da Cunha, C. R. (2019). *Ion irradiation-induced foams in antimonide binary alloys: A combination of small energy bandgap with giant surface-to-bulk ratio. Energy Reports.* doi:10.1016/j.egyr.2019.09.059

Manzo, D. J., Bolzan, C. A., de Andrade, A. M. H., Schoffen, J. R., & Giulian, R. (2019). *Structural and compositional analysis of GaSb nanofoams obtained by ion irradiation of sputtered films. Thin Solid Films, 687, 137447.* doi:10.1016/j.tsf.2019.137447

Bolzan, C. A., Manzo, D. J., de Andrade, A. M. H., Schoffen, J. R., & Giulian, R. (2019). *Characterization of polycrystalline In(y)Al(x)Sb(1-x-y) films deposited by magnetron sputtering. Thin Solid Films, 137630.* doi:10.1016/j.tsf.2019.137630

Giulian, R., Bolzan, C. A., Rossetto, L. T., de Andrade, A. M. H., Schoffen, J. R., Araujo, L. L., & Boudinov, H. I. (2020). *Atomic composition, structure, and electrical properties of In1-xGaxSb films deposited by magnetron sputtering. Thin Solid Films, 138213.* doi:10.1016/j.tsf.2020.138213

Bolzan, C. A., Manzo, D. J., Notthoff, C., Kluth, P., & Giulian, R. (2021). *Stoichiometry-dependent porosity by ion irradiation: In(1–x)Al(x)Sb films. Journal of Physics and Chemistry of Solids, 148, 109769.* doi:10.1016/j.jpcs.2020.109769

Bolzan, C. A, Johannessen, B., Wu, Z., Giulian, R. (2021). *Local and extended atomic structure of strained polycrystalline* $In_{(1-x)}Al_{(x)}Sb$ *alloys*. *Journal of Physics and Chemistry of Solids, 109844. doi: 10.1016/j.jpcs.2020.109844*

Bolzan, C. A, Johannessen, B., Wu, Z., Giulian, R. (2021). ***Local structure of porous InSb films: From first to third-shell EXAFS investigation*. *Solid state science, 106705. doi: 10.1016/j.solidstatesciences.2021.106705***

Giulian, R., Bolzan, C. A., Rossetto, L. T., de Andrade, A. M. H.,Dias J.F. $In_{1-x}Ga_xSb$ ***nanofoams made by ion irradiation of sputtered films: Atomic composition and structure*****,139263.doi: 10.1016/j.tsf.2022.139263**

Bolzan, C. A. , Johannessen, B., Wu,Z., Giulian, R.. Atomic-scale structure of $In_xGa_{1-x}Sb$ **thin films as-deposited and after ion irradiation, in preparation.**

Bolzan, C. A., Giulian, R., Rossetto, L.T.,Kochenborger, A.S. Thermal stability of $In_{1-x}Ga_xSb$ **nanofoams, in preparation.**

Bolzan, C. A., Rossetto, L.T., Giulian, R.. Ion irradiation effects on the thermoelectric properties of $In_xGa_{1-x}Sb$ **thin films, in preparation.**